Nanoplasmonic Surface Structures for Integrated Photonics

Paul Michael Zeph Davies

Imperial College London, Department of Physics

PhD

Statement of Originality

I, Paul Michael Zeph Davies, declare that I am the sole author of this thesis, which is the record of work carried out by me at the University of Surrey, Guildford, and at Imperial College London. The reported results constitute original work to the best of my knowledge, except where otherwise acknowledged or referenced within the thesis itself. Neither the thesis nor any of its original contents have previously been submitted for a higher degree in any university.

Abstract

Nanoplasmonic surfaces are known to be able to alter the localisation and propagation characteristics of light owing to the subwavelength interactions with the metallic elements. The recent improvements of nanolithography and self-assembly techniques have enabled the design of ever smaller and intricate structures with a high precision, allowing for research into more complex nanoplasmonic structures that control light on the nano-scale. Up until now, plasmonic surfaces are mostly operated with out-of-plane excitation which, although well-established and experimentally convenient to perform, has limited potential for on-chip applications.

The integration of surface plasmonic structures with photonic waveguides allows for light to be confined to a guiding layer while being kept in interaction along the surface structure without inducing uncontrolled scattering or excessive dissipative loss. In this work, plasmonic surface structures such as plasmonic antennas and array structures that are integrated with a CMOS compatible platform are explored. In particular, a new class of plasmonic surfaces, plasmonic nanogap tilings, are introduced. Remarkably, these simple periodic structures provide a rich physics characterised by many different regimes of operation, including subwavelength surface enhancement, hybrid plasmonic-photonic resonances, transmission stop-bands, resonant back scattering, coupling to out-of-plane radiation and asymmetric transmission. The ability of the nanogap tiling to concentrate the field on the surface is studied in detail as it allows for sensing changes in the dielectric medium on the accessible surface or the inclusion of nonlinear or gain materials to functionalise the device in an integrated setup.

Contents

List of Figures

Acknowledgements

I would like to express my gratitude to Professor Ortwin Hess for providing me with the opportunity to work within his research group and to study for my PhD. His supervision and guidance throughout the project has been invaluable.

I am particularly grateful to Dr. Sebastian Wuestner and Dr. Andreas Pusch for their assistance throughout the project and for their assistance with regards Thesis feedback.

I would also like to offer my sincere thanks to Professor Stefan Maier and Dr. Yannick Sonnerfraud for their collaboration with writing our published paper in ACS Nano [1].

At this point I'd like to mention my office co-workers, Freddie Page, Tim Pickering, John Wood and Fabian Renn, for the friendly office banter and readily available advice and discussions on a multitude of different topics when requested.

Finally, I would like to take this opportunity to express my huge thanks and unyielding gratitude to Dr. Joachim Hamm, my daily supervisor, who aided me on my PhD from start to finish. Dr. Hamm provided clear guidance, teaching, insight, knowledge and advice: a simple "thank you" will never be enough.

In addition to my work friends, I would like to express my thanks to my whole family, especially my parents Helen and Martin, for their continuous love, support and encouragement throughout my academic career, and beyond.

Also my close friends - you know who you are - who have supported me through life and especially during this trying time.

And lastly, to Lizzie, who entered my life in the final stages of writing up and provided me with the love and drive I needed to see this through to the end.

Chapter 1

Introduction

Technology is ever pushing towards smaller and faster devices for use within a wide range of scientific applications. Electronic systems alone are fast approaching their fundamental limits of speed and bandwidth and considerable effort is being expended to circumvent these limits. One leading solution is to replace the use of electrons as the information carrier with electromagnetic waves, via the use of photonic platforms, as the waves travel at the speed of light. However, the geometry of photonic devices is limited by the diffraction limit of light [2]: a constraint in the confinement of light of the order of around half the wavelength of the light. Visible light's wavelength, for example, is many times larger than the smallest geometric size of current electronic components, rendering the use of optics inadequate for miniaturisation. Shorter light wavelengths may be used, such as ultra-violet, but these can be damaging to some materials in chemical or biological applications.

Despite some plasmonic effects being seen in the early 1900s [3, 4], it took until recent years [5] before their origins were sufficiently understood to allow further research into plasmonics. This research has lead to new methods of controlling light in the subwavelength [6]; well beyond the diffraction limit. It was observed that light can be confined to interfaces where the permittivity changes sign, such as that of a metal-dielectric interface when the frequency of the light is below the plasma frequency of the metal. Collective oscillations of the free electrons at the surface of a metal, known as surface plasmons, form under the influence of an incident electric field [7]. Under certain conditions, these surface plasmons are able to couple with light to produce a propagating wave along the interface [8], known as surface plasmon polaritons. Metallic particles, due to their small size, limit the propagation of the surface plasmon polaritons resulting in standing wave resonances within the particle. These are known as localised surface plasmon resonances [9, 10], and are sensitive to the size and shape of the particle as well as the dielectric environment in which it resides [11]. This enables metallic particles to be used for a variety of different applications, such as scattering antennas [12] and biosensors [13, 14]. The resonances of individual particles are able to interact with neighbouring particles, providing a means to transfer energy along the structure [15].

With the recent advancement in nanolithography and other technologies [16], the fabrication of nano-scale metallic structures that resonate with visible and infra-red light has been possible, renewing interest into plasmonics and subsequently nanoplasmonics. This allows for the creation of structures whose only limitation in size is due to the atomic nature of matter itself. Plasmonic guides are able to channel light [17, 18] and focus it into a single hot-spot [19]. This paves the way for nano-tip detection and excitation devices that are now widely used [20, 21].

Plasmonic nanostructures, whose structure is smaller than the wavelength of light, alter the bulk properties of a material in a similar way to photonic crystals [22]. This behaviour provides the foundation for the vast world of metamaterials; designer materials whose properties are defined by their structure rather than the material the device consist of. With the properties of the medium being controllable by the structure of the device, along with the improving technology in nano-scale fabrication, it is possible to create metamaterials with properties that are not found in nature. Such properties include materials capable of altering the propagation of light [23] and which simultaneously have both a negative permittivity and permeability for a given frequency band [24, 25], leading to effects such as perfect lensing [26], cloaking [27, 28] and slow or stopped light [29] useful for (e.g.) data storage. The abilities of plasmonic structures and metamaterials to provide such expansive and exciting concepts are rapidly pushing forward research into the field of nanoplasmonics.

Two dimensional metamaterials (or metasurfaces [30]) which consist of subwavelength arrays of plasmonic nanoparticles are frequently studied. Plasmonic surface structures, such as these metasurfaces, are usually illuminated by out-of-plane radiation [31], with the transmission and/or reflection being recorded, as this method is both numerically and experimentally convenient to perform. Many plasmonic surface structures have undergone extensive research due to the wide array of properties and effects they have shown, such as extraordinary transmission through holes arrays [32, 33], varying colour resonances [34, 35] and surface field enhancements that are important for sensing applications, such as surface enhanced Raman scattering [36] and fluorescence [37]. The enhancement of the electromagnetic field strength in the nanogaps between plasmonic particles is known to improve the sensing abilities of devices [38, 39], which can additionally be improved when arranged in an array [40, 41].

Unfortunately, the use of plasmonics has a major drawback: the Ohmic losses induced within the metallic components render the structures inherently lossy when compared to non-metallic optical devices. Therefore, a lot of research is being directed into methods of overcoming the losses associated with plasmonics, such as creating active and gain-enhanced structures [42, 43], or integrating plasmonics with photonics [44, 45] to increase the propagation lengths.

The work of this thesis investigates the latter of these techniques by integrating a patterned metallic surface with a photonic waveguide. The light wave in the device hybridises between the two systems combining the long-range propagation of the photonic waveguide with the functionality of the plasmonic structure. Such hybrid plasmonic-photonic structures are known to significantly increase propagation lengths [44]. Gain can still be incorporated into hybrid systems [46, 47], potentially allowing for both methods to assist in controlling the loss. Since the surface structure is illuminated by the underlying waveguide mode, the surface structure is kept in interaction along the entirety of its length. In addition, the waveguide mode has a phase retardation that can be synchronised with the structure spacing, producing Floquet-Bloch waves which resonate with the periodic medium.

Integration of plasmonics with photonic platforms lends itself to surface structures which can be illuminated by the evanescent tail of the waveguide mode. This indirect coupling can result in strong plasmonic effects without inducing the high losses otherwise associated with plasmonic modes. The polarisation of the electromagnetic fields relative to the surface structure will change the interaction of the fields with the plasmonic elements, such as altering the profile of the guided mode or charge separation across the elements.

The following chapter begins by introducing the classical electromagnetic theory via the use of Maxwell's equations. It continues by describing dielectric and plasmonic materials before ending with a overview of the simulation method used in this work.

Chapter 3 introduces the hybrid platform used for the research of this thesis. It explores the photonic system and its associated modes, and introduces a simplistic one-dimensional plasmonic surface grating for coupling between the photonic waveguide and external radiation.

Chapter 4 introduces a particular class of plasmonic surface structures, nanogap tilings, and discusses in detail the optical properties of one type of nanogap tiling, triangular nanogap tile structure. To begin, an isolated trimer molecule is explored on the photonic platform to examine the scattering and field enhancement produced by the nanogap. This exploration is then extended to cover a dense triangular array of these trimer molecules (the triangular nanogap tiling), looking in detail at the different regimes of operation available. These include out-of-plane scattering, resonant backscattering and hybridisation of the plasmonic mode. The scattering spectra of the device is then compared to the same device but with reversed illumination revealing asymmetric transmission and mode conversion. Finally the surface enhancement ability of the tiling is explored and applied to the theoretical use of a gain medium to counter the losses of the system.

Chapter 5 concludes this work and offers some examples of further potential research using the proposed hybrid platform.

Chapter 2

Electromagnetic Theory

This chapter provides an overview of the interaction of light with matter as described by Maxwell's equations (section 2.1). When these equations are used in conjunction with the constitutive relations, the dipole response of matter to electromagnetic fields can be described and single-field variants can be formed to describe the interaction of light with matter. These equations can be applied to planar dielectric systems (section 2.2) and plasmonic systems with the addition of the Drude model description (section 2.3), yielding modal information regarding the polarisation of the electromagnetic fields in relation to the geometry of the system. These mode conditions, along with appropriate boundary conditions, simplify the system of partial differential equations which are solved computationally (section 2.4) for the geometries studied in this thesis.

2.1 Maxwell's Equations

Maxwell's equations describe the evolution of electromagnetic fields and are named after the physicist James Clerk Maxwell who formulated the equations over 150 years ago [48]. The set of equations are able to accurately describe a wide range of classical electromagnetic phenomena, from scales of that of the cosmos down to the nano scale [6].

Maxwell's equations are used in the context of the present work to describe the local interaction of light with nano scale metallic particles and dielectric materials. They accurately describe the evolution of electromagnetic fields within a given system.

The electric field intensity $\mathbf{E}(\mathbf{r}, t)$ and magnetic induction $\mathbf{B}(\mathbf{r}, t)$ can be described by the set of equations [49]

$$\nabla \cdot \mathbf{D}(\mathbf{r}, t) = \rho_f(\mathbf{r}, t) \tag{2.1a}$$

$$\nabla \cdot \mathbf{B}(\mathbf{r}, t) = 0 \tag{2.1b}$$

$$\frac{\partial}{\partial t}\mathbf{D}(\mathbf{r}, t) + \mathbf{J}_f(\mathbf{r}, t) = \nabla \times \mathbf{H}(\mathbf{r}, t) \tag{2.1c}$$

$$\frac{\partial}{\partial t}\mathbf{B}(\mathbf{r}, t) = -\nabla \times \mathbf{E}(\mathbf{r}, t). \tag{2.1d}$$

The set of equations 2.1 are Maxwell's equations in their macroscopic form. They describe how the electromagnetic fields evolve through space and over time. The macroscopic fields, electric displacement $\mathbf{D}(\mathbf{r}, t)$ and magnetic field strength $\mathbf{H}(\mathbf{r}, t)$, are connected to the microscopic charge density $\rho_\mathrm{m}(\mathbf{r}, t)$ and current density $\mathbf{J}_\mathrm{m}(\mathbf{r}, t)$. These describe bound charges and currents on the scale of atoms or molecules of the system, spatially averaged to obtain the macroscopic descriptions.

In the absence of free charges ($\rho_f(\mathbf{r}, t) = 0$) and currents ($\mathbf{J}_f(\mathbf{r}, t) = 0$), the set of equations can be simplified. To relate the macroscopic fields with the spatially averaged microscopic fields, constitutive relations are necessary. The constitutive relations can be expressed as

$$\mathbf{D}(\mathbf{r}, t) = \varepsilon_0 \mathbf{E}(\mathbf{r}, t) + \mathbf{P}(\mathbf{r}, t) \tag{2.2a}$$

$$\mathbf{B}(\mathbf{r}, t) = \mu_0(\mathbf{H}(\mathbf{r}, t) + \mathbf{M}(\mathbf{r}, t)), \tag{2.2b}$$

where $\mathbf{P}(\mathbf{r}, t) = \mathbf{P}[\mathbf{E}](\mathbf{r}, t)$ and $\mathbf{M}(\mathbf{r}, t) = \mathbf{M}[\mathbf{H}](\mathbf{r}, t)$ are the electric polarisation and magnetisation of a material respectively. This describes the dipole response of a material to the electromagnetic fields. The square brackets denote a functional dependence on the history of the electromagnetic fields.

In the case of an electromagnetic field whose evolution can be expressed as a frequency-dependent solution (i.e. time-harmonic) in a dispersive and linear material, the local polarisation and magnetisation can be written in the form

$$\mathbf{P}(\mathbf{r},\omega) = \varepsilon_0 \chi_{\mathrm{e}}(\mathbf{r},\omega)\mathbf{E}(\mathbf{r},\omega) \tag{2.3a}$$

$$\mathbf{M}(\mathbf{r},\omega) = \chi_{\nu}(\mathbf{r},\omega)\mathbf{H}(\mathbf{r},\omega), \tag{2.3b}$$

where ε_0 and μ_0 are the free-space permittivity and permeability, respectively. The $\chi_{\mathrm{e}}(\mathbf{r},\omega)$ and $\chi_{\nu}(\mathbf{r},\omega)$ terms are the electric and magnetic susceptibilities of the medium which describe the strength of the response of the material to the electromagnetic fields. The susceptibilities are related to the relative permittivity $\varepsilon_{\mathrm{r}}(\mathbf{r},\omega) = 1 + \chi_{\mathrm{e}}(\mathbf{r},\omega)$ and permeability $\mu_{\mathrm{r}}(\mathbf{r},\omega) = 1 + \chi_{\nu}(\mathbf{r},\omega)$ of the material.

The constitutive relations can now be combined with Maxwell's equations to give two time-harmonic differential equations for the electric and magnetic fields depending on the permittivity and permeability of the material

$$-i\omega\varepsilon_0\varepsilon_{\mathrm{r}}(\mathbf{r},\omega)\mathbf{E}(\mathbf{r},\omega) = \nabla \times \mathbf{H}(\mathbf{r},\omega) \tag{2.4a}$$

$$-i\omega\mu_0\mu_{\mathrm{r}}(\mathbf{r},\omega)\mathbf{H}(\mathbf{r},\omega) = -\nabla \times \mathbf{E}(\mathbf{r},\omega). \tag{2.4b}$$

It is clear from the above equations that the electric field can be determined from the magnetic field and vice versa. This allows for the above equations to be combined and rewritten in terms of one of the electromagnetic fields, rendering the equations independent. This is favourable when solving computationally as only one of the two fields needs to be calculated for a given system, yielding the solutions for both fields. This substitution provides a Helmholtz equation, linking the time and space components for the fields.

The electric Helmholtz equation is as follows

$$\frac{\omega^2}{c^2}\mathbf{E}(\mathbf{r},\omega) = \varepsilon_\mathrm{r}^{-1}(\mathbf{r},\omega)\nabla \times \left[\mu_\mathrm{r}^{-1}(\mathbf{r},\omega)\nabla \times \mathbf{E}(\mathbf{r},\omega)\right], \tag{2.5a}$$

with the magnetic case

$$\frac{\omega^2}{c^2}\mathbf{H}(\mathbf{r},\omega) = \mu_\mathrm{r}^{-1}(\mathbf{r},\omega)\nabla \times \left[\varepsilon_\mathrm{r}^{-1}(\mathbf{r},\omega)\nabla \times \mathbf{H}(\mathbf{r},\omega)\right]. \tag{2.5b}$$

Alternatively, the two equations can be obtained from each other with the substitutions $\mathbf{E} \to \mathbf{H}$, $\mathbf{H} \to -\mathbf{E}$ and $\mu \leftrightarrow \varepsilon$.

The direction and amplitude of the power flow of electromagnetic energy is given by the Poynting vector, and it is calculated as the cross product of the two electromagnetic fields

$$\mathbf{S} = \mathbf{E} \times \mathbf{H}. \tag{2.6}$$

In frequency domain, it is generally useful to know the average power flow per unit of time, which can be calculated from treating the electromagnetic components as complex vectors

$$\langle \mathbf{S} \rangle = \frac{1}{2}\mathrm{Re}\left\{\mathbf{E} \times \mathbf{H}^*\right\}. \tag{2.7}$$

In the next section, equations 2.5 will be solved for basic planar dielectric systems before discussing the inclusion of plasmonic materials in preparation for the hybrid plasmonic-photonic platform introduced later in the thesis.

2.2 Planar Dielectric Structures

The Helmholtz equations (2.5) can be applied to planar dielectric systems to provide the propagation characteristics and polarisations of the electromagnetic fields within these systems.

Consider a homogeneous and isotropic dielectric medium with a propagating plane wave in the positive z-direction. Such a system supports transverse electromagnetic (TEM) modes, where there are no field components in the propagation direction ($\mathrm{H_z} = \mathrm{E_z} = 0$). Now consider a planar dielectric system with varying material properties in the y-direction (also known as a stack or slab material system). With the geometric variation in the y-direction the field orientation relative to the stack becomes important, resulting in two fundamental orientations: when one or the other of the two electromagnetic fields is tangential to the planar stack. These are known as the transverse electric (TE) and transverse magnetic (TM) modes and are depicted in figure 2.1.

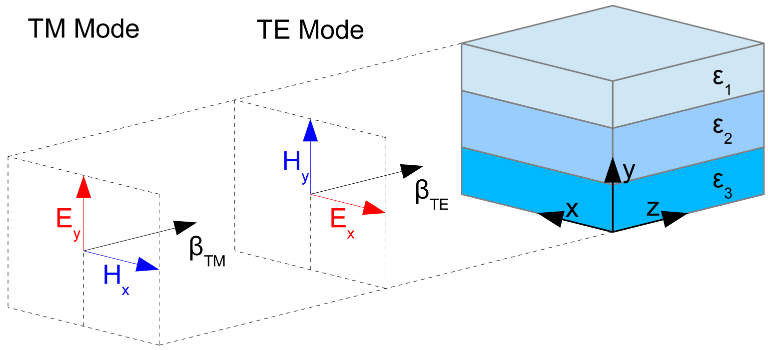

Figure 2.1: TE and TM electromagnetic field polarisations for a planar dielectric stack.

The TE solution has no electric component in the propagation direction ($\mathrm{E_z} = 0$) and is polarised to oscillate in-plane to the structure (i.e. $\mathrm{E}_y = 0$). Therefore, the TE solution only has a single electric field component and can be written as

$$\mathbf{E}(\mathbf{r}, \omega) = \begin{pmatrix} \mathrm{E_x} \\ 0 \\ 0 \end{pmatrix}, \ \mathbf{H}(\mathbf{r}, \omega) = \begin{pmatrix} 0 \\ \mathrm{H}_y \\ \mathrm{H_z} \end{pmatrix}. \tag{2.8}$$

From this condition, an ansatz can be made for a solution to the electric field since the amplitude and polarisation of the field remains continuous along the z-direction and additionally, due to the continuous planar geometry, the fields also do not depend on x. Therefore, the following solution can be proposed

$$\mathbf{E}(y, z, \omega) = \mathbf{E}(y) e^{-i\omega t + i\beta z}, \tag{2.9}$$

where the propagation constant of the mode is given by $\beta = n_{\text{eff}} k_0$, where n_{eff} is the effective refractive index of the mode ($n = \sqrt{\varepsilon}$).

Inserting this solution into the Helmholtz equation from section 2.5, the following eigenvalue equation is found

$$\left(n^2 \frac{\omega^2}{c^2} - \beta^2 \right) \mathrm{E}_x = \mu_{\mathrm{r}} \frac{\partial}{\partial y} \mu_{\mathrm{r}}^{-1} \frac{\partial}{\partial y} \mathrm{E}_x. \tag{2.10a}$$

For a given frequency ω, β is the corresponding eigenvalue of the solved mode. For a purely dielectric (and therefore non-magnetic) stack, the relative permeability $\mu_{\mathrm{r}} = 1$, simplifying the equation further. The differential Helmholtz equation is solved for given geometry parameters (i.e. the spacial dependence of the permittivity and permeability), providing the solutions to the TE polarised electromagnetic fields.

Using the same substitutions as before ($\mathbf{E} \to \mathbf{H}$, $\mathbf{H} \to -\mathbf{E}$ and $\mu \leftrightarrow \varepsilon$), the TM solution is equivalently obtained, directly from the TE Helmholtz equation

$$\left(n^2 \frac{\omega^2}{c^2} - \beta^2 \right) \mathrm{H}_x = \varepsilon_{\mathrm{r}} \frac{\partial}{\partial y} \varepsilon_{\mathrm{r}}^{-1} \frac{\partial}{\partial y} \mathrm{H}_x. \tag{2.10b}$$

At the interface between two dielectrics, any light wave which passes between the two media will undergo refraction due to the difference in permittivities. In order for the wavevector along the interface between the two dielectric media to remain constant the speed of the propagating wave must change from one medium to the other, resulting in a change of the angle of propagation (see figure 2.2). The angle from the normal of the interface is greater in a lower permittivity material after refracting from a higher permittivity material. At a certain large enough incident angle, known as the critical angle, the refracted wave propagates along the interface. If the incident angle was to increase further, the light would no longer be transmitted but instead totally internally reflects back into the source medium. Note that this cannot happen when going from a lower permittivity dielectric to a higher permittivity as the wave refracts towards the normal to the interface. A by-product of total internal reflection is the appearance of an evanescent wave at the interface. Essentially, the field penetrates into the second medium, without any transfer of energy. The evanescent wave propagates along the interface, and exponentially attenuates into the second medium. The wavevector of the evanescent propagation is equivalent to the projection of the incoming wavevector to the plane of the surface.

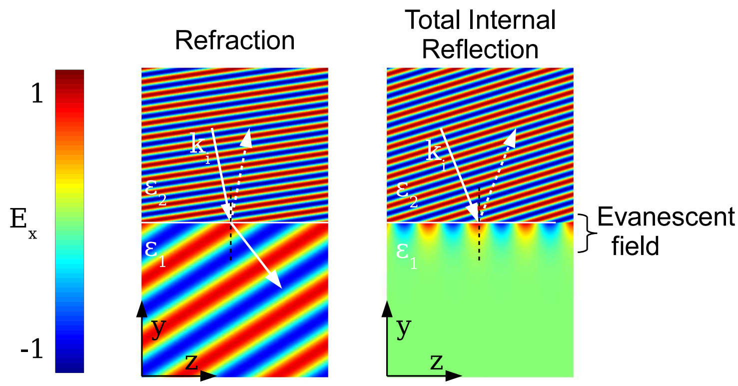

Figure 2.2: Refraction (left) and total internal reflection (right) at the interface between two dielectrics, where $\varepsilon_2 > \varepsilon_1$. The electric field of the reflected wave (dashed arrow) is not shown for clarity.

If an additional low-permittivity layer is added around the higher permittivity layer such that a three-layer slab (or planar) waveguide structure is constructed, then the light can be confined to the higher permittivity waveguide via total internal reflection from both interfaces. This effectively traps the light within the higher permittivity layer resulting in an effectively bound mode. Due to the discrete size of the waveguide, the transverse resonance condition states that only discrete waveguide modes may form due to the interference of the wavefronts after reflecting off both interfaces. These discrete waveguide modes form harmonics of the system; the fundamental mode being depicted in figure

2.3.

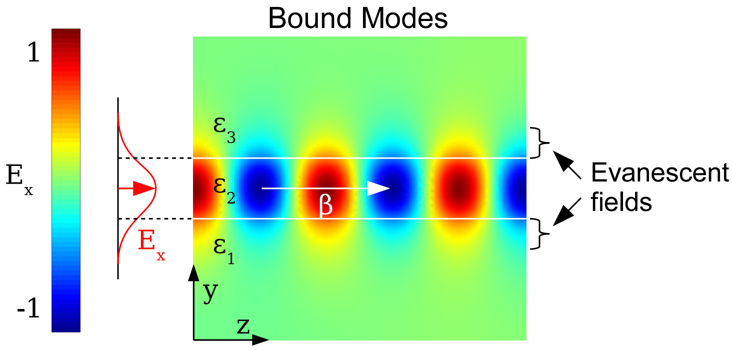

Figure 2.3: A bound mode within a dielectric slab waveguide, where $\varepsilon_2 > \varepsilon_1$, ε_3.

The bound mode produced by the waveguide stack forms the basis for the integrated dielectric platform used in this work. The evanescent field of the bound mode is exploited by a plasmonic material, introduced in next section.

2.3 Plasmonic Materials

Plasmonic materials are materials which have a plasma or plasma-like property that can be influenced by external electromagnetic fields, notably metals with their free electron density. In the case of metals, an applied electric field will cause a shift in the electron density of the metal, inducing an electric field which counteracts the incident electric field within the material. An oscillating incident field will cause the electrons to oscillate within the metal forming a plasmon. These shifted electrons have a restoring force on them from the lattice of positive ions of the metal, allowing the electrons to shift back to equilibrium if the external field is removed. This return to equilibrium happens at the plasma frequency ω_p of the metal, given by the free electron model as

$$\omega_\mathrm{p} = \sqrt{\frac{Ne^2}{m^* \varepsilon_0}}, \tag{2.11}$$

where N is the electron number density (concentration) and e is the unit charge. If the frequency of the external electric field is much lower than the plasma frequency of the metal ($\omega \ll \omega_{\mathrm{p}}$), the electron density is able to shift completely within one oscillation, resulting in the complete compensation of the electric field, nullifying it and causing the wave to be fully reflected. If the frequency of the external light becomes greater than the plasma frequency ($\omega > \omega_{\mathrm{p}}$), the electron motion cannot fully counteract the field allowing the field to penetrate into the metal.

The permittivity of a metal ε_{m} can be estimated with the Drude model, named due to the similarities with the model for electrical conduction in metals proposed by Paul Drude. The complex permittivity of a Drude metal is written [50]

$$\varepsilon_{\mathrm{m}}(\omega) = \varepsilon_{\mathrm{b}} - \frac{\omega_{\mathrm{p}}^2}{\omega^2 + i\omega\gamma}, \tag{2.12}$$

where ε_{b} (sometimes written ε_{∞}) is the metal's bulk (background) dielectric permittivity (often given the value of 1), ω_{p} is the plasma frequency of the metal, from equation 2.11, and γ is the attenuation constant (i.e. the losses) of the metal. The attenuation arises due to Ohmic loss from the resistance of the electron motion from the material, due to, for example, collisions and scattering of the electrons by the lattice of ions in the metal. At frequencies higher than the plasma frequency ($\omega > \omega_{\mathrm{p}}$), the ω^2 term becomes dominant, and the losses of the system become negligible (as $\gamma \ll \omega_{\mathrm{p}}$). From equation 2.12 it is clear that for frequencies below the plasma frequency ($\omega < \omega_{\mathrm{p}}$) the permittivity of the metal becomes negative. For noble metals, such as gold and silver, this occurs at ultra-violet frequencies, and therefore the permittivity of these noble metals is negative at optical wavelengths.

The parameters of the Drude model, ε_b, ω_{p} and γ, can be tuned to fit experimental data within a desired range; this provides a fit that can be used to define the permittivity of the metal for a wide range of frequencies. To globally fit experimental data on the other hand, additional models would need to be included as the free electron model is no longer sufficient to explain the characteristics of experimentally measured data. This can be seen by the deviation of the imaginary part of the Drude model (blue lines) to the experimental data of silver (dots) in figure 2.4 at short wavelengths. However, this is beyond the range of wavelengths used in this thesis ($\lambda_0 \sim 1550$nm) and therefore the Drude model is sufficient to model the permittivity of the metal.

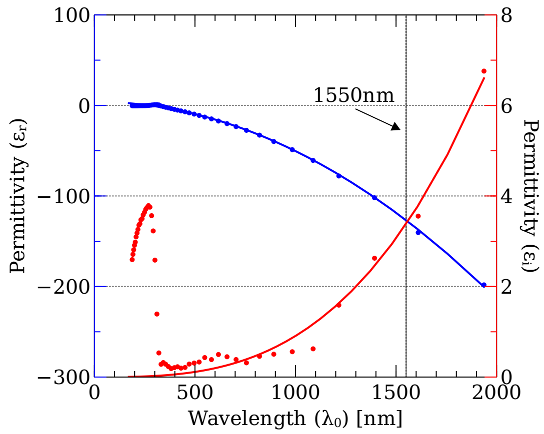

Figure 2.4: The Drude model fit (coloured lines) to the complex permittivity data (dots) for silver (Ag) taken from [51], using the fitting parameters $\varepsilon_\mathrm{b} = 4.05$, $\omega_\mathrm{p} = 1.39 \times 10^4$ THz and $\gamma = 31.4$ THz.

At an interface where the permittivity of the media changes sign, such as a dielectric (with a positive permittivity) and plasmonic metal (below its plasma frequency, and therefore with a negative permittivity), the formed plasmon is tightly confined to the interface between the metal and dieletric [7] (see figure 2.5). This surface plasmon (SP) has an electric field which decays exponentially away from the surface into the metal and the dielectric. Due to the SP being strongly confined at the interface, the electric field in the dielectric near the metal surface has a high field strength. This makes SPs sensitive to near-field conditions which makes them ideal candidates for applications such as sensing [14] or with the use of nonlinear materials whose responses are dependent on the field strength.

The surface plasmon is dependent on the plasma frequency of the metal and

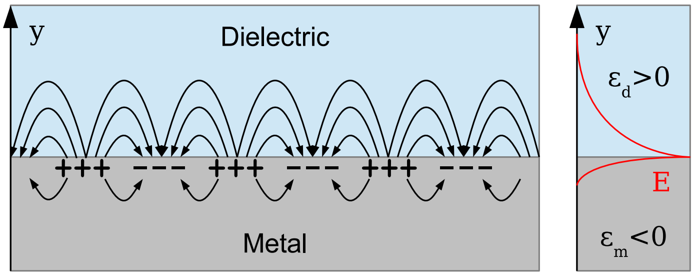

Figure 2.5: The surface charge (left) and electric field profile (right) for a surface plasmon at the interface between a metal and a dielectric.

the permittivity of the dielectric at the interface (here assuming $\varepsilon_\mathrm{b} = 1$)

$$\omega_\mathrm{sp} = \frac{\omega_\mathrm{p}}{\sqrt{1+\varepsilon_\mathrm{d}}}. \tag{2.13}$$

Light can couple with surface plasmons at surface of the metal forming surface plasmon polaritons (SPPs). These SPPs propagate along the interface and are generally short ranged due to the evanescent penetration of the fields into the lossy metal. It follows from Maxwell's equations that SPPs at the interface between a metal, characterised by its permittivity $\varepsilon_\mathrm{m} = \varepsilon_\mathrm{m}(\omega)$, and a dielectric $\varepsilon_\mathrm{d} = \varepsilon_\mathrm{d}(\omega)$ obey the dispersion relation [49]

$$\beta_\mathrm{spp} = \frac{\omega}{c}\sqrt{\frac{\varepsilon_\mathrm{m}\varepsilon_\mathrm{d}}{\varepsilon_\mathrm{m}+\varepsilon_\mathrm{d}}}, \tag{2.14}$$

where c is the speed of light in vacuum.

Figure 2.6 shows two example SPP dispersion graphs for a metal-dielectric interface where the dielectric is air and silica. For small wavevectors, the SPP dispersion closely follows that of the light-line of the dielectric medium. With increasing wavevector, the SPP dispersion drops away from light-line, asymptotically approaching the SP frequency of the metal-dielectric interface. For air ($\varepsilon_\mathrm{d} = 1$), the SP frequency is $\omega_\mathrm{sp} = \omega_\mathrm{p}/\sqrt{2}$. Below the SP frequency, the SPP wavevector is real and therefore the SPP is bound to the surface. Between the surface plasmon frequency and the plasma frequency of the metal, β_spp becomes purely imaginary (in the limit of a loss-less material), as no propagating electro-

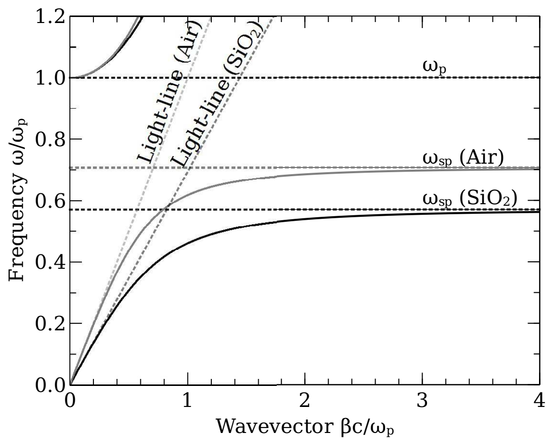

Figure 2.6: The surface plasmon polariton dispersion for metal-air and metal-silica interfaces, highlighting the light-lines for the two dielectrics and their relative surface plasmon frequencies.

magnetic mode is supported. Above the plasma frequency, the metal becomes transparent as propagating bulk modes are supported within the metal.

Plasmonic surfaces may be used to guide the SPP by the use of a defect in the surface, such as a groove or channel [52, 53]. These channels localise the SPP and guide it, often with high levels of light confinement [18]. With this control over the propagation of light, applications such as ultra-compact waveguiding plasmonic components can be realised [54].

The surface plasmons formed on small metallic particles are unable to propagate far due to the finite size of the particle. An oscillating electrical field across the particle causes a build up of electric charge at the edges of the particle [55], peaking when the particle size is resonant with the illuminating wavelength of light [56, 57]. These localised surface plasmon resonances (LSPRs) concentrate the fields at the particle extremes, even for off-resonant excitation or sub-wavelength particles, as explained by the lightning rod effect [36]. As sufficient field penetrates the metallic particle, LSPRs are highly lossy, especially when in resonance with the particle.

The restoring force from the ions in the metal provides the oscillation resonance of the LSPR, which is sensitive to both the size and shape [11, 58] of the particle as well as the dielectric environment [11, 59]. This allows LSPRs to be used with devices that benefit from high field enhancements, such as the sensing of changes in the dielectric environment [13]. Larger particles will support higher order LSPRs [60].

Nanoparticle LSPRs, with strong fields at their edges, can couple to particles in close proximity via near-field interactions [61]. This has been well explored for particle pairs [62], chains of particles [15, 63] and holes [64], and is increasingly explored in molecule clusters [65, 66] and arrays [67], giving rise to lattice surface plasmons. Lattice surface plasmons propagate energy along surface structures [68] given a sufficiently close proximity of the particles. Particles with large separation distances are unable to couple via their near fields but may couple via far field interactions allowing them to couple via radiative modes in much the same way as gratings [69, 70].

The next section will introduce the simulation methods used for the work of this thesis. The computational method builds upon the models and equations discussed in this chapter to find solutions to electromagnetic problems for specific structures.

2.4 Numerical Methods

Numerical studies of the interaction of electromagnetic fields with material environments are performed by computational electromagnetics. Maxwell's equations are used to provide efficient and accurate solutions to simulated problems in order to prepare, test and optimise new ideas and structures without the need for fabricating samples for experiments.

The simulations in this thesis make use of the finite element method (FEM) which finds approximate solutions to partial differential equations; Maxwell's equations in the case of electromagnetism. The differential equations are applied to small discrete finite elements of the full geometry. The discretised mesh can be adaptively refined for areas where a higher degree of accuracy is required, or where smaller geometric features are present. The FEM is used in this work to solve two particular problems. The first is a mode solver for a given geometry, the second is a scattering solver of a propagating electromagnetic wave through a geometry.

In mode solving problems either the magnetic or electric time-harmonic Maxwell's equations (equations 2.1) with geometric properties, such as the permittivity, permeability and sizes of the materials, and appropriate boundary conditions, can be used to find the solutions of a system at a given frequency. By providing the frequency value ω for equations 2.10 the partial differential equation becomes an eigenvalue equation, allowing for multiple eigenvalues, and therefore discrete solutions, to be calculated for one geometry.

In scattering problems the geometric properties are given for the computational domain in addition to incident (or source) electromagnetic waves on the structure. The electromagnetic response of the geometry to the incident light wave is calculated in terms of reflection, refraction and diffraction. The source light can either be a plane wave from a single-material boundary or from a previously solved mode for the matching geometry stack of the excitation boundary. Again, the Helmholtz equations are solved for the given geometry and boundary conditions, providing a steady-state (time harmonic) solution of the propagating mode in the system.

Two FEM software packages are used for the work of this thesis. JCMwave (www.jcmwave.com) (where the 'JCM' stands for James Clarke Maxwell) is a commercially available FEM software used for the majority of the mode solving and scattering calculations. COMSOL Multiphysics (www.uk.comsol.com) is also commercially available and is a more widely known FEM software package. COMSOL is specifically used to perform the isolated trimer calculations in section 4.1, due to the availability of a two-step process outlined in section A.2, and the mode-specific scattering calculations in section 4.3, due to the availability of the port boundary condition.

The right hand geometry in figure 2.7 shows an example simulation setup for out-of-plane scattering. The geometry is assumed to be infinite (or periodic) tangential to the interface, with an external light source impinging on the structure from an out-of-plane direction. The transmitted energy through the structure (the transmission, T) and the energy reflected back towards the source medium (the reflection, R) are obtained. Knowing the strength of the light source (incident energy, I), the absorption within the structure (A) can be estimated with $A = I - T - R$, assuming no other scattering channels are present. Out-of-plane excitation is commonly used to explore structures numerically and experimentally, as the simulated domains are small (being periodic) and the low number of scattering channels are relatively easy to measure.

The left hand geometry in figure 2.7 depicts a more complex example of an in-plane excitation method. The system consists of a waveguide which requires a previously solved waveguide mode to be injected. The energy from the waveguide can transmit (T) and reflect (R) within the plane, and with the addition of scattering objects, such as a surface structure, the light will additionally be scattered towards the top (t) and bottom (b) of the system. This provides additional scattering channels and therefore more information regarding the performance of the structure. As before, there is absorption (A) if lossy mediums are included. The scattering channel labelling and colours used in figure 2.7 will match those of subsequent scattering spectra.

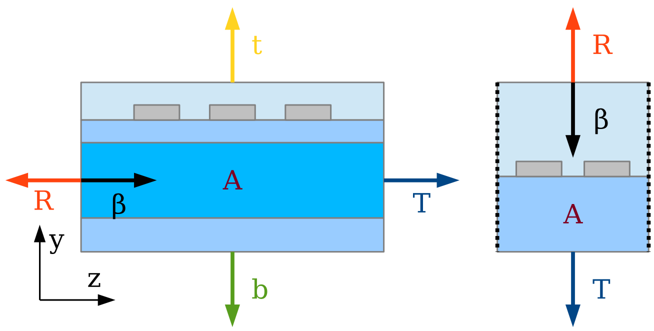

Figure 2.7: A comparison of the in-plane (left) and out-of-plane (right) setups. Introducing the transmission (T), reflection (R), top (t; superstrate) and bottom (b; substrate) scattering channels and the internal absorption (A).

The defining feature of all numerical simulations are the boundary conditions used for the edges of the computational domain. Boundary conditions greatly affect the solutions produced, such as forcing electric field polarisations at certain boundaries. The boundary conditions used for this work are described below.

The periodic boundary condition (PBC) dictates that the field values on one boundary must match that of the opposite boundary (with an optional phase shift to the complex field). This is useful for simulating infinitely large, periodic structures as only a single unit cell of the structure is required to model the behaviour of the full, infinite structure.

Perfect electric conductor (PEC) and perfect magnetic conductor (PMC) boundaries simulate perfect conductors of the electromagnetic field (electric or magnetic). The matching electromagnetic field tangential to the boundary interface is forced to be equal to zero. This is because the boundary is forced to have zero resistance (i.e. has perfect conductance) to the induced electric charge motion, inducing an identical field opposite the tangential field component completely cancelling the field. The PEC or PMC boundary conditions act as a perfect mirror for the given electromagnetic field allowing for a smaller computational domain than a periodic system (half that of the unit cell), assuming the unit cell has reflection symmetry. It also will force the particular TE or TM solution upon the system, depending on the choice of boundary condition used.

Perfectly matched layers (PMLs) are domains which extend the computational domain to simulate an infinite extension to a material at the boundary. PMLs enforce that all energy which passes into the PML will sufficiently exponentially decay to prevent reflections back into the computational domain. It can also be used as an external source under the assumption that the wave originates on the computational domain boundary and propagates into the computational domain. Therefore the incident light is not affected by the properties of the PML boundary.

Port boundaries are mode-specific scattering boundaries which only allow a certain (pre-solved) mode to transmit through them, reflecting all other contributions from other modes. Multiple ports may be applied to the same domain boundary to allow the transmission of multiple modes through the boundary and therefore enabling the calculation of mode-specific power flows.

The following two chapters utilise the FEM to explore the optical properties of the structures designed in this work.

Chapter 3

Integrated Plasmonic Surface Structures

This chapter introduces the hybrid dielectric-plasmonic waveguide as the platform for integrated plasmonic surface structures. Waveguide modes for the metal-covered and uncovered platform are explored, including the effects of the buffer thickness (and therefore the separation between the photonic waveguide and plasmonic surface) upon the loss associated with the modes. The study of a basic surface structure, the plasmonic grating, is presented in section 3.2, with the primary focus on controlling the coupling between the waveguide and radiative modes.

Plasmonic surfaces are increasingly being researched for their abilities to control the localisation [71, 72] and alter the propagation of light [73–75] on scales which are much shorter than the wavelength of light. The steady progression in nanolithographic techniques [16] for the fabrication of plasmonic surfaces has recently reached the levels of precision and accuracy required to create plasmonic structures with nanogaps towards the nanometre range [6]. This degree of precision enables surfaces to be made that are capable of subwavelength interaction with light that is unmatched by photonics for high-resolution devices [2].

The unique ability to collate light in the nanogaps between plasmonic particles [76, 77] and in thin metallic films [78, 79] has been extensively researched. As part of the growing interest in metamaterials, 2D metamaterials, often referred to as metasurfaces [30, 31], are being explored for their abilities such as being able to control the phase [80] and propagation direction [81–83] of lattice SPPs, to slow down light [84], and to create double negative materials [85]. However, plasmonic materials are inherently lossy; structures relying on plasmonics are typically characterised by having short operational lengths [86, 87] or require the addition of gain media [42, 43, 88] to amplify the signals in order to compensate for the losses.

One of the main aspects of this work is to explore an alternate method of overcoming the problem of the high losses associated with plasmonic structures while still maintaining the plasmonic effects of the surface structure. This can be achieved by combining the longer propagation lengths of photonic systems with the functionalisation of plasmonic nano-devices in an integrated plasmonic-photonic structure [44, 89]. Low index photonic materials used between a high index material and a plasmonic material are known to increase propagation lengths of SPP modes [90–92]. Hybrid structures have been extensively investigated, utilising photonic guiding [93–95], plasmonic guiding [45, 47] and even guiding provided by both photonic and plasmonic materials [89, 96–98]. Some hybrid structures have shown to produce slow light [99] or EIT like properties [100]. Most experimental research relies upon out-of-plane illumination of plasmonic surface structures or excitation using a SNOM probe [20, 101, 102]. The addition of a photonic waveguide provides a means of exciting a surface structure from within the structure's plane, for example plasmonic antennas [103, 104] and resonators/sensors [105, 106]. Such hybrid integrated systems offer one possibility to break the interdependency of loss and localisation of plasmonics, but require careful design to achieve good loss management in addition to compatibility with established photonic architectures. Using standard photonic platforms, such as silicon-on-insulator (SOI) or III-V semiconductors, it is possible to pattern the surface of the photonic platform with plasmonic materials which are indirectly (i.e. evanescently) driven by electric fields from the underlying photonic waveguide, combining the high propagation lengths of the photonic waveguide with the flexibility and functionalisation of the plasmonic surface structure.

The metallic surfaces also lend themselves well to Babinet's principle allowing for inverted designs of plasmonic structures [107, 108]. An inverted structure, i.e. a metallic surface with a hole array instead of an array of particles, would change the diffraction spectra of the surface structure. Although surfaces have been explored via out-of-plane illumination [109, 110] where the transmission and reflection features are seen to switch, a similar effect would be expected of the surface structure when illuminated in-plane, in regards to the scattering to the superstrate. The inverted structure would additionally need to be rotated to accommodate the electric field polarisation of the waveguide mode, as outlined by Babinet's principle [107].

Section 3.1 will introduce the silicon-on-insulator photonic platform used for the majority of this work and how the current applications and fabrication techniques help guide the choice of the geometric properties. It will then continue by charactering the platform in terms of the waveguide modes it can support, comparing the losses for the different field orientations and geometric setups. This includes the scattering caused when the guided mode impinges on an interface between the open (i.e. uncovered) and closed (i.e. metal-clad) setups and how the mode profiles change between the two setups.

Section 3.2 will explore the coupling into and out of the waveguide by the use of a plasmonic surface grating to phase match between the radiative and waveguide modes. This introduces the concept of phase matching, which is relevant to understanding some of the properties of the triangular nanogap tiling explored in chapter 4. The metallic grating is optimised, revealing some basic properties of periodic surface structures in the integrated configuration.

The next section shall introduce the integrated platform and the choice of material system and geometric parameters and the effects of some of the parameters on the waveguide modes.

3.1 Hybrid Photonic-Plasmonic Platform

For the integrated platform, a silicon-on-insulator (SOI) stack is considered as it is already an existing and extensively used platform for silicon-based electronics (e.g. CMOS), meaning that the fabrication of the silicon wafers is cheap and that they can be produced to a high degree of accuracy [111]. It is also commonly used in optical photonics as the compounds of silicon (i.e. silicon and silicon oxide) have a large refractive index difference, allowing for stronger electromagnetic wave confinement leading to smaller devices. Silicon and its compounds are highly transparent at the telecommunication wavelength (1550 nm) used by, for example, optical fibres. This makes SOI an ideal candidate for the photonic platform of the integrated device at this desired wavelength.

The SOI platform used in this work consists of a $w = 220\,\mathrm{nm}$ silicon ($\mathrm{n_{Si}} = 3.48$) waveguide, a thickness commonly used in silicon photonics allowing the device to be compatible with many other SOI photonic devices. The waveguide is thin enough to only support the fundamental TE and TM modes across its height. The silicon waveguide sits upon a semi-infinite silica substrate and is topped with a $b = 50\,\mathrm{nm}$ layer of silica ($\mathrm{n_{SiO_2}} = 1.44$) to act as a buffer layer to separate the waveguide from the plasmonic cover. The buffer layer needs to be thin to allow the evanescent field from the mode in the waveguide to be sufficiently strong to interact with the metallic surface. A thin $m = 30\,\mathrm{nm}$ layer of silver is applied on top of the buffer. The permittivity of the silver is approximated using the Drude model with the fitting parameters as previously shown in figure 2.4 and at $\lambda_0 = 1550\,\mathrm{nm}$ it takes on the value $\varepsilon_{\mathrm{Ag}} = -126.8 + \mathrm{i}3.38$.

To characterise the properties of the integrated device, two possible stacks are explored: the first structure is the photonic waveguide stack *without* metal deposited on top, hereafter referred to as the open system, and the second structure is the integrated platform *with* a metallic cover, referred to as the closed system. These two setups are shown in figure 3.1, along with the material and geometric properties. There is inherent loss within the closed system due to the inclusion of a plasmonic material (neglecting the much smaller loss within the silicon layers). The geometry of the platform and its guided modes are explored in order to tune and control the loss of the system.

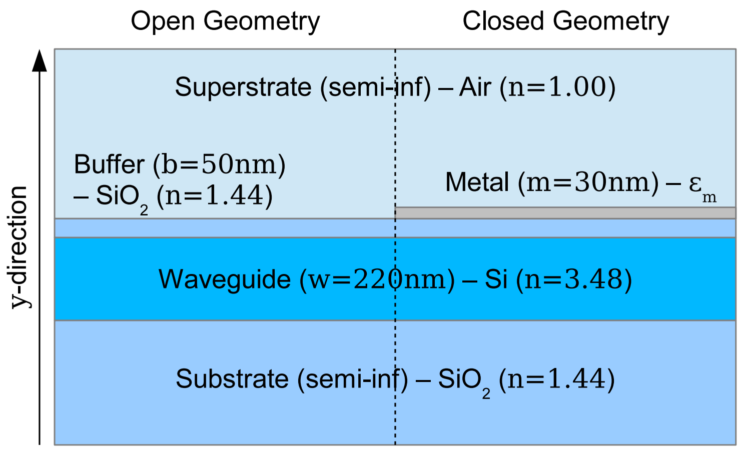

Figure 3.1: The silicon-on-insulator waveguide stack in the open (left) and closed (right) configurations.

The supported fundamental TE and TM waveguide modes for the open system are shown in figure 3.2. The TE mode has the electric field polarised in the x-direction, whereas the TM mode electric field is polarised in the y-direction. Due to this difference in the electric field polarisation, the interaction of the electric field with a given metallic surface will alter the attenuation received by the modes. Further analysis of the attenuation of the modes can be made to identify the mode with the least loss.

The profile of the electric field differs between the open and closed geometries. As the electric field for the TE mode is polarised in the plane of the waveguide, an electric field in the metal will be induced which counteracts the incident electric field at the surface ($E_{||} \approx 0$). This creates a node at the plasmonic interface [45] (see figure 3.3), therefore causing the mode shape to be

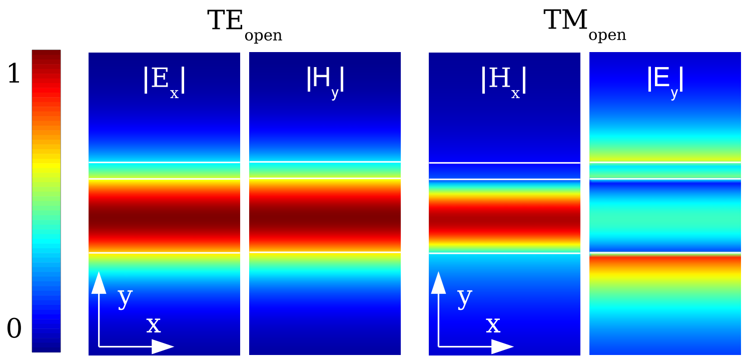

Figure 3.2: Comparison of the electromagnetic fields for the TE (left) and TM (right) waveguide modes for the open geometry.

affected by the proximity of the metallic layer; pushing the peak of the field away from the centre of the waveguide. The electric field of TM mode, on the other hand, is normal to the plasmonic surface. This allows it to hybridise with the surface plasmons [112], resulting in a proportion of the field energy being pulled into the buffer layer which lowers the effective index of the mode and increases the losses of the system as more of the field penetrates into the metal. Therefore, for the closed system, the TM mode is expected to have higher losses.

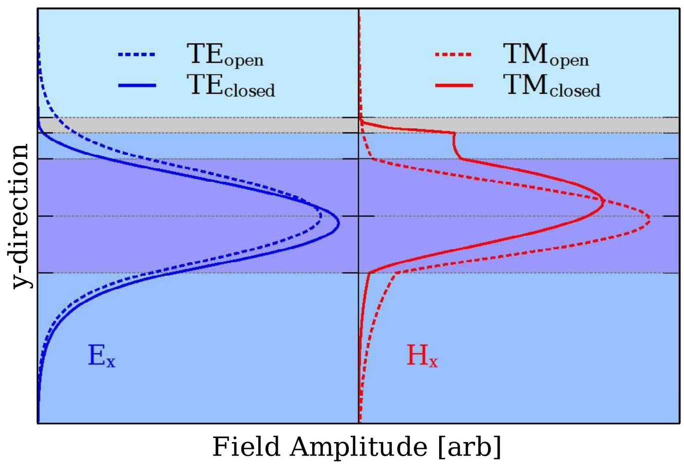

Figure 3.3: The x component of the electromagnetic fields of the TE and TM modes for both the open and closed geometries.

Additionally, since the fields either side of the waveguide layer are evanescent, the distance between the waveguide and the plasmonic cover will also greatly influence the loss of the system. Since the buffer layer separates the lossy plasmonic surface structure from the waveguide, the buffer layer thickness will affect the propagation length of the system. The propagation length is calculated with $\ell_\mathrm{p} = 1/\alpha$ where $\alpha = 4\pi n''_\mathrm{eff}/\lambda_0$ is the attenuation of the modal electromagnetic fields, which is proportional to the imaginary component of the effective refractive index of the given mode. The effect of the buffer layer thickness on the TE and TM fundamental modes for the open and closed systems can be seen in figure 3.4.

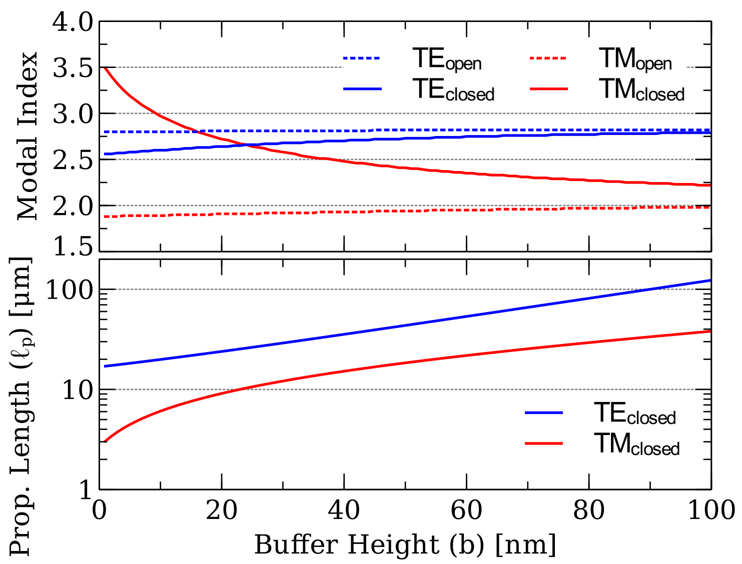

Figure 3.4: Model indices (top) and propagation length ℓ_p (bottom) for the open (dashed) and closed (solid) geometries for both the TE (blue) and TM (red) fundamental modes.

It is apparent from figure 3.4 that the effective index for both modes in the open setup (dashed lines) are only influenced to a small degree by the varying buffer layer thickness. As the thickness of buffer layer decreases, the proportion of modal fields in the air superstrate increases and, since air has a lower index than the buffer layer, the resultant effective index is reduced for both modes. However, with the closed system, the introduction of the metal cladding significantly impacts the modes. The TM mode, with its electric field component perpendicular to the metallic surface, has a substantially reduced propagation length in comparison to the TE mode due to the higher overlap of the electric field with the lossy plasmonic medium. This effect is stronger for a very small buffer layer thickness. The open system propagation lengths are not shown in figure 3.4 as they are much larger than that of the closed system.

How the mode scatters as it traverses from one system (e.g. the open system) to another (e.g. the closed system) is of specific interest as the scattering will differ for the two mode polarisations. As the TM mode hybridises with the plasmonic surface, the modal indices of the TM modes strongly differ between the open and closed systems. A strong impedance mismatch between the two waveguide systems for a given mode will have increased scattering (including reflection) of the energy at the interface between them. Specifically, the difference in mode index Δn for the TE case (at a buffer layer thickness of 50 nm) is -0.1, whereas for the TM case a much larger value of $+0.45$ is found (taken from figure 3.4).

The coupling efficiency of the modes between the open and closed systems can be obtained by the overlap integral of the modes between the systems, assuming both modes are well confined [113]. Figure 3.3 shows the x field component profiles for both the TE and TM modes, for the open and closed system. It is clear that there is a better overlap between the TE polarised mode than the TM polarised mode. Therefore, the TE mode is expected to have a higher coupling efficiency and less scattering at the interface between the two systems.

The reflection of the wave as it impinges the interface between two media of different impedances (for a non-magnetic material (i.e. $\mu = 1$)), can be calculated from Fresnel's equations, resulting in

$$\Gamma_{12} = \frac{Z_2 - Z_1}{Z_2 + Z_1}, \tag{3.1}$$

where $Z = \sqrt{\mu/\varepsilon} = 1/n_{\text{eff}}$ for a non-magnetic dielectric. For the interface between the open and closed geometries, the reflection for the TE and TM modes can be estimated using equation 3.1 from the effective indices of the two systems. This comes to around 1.7% for the TE case, and 10.5% for the TM case, at a buffer thickness of 50 nm. Since this assumes the two waveguide stacks as effective bulk dielectrics (i.e. it does not take into account the full geometric properties), the true scattering ratios and angles are not accurately determined. However, it strongly suggests that the TM mode will reflect/scatter far more than the TE mode at the interface between open and closed systems, simply by the change in effective index alone. This will have a large impact on the ability of the integrated system to contain the waveguide mode of the system when more complex structures (i.e. that repeatedly change between an open and closed system) on the surface are present.

The surface of the photonic platform can be patterned with metallic elements [16] to create an evanescently driven structure. The most common method to create metallic structures on a surface is nanolithography, encompassing a wide range of fabrication techniques, including direct deposition of the metal through a mask or stencil [114, 115] or etching out the shapes from a resist material before depositing the metal [116, 117]. These methods allow for the selective deposition of the metal with relatively high precision, down to the nanometer scale [6]. Electron beam lithography is suitable for research and development, but is considered less suitable for mass production due to its low throughput. Alternative methods include nano-imprint lithography [118, 119], which uses a mechanical stamp to imprint a pattern into the resist material with the ability to scale the structure [120] for higher or lower density lattices, self-assembly techniques [65, 121] using a self-assembled mask to define the pattern or manipulation of individual atoms [122].

Ideally metallic structures would have well defined features such as sharp corners or nanogaps between elements. However, due to fabrication tolerances, there is always some rounding or smearing of these corners and edges. Thicker layers of metal deposited on the surface would cause fabrication techniques, such as e-beam lithography, to produce poorer edges, reducing resolution and increasing deformations. It is therefore preferable to have thin layers of metal for the surface structure to allow for well defined features.

Metallic particles on the surface of the platform will be evanescently driven by the field from the waveguide mode. The evanescent field will cause a charge separation in the metal particles along the direction of the electric field, exciting LSPR modes. These modes are able to couple between neighbouring particles if the particles are sufficiently close [63]. The electric field of the TE mode excites an in-plane mode in the nanoparticle which will be able to directly couple with the in-plane particles [123]. The electric field of the TM mode, however, excites an out-of-plane mode which is still able to couple between particles but at a reduced strength due to the LSPR being normal to the surface structure [63]. As the waveguide mode propagates in-plane to the surface structure, the phase of the waveguide mode changes along the structure. This phase retardation along the lattice can be exploited by tuning the distance between particles in the longitudinal direction (i.e. the pitch of the structure).

The excitation of LSPRs in the plane of the surface structure by the TE mode is best suited for the plasmonic surfaces studied in this work. The attenuation of the TE mode is significantly lower than that of the TM mode and the modal index is affected less by the proximity of the metallic cover. The scattering of the TE mode when transferring between the open and closed systems is much smaller than that of the TM mode due to the higher overlap of the profile of the TE mode between the two systems and better impedance matching. The TE mode also allows for strong lateral charge separation within the metallic nanoparticles on the surface, which can be exploited to form spoof SPP modes which traverse the surface structures [124].

In the next section, the experimentally common coupling from an external light source to the waveguide is explored. This in-coupling is commonly done via the use of surface gratings. A plasmonic surface grating integrated to the waveguide platform introduced in this section is explored and optimised as a coupling mechanism between radiative modes and the waveguide modes.

3.2 Plasmonic Surface Grating

Thus far only the propagation of fields that are already present within the waveguide have been considered. In this section, the insertion of fields into (and equivalently scattering out of) the system are explored.

There are three primary methods of coupling to/from a photonic waveguide. The first is known as end-fire or butt-coupling and consists of direct coupling between the ends of one waveguide to another, such as an optical fibre and waveguide, or between plasmonic and photonic waveguides [125, 126]. For the hybrid device, this would mean positioning the end of an optical fibre on the side of the waveguide structure. This would potentially have an extremely poor efficiency due to the high mismatch of waveguide shapes (e.g. the circular fibre core to a slab waveguide, often smaller in width than the fibre diameter) and the gap between the two waveguides causing reflection and scattering. Additionally, this method would require access to the side of the device, making it less suitable for on-chip applications.

The second common method is via the use of a prism, altering the interface between the superstrate and the device, and allowing for refracted waves to couple to the waveguide with little scattering. This method is commonly used to excite SPPs by phase-matching the radiative light with the SPP [8].

The third method achieves in-coupling via the use of a grating. Gratings have been extensively studied since the 1900s due to their diffraction abilities which were seen to produce anomalies [127, 128] and other interesting effects such as energy gaps [129, 130], slow light [131] and transmissive resonances [132]. They are known to provide additional momentum to an incoming light wave, allowing it to couple to modes with effective indices larger than free space, such as that of a waveguide. Additional back reflectors may be used within the SOI wafer, allowing for higher coupling efficiencies [133].

Photonic gratings, etched into the waveguide itself [134, 135], are one type of grating which can be used to couple light from a fibre to the waveguide [136]. Alternatively, plasmonic gratings [137, 138] and particles [139] can be used. The hybrid device described in the previous section utilises metallic surface structures, making metallic surface gratings an ideal method for external light coupling for the hybrid device.

Through the introduction of the periodic structure to the surface of the integrated device, a photon incident on the structure can scatter with an additional phase which is equal to multiples of the grating period. This can be seen from the momentum transfer equation

$$k_{\mathrm{s}} \sin \theta_{\mathrm{s}} = \beta \sin \theta_{\mathrm{i}} \pm m k_{\mathrm{g}}, \tag{3.2}$$

where the scattered wavevector k_{s} at an angle θ_{s} can be calculated by the propagation constant of the incident wave β at an angle θ_{i} to the normal of the grating, with an integer multiple m of the momentum k_{g} added by the grating. For a grating of period (or pitch) Λ, the momentum given to the incident wave is the reciprocal of the lattice vector, $k_{\mathrm{g}} = 2\pi/\Lambda$.

It is important to note that the k-matching condition works both ways: i.e. it can be used to calculate the coupling of a waveguide mode to a radiative mode, and also coupling to the waveguide from a radiative mode. For example, an optical fibre end firing onto the top of the grating at a slight angle would require a specific grating period to couple the wavevector of the mode from the fibre to the propagation constant of the waveguide. It is necessary for the fibre to be at an angle to the surface in order to get the coupling to one propagation direction of the waveguide, as the forward and backward propagating modes require different phase matching and therefore couple at different periods. Coupling directly to the normal of the structure $\theta_{\mathrm{s}} = 0°$ would equally couple to both the forward and backward modes of the waveguide as they would couple for the same period.

The integrated platform can be fabricated with a plasmonic grating on top of the SOI structure (figure 3.5), separated from the waveguide by the buffer layer. The guided mode cannot directly interact with the grating due to the confinement from the waveguide, however the evanescent field of the mode will be influenced by the plasmonic surface grating.

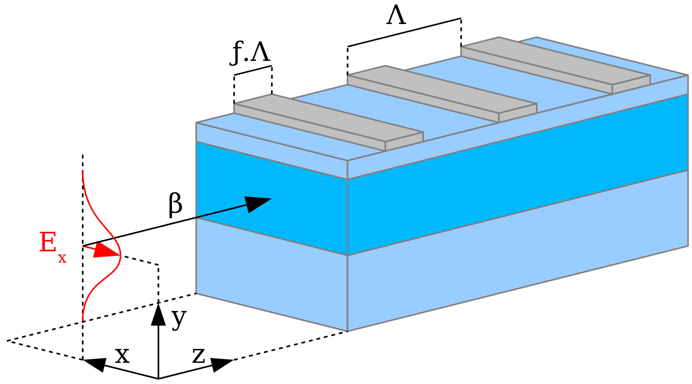

Figure 3.5: The integrated plasmonic surface grating, illuminated by the in-plane fundamental TE mode.

Since a surface grating would extend for many wavelengths in the x-direction, it can be assumed to be infinite in this direction, allowing for the grating geometry to be represented in two dimensions (the yz-plane). Normally, the performance of a single grating is explored for a range of frequencies of the incoming light. This method explores the ratio between the wavelength of the light in the waveguide and the longitudinal geometry of the grating. However, changing the frequency (and therefore the wavelength) of the incident light would result in different modal indices of the waveguide mode, thereby changing the overall confinement of the guided mode and the interaction with the surface structure. To explore the grating without a change in the confinement of the waveguide, the frequency is held constant and a geometric scan of the longitudinal period (the pitch, Λ) is numerically studied. This allows for the exploration of the ratios of the wavelength of the guided wave ($\lambda_{\text{eff}} = \lambda_0/n_{\text{eff}}$) to structural features (e.g. Λ) without affecting the confinement of the mode within the waveguide. Full details of the simulation setup can be found in the A.1 methods section.

With this in mind, the geometric parameters of the grating can be optimised to improve the ability of the grating to couple between the waveguide and external radiation modes (i.e. to/from an optical fibre above the grating) [136]. The ratio between the width of the metallic element and the period of the grating (known as the element's filling factor, f) is explored. A very small filling factor would mean very little metal is present on the surface, similar to the open system, whereas a high filling factor would make the grating appear closer to that of the closed system. Using previous iterations of optimised geometries to determine the values for the other geometric parameters, the filling factor is explored in the top image of figure 3.6 at a pitch of $\Lambda = 500\,\text{nm}$ (before the dip in out of plane scattering). Clearly seen is a broad peak in the out-of-plane scattering, both to the substrate (green) and superstrate (yellow), centring around the filling factor $f = 1/3$. Next the number of elements that make up the grating is explored, shown in the lower right graph of figure 3.6, as this relates to the overall length of the grating. The ability of the grating to couple energy to the free-space modes clearly increases with the number of elements. However, out-of-plane scattering is reduced by adding *additional* elements to the grating as there is less energy available to be scattered due to attenuation and scattering by previous elements. Finally, to show the tunability of the integrated structure, the buffer layer separating the plasmonic surface from the waveguide is varied to explore the evanescent coupling between the two structures. It is clear that a thicker buffer layer weakens the ability of the plasmonic grating to scatter light from the waveguide due to the weaker evanescent tail of the waveguide at larger distances.

Using the optimised values for the geometric parameters, the effect of the pitch of the grating is explored. Keeping the filling factor of the elements constant ($f = 1/3$) and setting the buffer to the relatively thin $b = 50\,\text{nm}$, for $N = 20$ elements in length, the scattering and absorption of the grating is explored between the pitch ranges of $\Lambda = 200\,\text{nm}$ to $1000\,\text{nm}$, and is shown in figure 3.7.

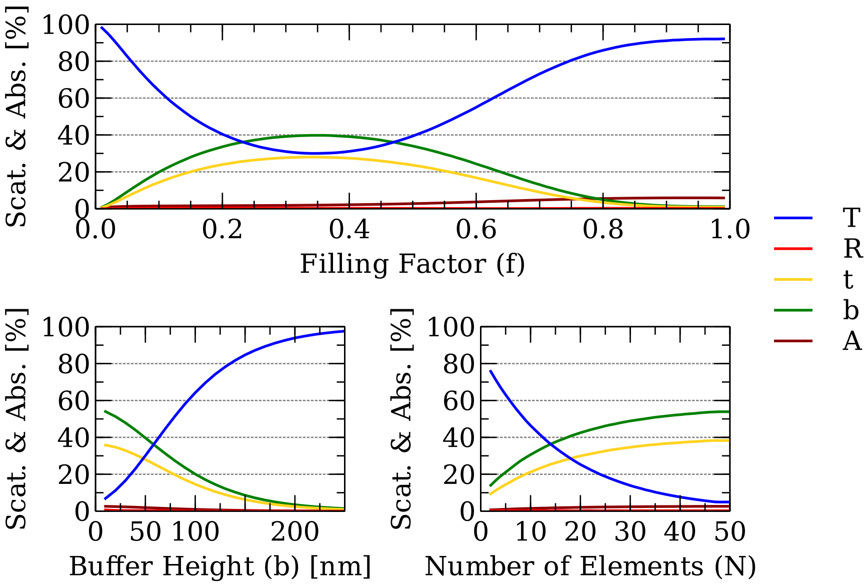

Figure 3.6: Optimising the filling factor f (top) of the integrated surface plasmonic grating and exploration of the buffer layer thickness b (bottom left) and number of elements N (bottom right) parameters.

There are distinct spectral features relating to a variety of responses. Firstly, there is a broad band between 400 nm and 900 nm where out-of-plane scattering (green and yellow lines) is prominent, in addition to distinctive reflection peaks.

Taking the k-matching condition 3.2, for the specific case of the integrated structure, the incident light on the structure is the mode propagating within the waveguide $\beta = n_{\text{eff}} k_0$, at an angle of $\theta_{\text{i}} = -90°$ to the normal of the surface of the platform (i.e. within the waveguide). Knowing that $k_0 = 2\pi/\lambda_0$, equation 3.2 may be re-written in the form

$$\Lambda = \pm m \frac{\lambda_0}{n_{\text{s}} \sin\theta_{\text{s}} - n_{\text{eff}}}, \tag{3.3}$$

which provides the means to estimate the grating period required to scatter the guided light into material n_{s} at an angle θ_{s}. Using this equation, the range of diffraction from the platform can be estimated: Taking the superstrate (air) as an example ($n_{\text{s}} = 1.0$), the limits for the out-of-plane scatter ($\theta_{\text{s}} = [-90°, 0°, 90°]$)

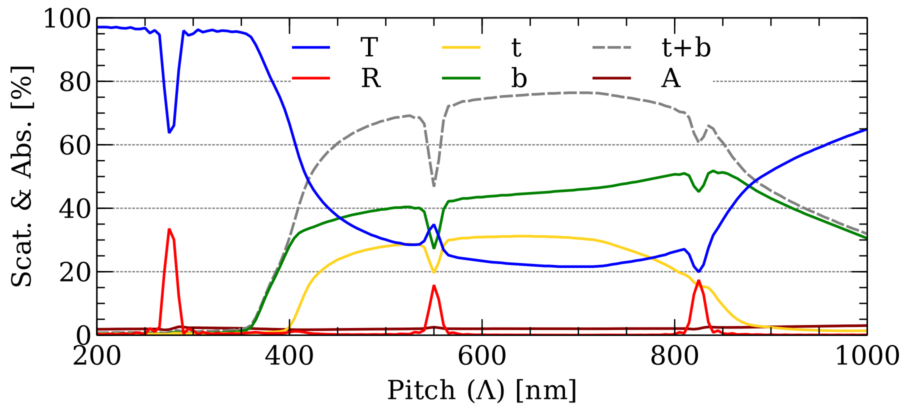

Figure 3.7: The transmission (T), reflection (R), top (t) and bottom(b) scattering and absorption (A) spectra for the integrated surface plasmonic grating.

for the TE mode of the open waveguide ($n_{\text{eff}} = 2.845$, taken from figure 3.4) at $\lambda_0 = 1550\,\text{nm}$ can be estimated as $\Lambda = [403.1\,\text{nm},\ 544.8\,\text{nm},\ 840.1\,\text{nm}]$.

There is a small difference between the values estimated above and the out-of-plane scattering spectra, as is most noticeable by a small deviation of the characteristic dip in transmission near the 0° location. This is because the effective index of the open system has been used, whereas the (unknown) effective index of the grating is required to accurately describe the full system using this equation. Using the location of the perpendicular out-of-plane scattering ($\theta_s = 0°$) as a guide along with equation 3.3, the effective index of the grating can be estimated to be $n_{\text{eff}} = 2.815$. Using this grating effective index, the limits for scattering can be estimated again, and are shown as dotted lines in figure 3.8, along with similar calculations for the substrate scattering ($n_s = 1.44$). The pitch values ($\theta_s = [-90°,\ 90°]$) are $\Lambda = [406.3\,\text{nm},\ 854.0\,\text{nm}]$ for air and $\Lambda = [364.3\,\text{nm},\ 1127.3\,\text{nm}]$ for silica (plotted as dashed lines in figure 3.8). These values match very well with the onset of out-of-plane scattering to both the top and bottom interfaces and the reduction in bottom scattering due to the onset of top scattering at $\Lambda = 406.3\,\text{nm}$. Outside of the limits, the energy is unable to match the phase with the radiation modes, resulting in a near zero out-of-plane scattering.

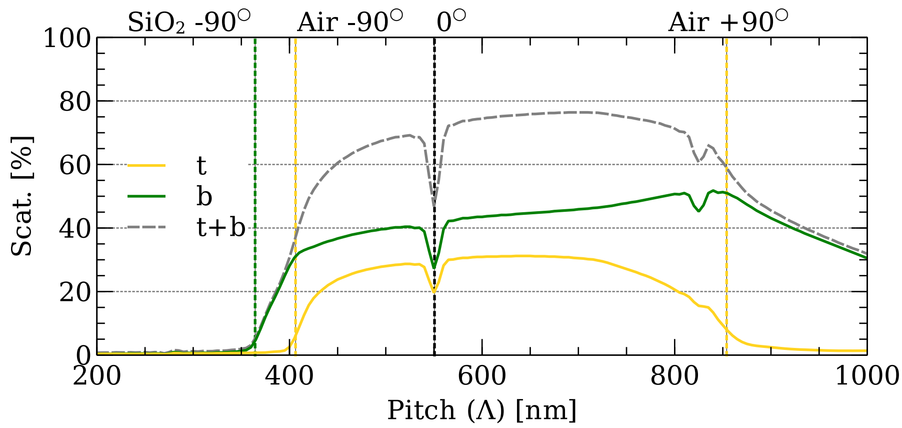

Figure 3.8: The top (t) and bottom (b) scattering spectra for the integrated surface plasmonic grating highlighting the out-of-plane coupling angles from equation 3.3 marked with dashed lines.

Using the effective index estimation of the grating in equation 3.3 with $\lambda_0 = 1550\,\mathrm{nm}$, the scattering of the grating at any angle between $\pm 90°$ can be given for the substrate or superstrate. To visualize the fields within the system, the electric field component E_x for the scattering angles $\theta_s = \pm 45°$ in air are plotted in figure 3.9. The coupling to both a forward and backward direction are possible by simply changing the grating pitch. The pitches for the $+45°$ and $-45°$ scattering angles in the air superstrate are around 440 nm and 735 nm respectively. Since the number of elements is held constant at $N = 20$, the total length of the structure varies significantly between the two pitches.

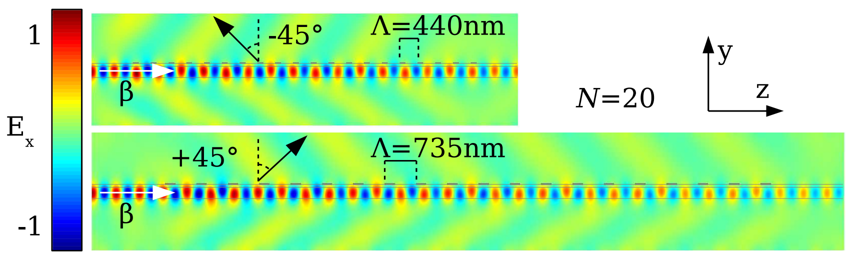

Figure 3.9: The x component of the electric field of the integrated plasmonic surface at the pitches required to couple the waveguide mode with the 45° radiation modes.

It was noted that there are distinct reflection peaks in figure 3.7. The grating effectively alternates between the open and closed geometries, with each part having a different effective index. At each effective interface between the alternating geometries, the propagating light will be partially reflected (as described by the Fresnel Equations). When the wavelength of the propagating light is in resonance with the period of the alternating layers, the partial reflections will constructively interfere, resulting in a strong resonant back-scattering into the waveguide. As a result, a transmission stop-band forms. This occurs as a special case of the k-matching equation when the pitch is equal to multiples of the half-wavelength [140], known as the Bragg condition. Such Bragg reflections manifest as transmission stop-bands in such structures, and are seen in many different waveguide setups [141].

Using equation 3.3, but setting the scattering medium to the effective index of the waveguide $n_\mathrm{s} = n_\mathrm{eff}$, at an angle of $\theta_\mathrm{s} = -90°$ (i.e. reflection), the equation can be reduced to

$$\Lambda = \frac{m\lambda_0}{2n_\mathrm{eff}}. \tag{3.4}$$

Using this equation and the effective index of the grating, the period of the grating where the first Bragg reflection occurs ($m = 1$) can be estimated to be at $\Lambda = 275.3\,\mathrm{nm}$, which matches the reflection peak in the scattering spectrum of the grating (see figure 3.7). Since the resonant back-scattering occurs every time the maxima of the reflective waves constructively interfere, a reflection peak should occur every m multiple of the Bragg period calculated above. The pitch locations for the $m = [1, 2, 3]$ Bragg resonances are $\Lambda = [275.3\,\mathrm{nm}, 550.6\,\mathrm{nm}, 825.9\,\mathrm{nm}]$. These are additionally plotted in figure 3.10. The calculated values match very well with the observed spectrum, identifying the reflection peaks as resonant back-scattering due to the Bragg condition.

The $m = 2$ Bragg reflection peak (B2) coincides with the $\theta_\mathrm{s} = 0°$ out-of-plane scattering, for at this angle the $n_\mathrm{s} \sin\theta_\mathrm{s}$ term is reduced to zero, rendering the permittivity of the scattering medium redundant. The k-matching equation then reduces to the Bragg equation, providing the characteristic dip in the out-

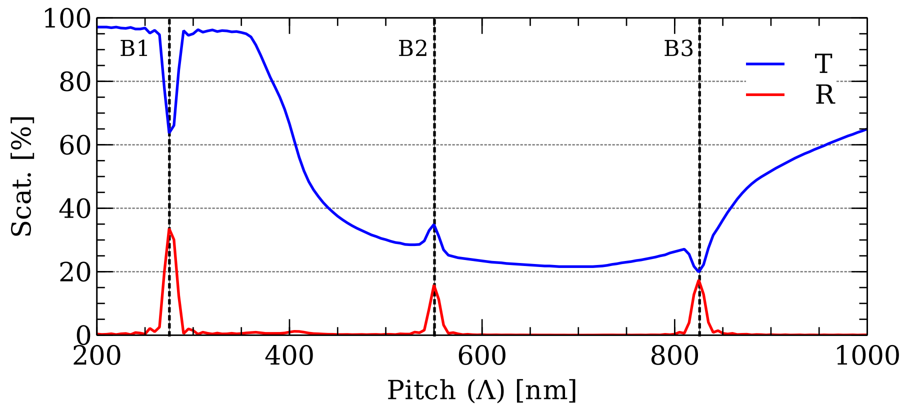

Figure 3.10: The transmission (T) and reflection (R) scattering spectra for the integrated surface plasmonic grating highlighting the Bragg reflections from equation 3.4 marked with dashed lines.

of-place scattering spectra as a large portion of the energy of the propagating mode is coupled back into the waveguide instead being of scattered out-of-plane.

It is also possible to observe this effect in a purely dielectric stack of alternating layers using the effective indices of the open and closed waveguide as the two alternating dielectric media. This correctly recreates the resonant reflection peak positions as seen in spectrum of figure 3.11.

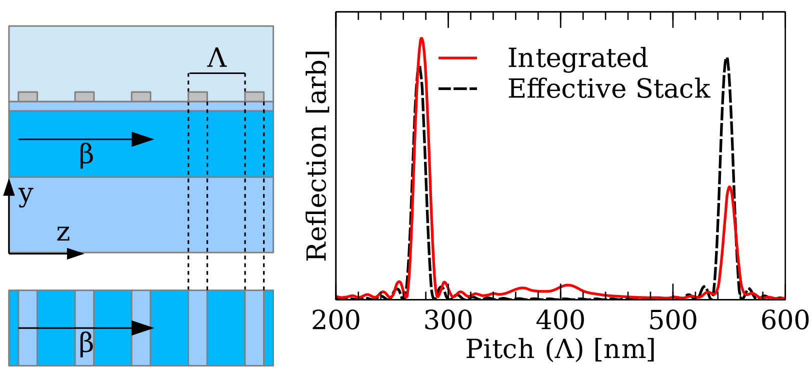

Figure 3.11: The geometries (left) of the integrated surface plasmonic grating (top) and effective dielectric stack (bottom), with a comparison of the reflection (R) scattering spectra (right). The reflection data are rescaled for comparison.

The grating provides a workable means of coupling an external electromagnetic source (e.g. from an optical fibre) to the photonic platform, which is important for the experimental realisation of the integrated device. The ability of the grating to scatter the electromagnetic field from the waveguide to radiation modes was optimised by tuning the parameters of the grating geometry. The k-matching condition to calculate the momentum required to phase-match the waveguide and radiation modes was tested against the numerical simulations, where it was found to provide a good agreement.

The designed photonic platform in this chapter will be used as the platform for integrated plasmonic surface structures introduced in the next chapter. Some of the features seen in the spectrum of the plasmonic surface grating are also present in the spectra of the introduced surface structures. Therefore the exploration of the grating, and the physics associated with it, provides a basis to readily identify these spectral features.

Chapter 4

Plasmonic Nanogap Tilings

This chapter introduces and studies a particular class of surface structure: plasmonic nanogap tilings (NGTs). Plasmonic nanogap tilings are regular periodic patterns of metal patches which can be fabricated on the surface of the photonic waveguide stack introduced in previous chapters. NGTs can be compared to plasmonic crystals, which in turn are similar to photonic crystals, both of which have been investigated for their optical properties such as slow light [142], scattering [143] and field enhancement useful for nonlinear processes and Raman scattering [144, 145]. Additionally, as the element size approaches subwavelength scales, the surface NGT structure becomes a metasurface [30], a 2D metamaterial. Metamaterials and plasmonic structures are being extensively research for their abilities to provide the double-negative index required for negative refraction [26], to slow and stop light [142], and for their band structures [146]. NGT structures are of particular interest due to the close arrangement of the metallic nanopatches on the surface resulting in a dense lattice of nanogaps between the elements [147]. The nanogaps allow for light to concentrate between the plasmonic elements [148], resulting in strong surface field enhancement and confinement; a property highly desirable for use with intensity-sensitive applications such as the inclusion of gain [43], sensing [14, 41] and the use of non-linear materials [144].

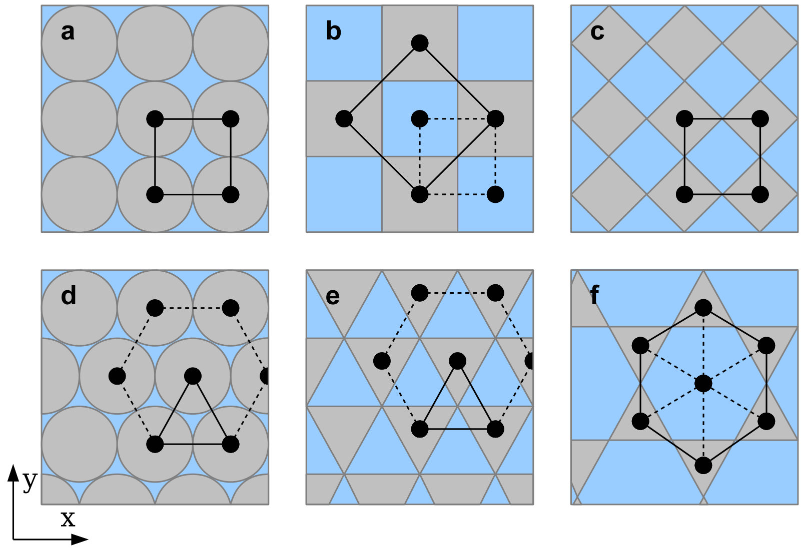

Figure 4.1: Examples of nanogap tilings: a) circular patches on a square lattice, b) square patches on a square lattice, c) diamond patches on a square lattice, d) circular patches on a triangular lattice, e) triangular patches on a triangular lattice, f) triangular patches on a hexagonal lattice. Primary lattices are solid lines, with dotted lines as alternate lattices.

A major function of the NGTs are their capacity to enhance light fields in the nanogaps between the plasmonic elements. Due to the physics outlined in section 2.3, this is heavily dependent on field polarisation, element shape and the structural lattice, allowing for the properties of the structures to be engineered [149].

To study the properties of NGTs, the triangular nanogap tiling (figure 4.1e) is explored in detail. The choice of a fixed triangular patch arranged in a triangular lattice is governed by the motivation to focus light into a dense array of nanogaps as well as the ability of the triangle patch to enhance fields while maintaining a relatively small effective size [150]. For comparison, the C_{4v} diamond tiling (figure 4.1c) has four axes of symmetry, and for a given electric field polarisation, i.e. a horizontal polarisation, only *half* of the nanogaps are excited: those with a horizontal separation. The C_{3v} triangular tiling (figure 4.1e) has fewer axes of symmetry than the diamond tiling and, for the same electric field polarisation, *all* the nanogaps are excited due to each having a component of horizontal separation. Therefore, the TE polarised light of the underlying waveguide can excite all the nanogaps of the triangular NGT, leading to a denser array of hot-spots in comparison to the diamond tiling. In addition, the triangular shape of the elements effectively acts as a taper that focuses light into the nanogaps [151] when orientated with the point of the triangles against the direction of wave propagation.

As a first step to characterising the triangular nanogap tiling, the scattering and hot-spot response of an isolated trimer molecule is explored in the following section, before continuing to study the full arrangement of the triangular NGT.

4.1 Isolated Trimer Molecule

The trimer molecule (figure 4.2) is the fundamental molecule of the triangular NGT. In a dense arrangement, the triangular NGT can be seen as a collection of strongly-coupled individual trimer molecules. Therefore studying the optical properties of the isolated trimer molecule would assist in understanding the optical properties of the integrated triangular NGT. The trimer molecule is driven by the evanescent fields from the underlying waveguide. The fields concentrate at the focal point of the nanogap via evanescent interaction of the plasmonic trimer molecule with the TE polarised waveguide mode.

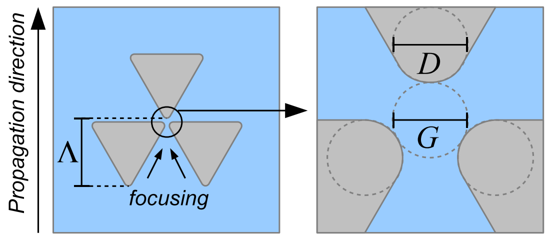

Figure 4.2: The backwards orientated trimer molecule with the pitch Λ, corner rounding diameter D and gap size G, where $D = G = \Lambda/10$, additionally showing the expected focusing effect.

Each triangular element, and the trimer molecule, has a C_{3v} symmetry. Setting the propagation of the driving photonic mode to one of the symmetry axes will result in two directions of excitation. These shall be refereed to as the forward and backward orientations or propagation directions. To clarify these directions, the forward direction is declared as the mode propagating *with* the point of the triangle (denoted as β^+) and backwards is declared as propagating *against* the point of the triangle (denoted as β^-). These two propagation modes can be used to excite the LSPR modes of the triangular patch [152] and trimer molecule [153]. The ability of the trimer to focus light into the nanogap is affected by the orientation of the triangles. In the backwards propagation orientation, the evanescent energy of the waveguide mode is effectively tapered into the nanogap [151]. This is expected to increase the light concentrating ability of the trimer and therefore this orientation will be primarily explored to maximise the effective nanogap enhancement.

To characterise the trimer molecule a pitch length Λ is defined, which is the length of the unit cell of a single triangular element along the axis of propagation. The actual height of the triangular element (tip-to-base length) will be smaller than this pitch length due to the nanogaps. The nanogaps between the elements are given by a circular distance with diameter G (see figure 4.2). The pointed tips of the triangular elements allow for high field strengths to build up due to the lightning rod effect [36]. However, sharp features are often difficult to fabricate due to manufacturing tolerances, resulting in a softening or rounding of the corners and edges. To model this fabrication feature and to reduce computational errors around very sharp features, the triangular elements are given a corner rounding of diameter D. Both the corner rounding and nanogap distance are set to scale proportional to the pitch ($G = D = \Lambda/10$), providing a simple model in which to scale the structure by.

The trimer molecule is integrated with the previously introduced photonic platform (figure 4.3). The thickness of the metal layer which forms the trimer molecule is set to the thin thickness of 30 nm. The trimer is separated from the 220 nm silicon waveguide by a 50 nm buffer layer of silica. The waveguide is placed on a silica substrate, and the trimer is exposed to air. Details of the simulation process to obtain the scattering data of the trimer molecule can be found in the A.2 methods section.

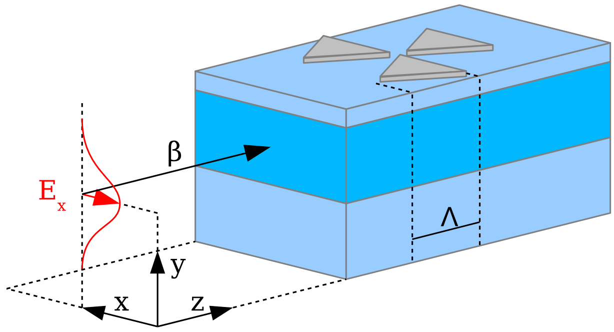

Figure 4.3: The integrated plasmonic trimer molecule, illuminated by the in-plane fundamental TE mode.

The timer molecule is illuminated by the waveguide mode at the telecommunication wavelength $\lambda_0 = 1550\,\mathrm{nm}$. The effect of the changing molecule size (i.e. its pitch Λ) in relation to this wavelength is explored, similar to the grating setup before. This keeps the confinement of the waveguide mode constant.

The trimer molecule will absorb and scatter energy from the underlying waveguide mode into various in-plane and out-of-plane scattering channels for the different boundaries of the geometry. The normalised scattering cross section and absorption is shown in figure 4.4.

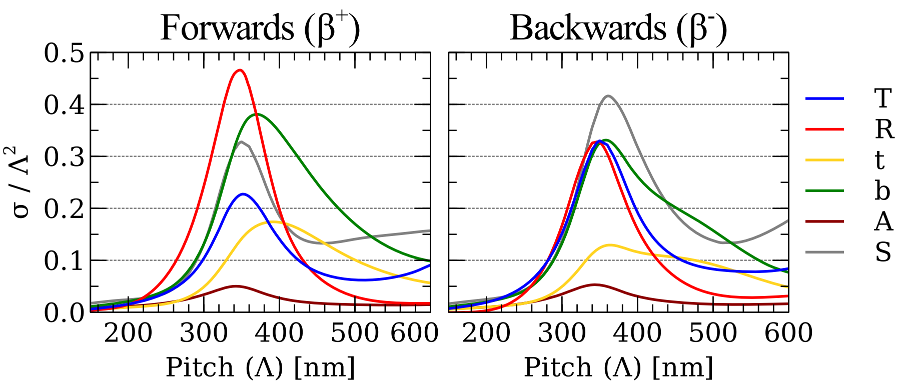

Figure 4.4: The normalised transmission (T), reflection (R), top (t), bottom (b) and side (S) scattering and absorption (A) cross sections of the isolated trimer in both the forward (left) and backward (right) excitations.

The scattering spectra for the trimer molecule indicates a clear dipole resonance at around $\Lambda \approx 350\,\mathrm{nm}$. The top scattering is relatively weaker than the other scattering channels due to the larger mismatch in impedance between the effective index of the waveguide and the air superstrate. The absorption channel is weak in comparison to the scattering as the molecule cannot be considered small compared to the effective wavelength of the waveguide mode. There is a slight shoulder in the scattering spectra of the top and bottom scattering channels at $\Lambda \gtrsim 450\,\mathrm{nm}$. This feature is more prominent in the backwards orientated trimer, and suggests the presence of another radiative resonance or the onset of out-of-plane scattering due to the resonance with the molecule spacing.

To quantify the ability of the trimer molecule to concentrate the evanescent fields, the average electric field of a small volume at the corners of the trimer molecule are normalised against the field amplitude of the same position if the trimer was not present, i.e. $\eta^{(\mathrm{E})} = |\mathrm{E}(\mathbf{r})|/|\mathrm{E}_0|$, where $\mathrm{E}(\mathbf{r})$ is the surface field amplitude at the given corner.

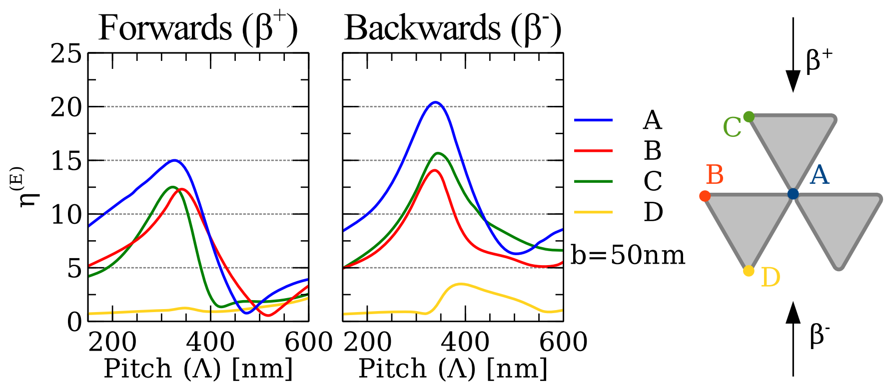

Figure 4.5: The normalised corner field enhancement of the integrated plasmonic trimer molecule (diagram inset) for both the forward (left graph) and backward (right graph) excitations.

The corner enhancements of the trimer molecule are shown in figure 4.5. The relative enhancements of the electric field are largely independent of the buffer thickness as the waveguide mode is not significantly perturbed due to the evanescent interaction. The backward excited trimer molecule has a stronger field enhancement at the central nanogap A, confirming the focusing effect of the triangular shape. With the increasing pitch of the molecule, the plasmonic trimer resonates with the waveguide mode at $\Lambda \approx 338\,\text{nm}$ and the relative field enhancement of the central point increasing to $\eta_{\text{A}} \approx 20$ for backwards excitation. For longer pitch lengths, the size of the molecule becomes larger than the effective wavelength of the waveguide mode and wave retardation effects become apparent, such as additional nodal planes appearing across the molecule and the excitation of higher order modes. This retardation effect leads to the illumination of the otherwise dark corner D, and causes a decrease of the enhancement in the centre nanogap as the lateral resonance weakens.

The trimer molecule has a strong dipole resonance at a pitch length $\Lambda \approx 350\,\text{nm}$, with simultaneously high field strengths in the primary focal point in the centre of the molecule. The evanescent field is effectively funnelled into the primary nanogap by the triangular shape of the elements. The strong fields at the outer corners of the molecule, corners B and C, allow for the trimer molecule to capacitively couple with neighbouring molecules if placed in a dense array such as the triangular nanogap tiling, forming larger lattice resonances.

In the next section the trimer molecule, as defined above, is placed in a dense arrangement on the photonic platform, resulting in a triangular nanogap tiling surface structure. The response of the nanogap tiling is explored in detail by characterising the scattered fields and the field enhancement effect.

4.2 Triangular Nanogap Tiling Spectra

Having established the scattering, absorption and light concentrating ability of the surface mounted isolated trimer molecule, the additional effects of the close proximity within the triangular nanogap tiling (NGT) can be characterised. The triangular NGT is of particular interest due to the dense arrangement of hot-spots associated with this tiling.

The trimer molecules are arranged in a triangular lattice with lattice vectors

$\overrightarrow{a_1}$ and $\overrightarrow{a_2}$, as seen in figure 4.6, which can be related to the pitch Λ of the structure by $\Lambda = |\overrightarrow{a}|\sqrt{3}/2$. As with the trimer, the nanogaps and corner rounding of the triangular NGT are chosen to scale with the pitch of the tiling pattern.

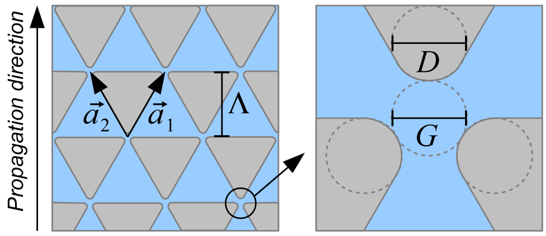

Figure 4.6: The backwards orientated triangular NGT with the lattice vectors $\overrightarrow{a_1}$, $\overrightarrow{a_2}$, pitch $\Lambda = |\overrightarrow{a}|\sqrt{3}/2$, corner rounding diameter D and gap size G, where $D = G = \Lambda/10$.

The triangular NGT is placed on top of the photonic platform (see figure 4.7). The waveguide is a 220 nm layer of silicon and guides the $\lambda_0 = 1550$ nm TE mode, with a 50 nm silica buffer layer separating the waveguide from the surface structure. Further details for the simulation setup, including the scattered fields calculation, can be found in the A.1 methods section.

The triangular NGT is evanescently illuminated by the TE waveguide mode. The full geometry has 25 triangular backwards orientated patches in the propagation direction. The effects of the pitch Λ of the surface structure on the abilities of the structure are studied.

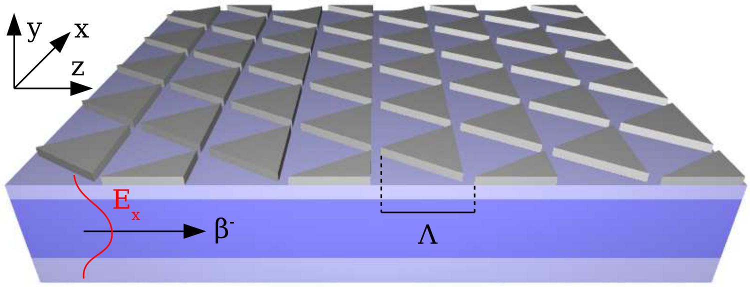

Figure 4.7: The integrated plasmonic triangular NGT, illuminated by the in-plane fundamental TE mode.

The full scattering and absorption spectrum (figure 4.8) reveals multiple resonances relating to photonic, plasmonic and radiative effects. Each of these effects will be discussed individually in the following paragraphs.

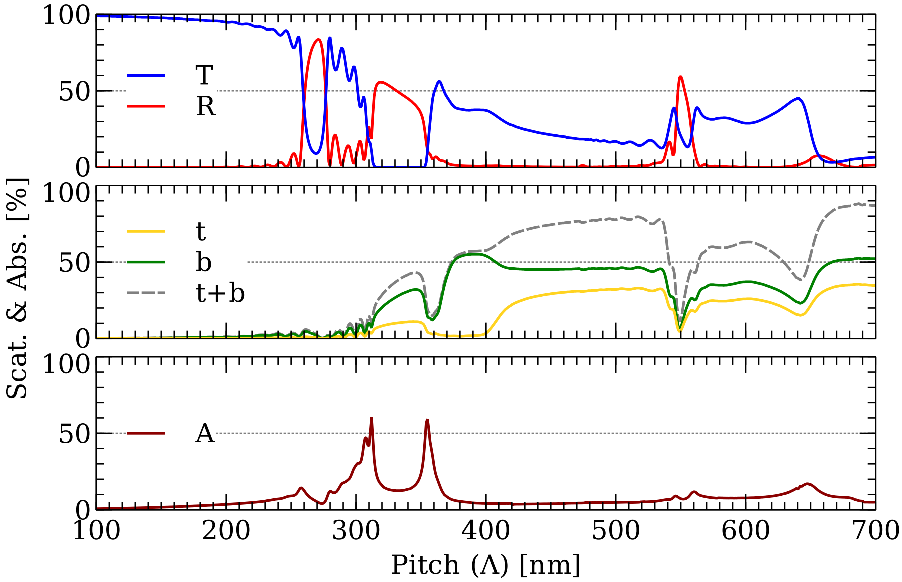

Figure 4.8: The transmission (T), reflection (R), top (t) and bottom(b) scattering and absorption (A) spectra for the triangular NGT consisting of $N = 25$ elements in length.

The triangular NGT features two strong peaks in the reflection spectrum (see figure 4.9) due to the Bragg reflections of the system, similar to those seen before in the surface grating. These photonic resonances are due to the surface structure changing the effective index of the waveguide modes and occur when the phase retarded waveguide mode matches multiples of half the pitch. Using the Bragg equation with the estimated effective index of the triangular NGT structure taken from the second reflection peak centre ($n_{\text{eff}} = 2.82$), the Bragg peaks for the $m = 1, 2$ conditions are expected to be located at a pitch of $\Lambda_{\text{B1}} = 274.8\,\text{nm}$ and $\Lambda_{\text{B2}} = 549.6\,\text{nm}$, as marked in figure 4.9.

Similar to the process performed for the metallic grating, an effective index dielectric stack structure can be used to explore the principles of Bragg reflection. However, the comparison of the triangular NGT structure differs from that of the grating (where the effective index of the structure changes periodic-

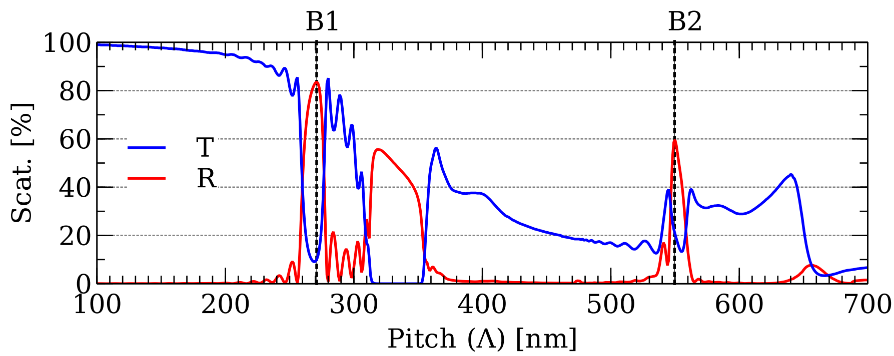

Figure 4.9: The transmission (T) and reflection (R) spectra for the integrated triangular NGT structure highlighting the Bragg reflections B1 and B2 with dashed lines.

ally between the open and closed effective indices of the waveguide) due to the triangular NGT being structured along the propagation direction. The effective index of the triangular NGT gradually varies from the open effective index at the very tip of the triangle point to the (nearly) fully covered (closed) effective index at the base of the triangular element. This forms a sawtooth-like variation in the effective index. Along the sloped edge of the saw-tooth oscillation, a continuous partial reflection can be assumed. There is still a well-defined interface where there is a sudden change from one effective index to the other, providing a boundary at which stronger resonant reflection takes place.

Like the isolated trimer, the triangular NGT has a plasmonic resonance. However, unlike the trimer, the resonance appears as two substantial absorption peaks P1 and P2 (shown in figure 4.10), which mark the edges of a transmission stop-band where the transmission through the waveguide is completely inhibited. Transmission stop-bands are seen in many periodic surface structures, including both photonic crystals [154] and plasmonic crystals [146, 155], and are well understood for the basic lattice structures such as the triangular lattice [156].

The integrated triangular NGT is driven by the evanescent field of the underlying waveguide mode (right panel of figure 4.11). To gain an insight into the

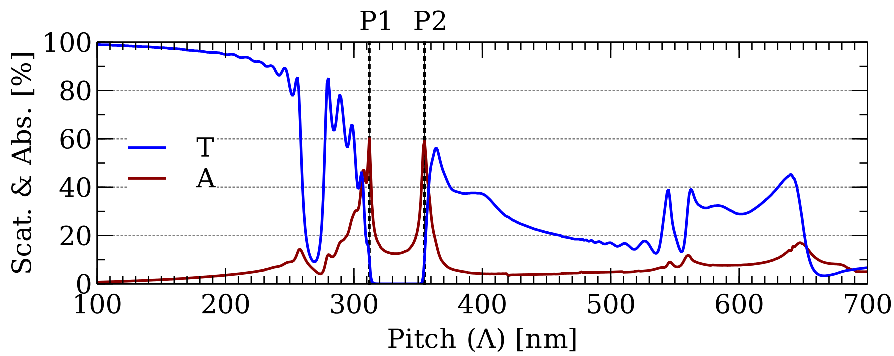

Figure 4.10: The transmission (T) and absorption (A) spectra for the integrated triangular NGT structure highlighting the plasmonic resonances P1 and P2 with dashed lines.

plasmonic resonance of the tiling and to explore the origin of the two absorption peaks, the surface structure can be illuminated under out-of-plane excitation (left panel of figure 4.11). This technique uses total internal reflection to produce an evanescent wave, which interacts with the surface structure in a similar way to the in-plane setup. The wavevector of the evanescent wave generated from the total internal reflection needs to match the wavevector of the in-plane waveguide mode to ensure the same plasmonic resonance is induced at the given frequency.

Since the wavevector of the surface plasmon polariton (SPP) of a metal-dielectric interface is below the light line of the dielectric medium, a plane wave impinging the dielectric is unable to directly couple to the SPP. Instead, a dielectric prism of a higher permittivity can be used to provide the larger wavevector needed. Removing the silica substrate and making the silicon waveguide semi-infinite allows the use of the silicon as the higher index prism. Since the light from the silicon substrate will have a larger wavevector than that of the SPP for the metal-silica interface, the wave is able to couple to the SPP when correctly phase matched.

The phase of the out-of-plane wave can be phase matched with the waveguide mode by altering the incident angle. The wavevector of the waveguide mode is

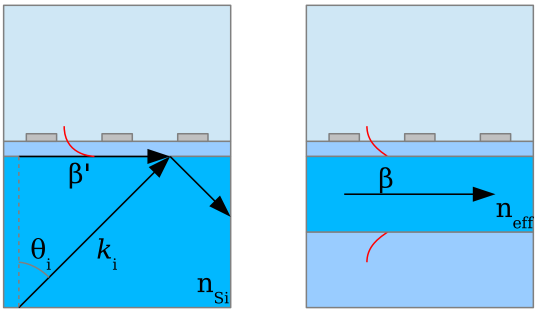

Figure 4.11: A comparison of an out-of-plane (left panel) and in-plane (right panel) illuminated surface structure highlighting the evanescent fields (red lines).

$\beta = n_{\text{eff}} k_0$, where n_{eff} is the effective index of the waveguide and $k_0 = 2\pi/\lambda_0$. For an external out-of-plane wave incident from a prism with refractive index n_{i}, under the Otto configuration [8] (see left panel of figure 4.11), the wavevector of the evanescent wave $\beta' = n_{\text{i}} k_0 \sin\theta_{\text{i}}$ is a projection of the incoming wave vector from the dielectric prism at the incident angle θ_{i} from the interface normal.

The incident angle required to match β' with β can be calculated by setting the equations equal to each other and rearranging, giving a ratio of the refractive and effective indices

$$\theta_{\text{i}} = \arcsin\left(\frac{n_{\text{eff}}}{n_{\text{i}}}\right). \tag{4.1}$$

An incident angle of $\theta_{\text{i}} = 54.8°$ is required to phase match the wavevector of the out-of-plane plane wave to that of the waveguide mode. Since this angle is larger than the critical angle of the silicon-silica interface ($\theta_c = 24.4°$), the wave will undergo total internal reflection on the silicon-silica interface, resulting in an evanescent wave with a propagation wavevector matching that of the waveguide mode of the integrated platform. To reduce the influence of the silicon layer upon the plasmonic resonance, a larger buffer layer thickness of 150 nm is used separating the plasmonic structure from the silicon.

The absorption spectra for out-of-plane illumination of the triangular NGT is depicted in figure 4.12. The absorption peak is a single broad LSPR resonance of the triangular NGT lattice centred around $\Lambda \approx 325$ nm. The plasmonic resonance is located between the two absorption peaks of the integrated struc-

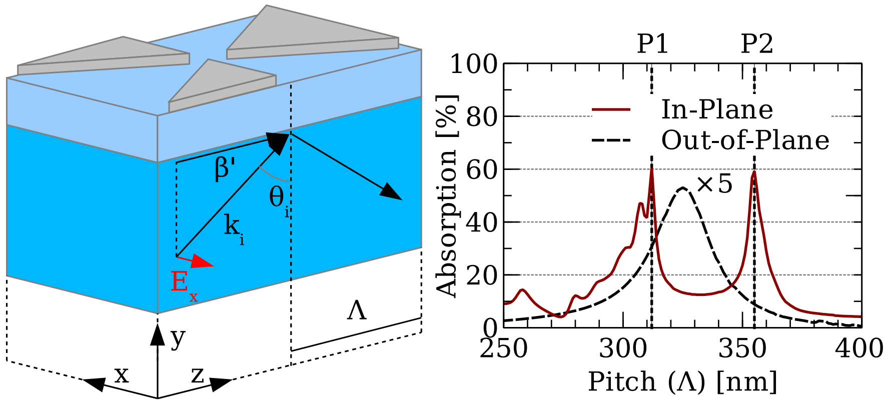

Figure 4.12: One unit cell of the integrated plasmonic triangular NGT (left), illuminated by an out-of-plane TE mode. A comparison of the absorption (A) spectrum (right) for the in-plane (solid) and out-of-plane (dashed) illumination.

ture under in-plane illumination. As a side effect of the increased buffer height, the interacting evanescent wave is exponentially weaker due to the increased distance to the plasmonic structure, resulting in a weaker resonance. However, the position of the resonance is closer to that of the pure metal-silica LSPR, as the influence of the silicon layer is reduced. A thinner buffer would bring the higher-indexed silicon closer to the plasmonic surface, reducing the wavelength of the LSPR and therefore resulting in a resonance shift towards shorter pitches.

It is clear that the presence of the waveguide in the integrated (in-plane) setup effects the plasmonic resonance. The LSPR resonance splits into two strong absorption peaks which mark the edges of a transmission stop-band. The presence of the waveguide provides an additional photonic mode to the system which hybridises with the SPP mode of the surface structure, forming a waveguide plasmon polariton.

Waveguide plasmon polaritons (WPPs) [157–161] arise from the coupling between a plasmon polariton, for example the LSPR of a nanoparticle, with a photonic mode [162], such as that of a nearby waveguide. The periodic structuring of the NGTs can manipulate the optical properties of the waveguide, similar to that of photonic crystals [159]. As the elements of the NGT are coupled in a dense array, the LSPRs strongly couple to a plasmonic band that supports the propagation of a SPP along a chain of the nanoparticles [163]. The coupling between this SPP propagation and the waveguide mode forms the quasi-particle waveguide plasmon polariton [157].

The strong coupling present in the integrated triangular NGT between the plasmonic and photonic modes allows for strong hybridisation, resulting in the two modes to anti-cross at the point where the wavevectors and frequencies match (described in figure 4.13).

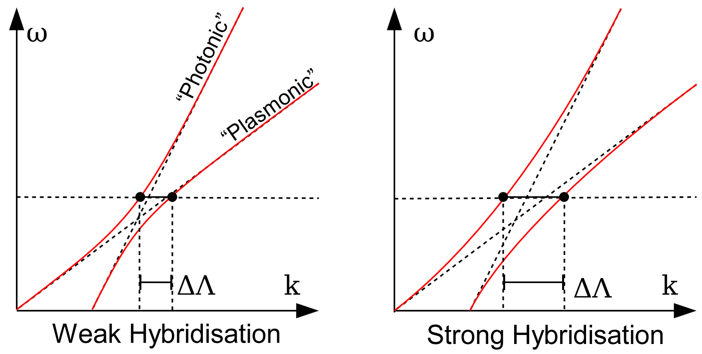

Figure 4.13: An illustration of a $\omega - k$ dispersion diagram for a structure with a photonic and plasmonic mode highlighting the effects of hybridisation strengths on the resonance position. Weak hybridisation may cause the resonance peaks to overlap resulting in the inability to distinguish the two resonances.

This hybridisation can be explored by varying the distance between the two structures via the thickness of the buffer layer. A thinner buffer layer will bring the two system closer together resulting in a higher overlap of the modal fields and therefore stronger coupling and hybridisation. This effect can be seen in figure 4.14.

Figure 4.14 shows that as the buffer thickness decreases, the hybridisation strengthens resulting in the separation of the absorption resonances. This anti-crossing behaviour of the hybridisation between a photonic waveguide mode and a plasmonic surface mode is well known [157]. The transmission stop-band between the two absorption peaks is a characteristic feature of metallic arrays where the plasmonic resonance prevents the propagation of energy [30, 140].

The sharp change in transmission at the edge of the stop-band is potentially a

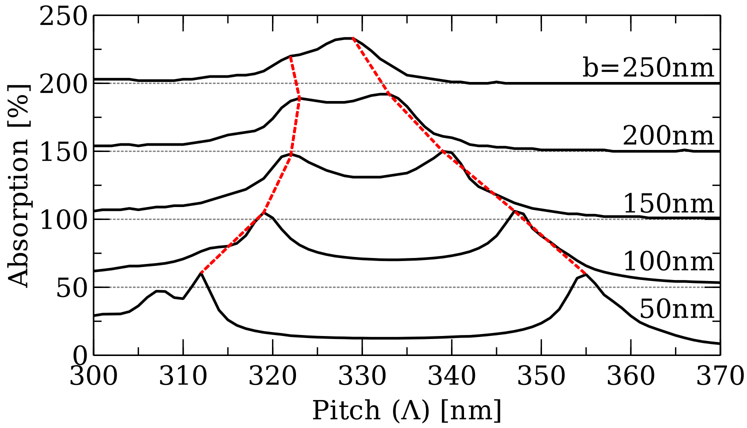

Figure 4.14: The absorption spectra for the integrated triangular NGT for a range of buffer heights (b) (denoted in the labels). The dashed red lines are estimations of the peak locations, showing an anti-crossing behaviour. Each individual spectra is shifted by an additional 50% absorption.

good candidate for sensing applications. Metallic nanoparticle arrays have been used for sensing purposes [61, 164] due to the collective high field strengths at the edges of the nanoparticles. Since the resonances of the nanoparticles are sensitive to changes in the dielectric environment in which they reside, a shift in the spectral features of the device can be expected. Sharp spectral features, such as at the edge of the transmission stop-band for the triangular NGT, can be used to detect a change in the dielectric environment at the surface as the spectral shift may be strong enough to allow the device to change from a non-transmitting state to a state of transmission.

The triangular NGT surface is exposed to air meaning it can be used to detect a liquid or gas which flows over the surface between the surface elements. Figure 4.15 shows the response of the triangular NGT when the material between the metallic elements is changed from having a refractive index of $n = 1.00$ (air) to an arbitrary medium of a higher refractive index, $n = 1.05$. The sharper feature at the end of the transmission stop-band (P2) will be used to detect the shift in the transmission caused by the change of dielectric environment.

To quantify the strength of the sensing ability of the NGT, a figure of merit

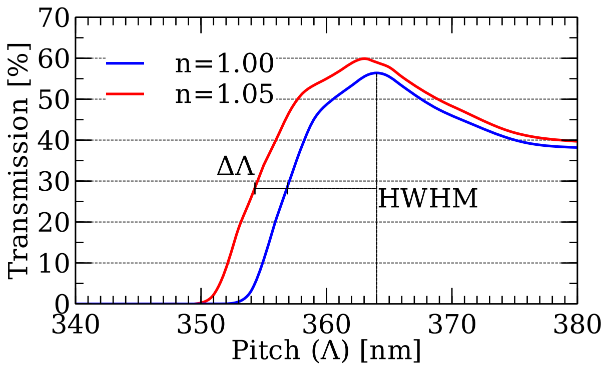

Figure 4.15: The shift of the P2 edge of the transmission stop-band when the surface is exposed to a $\Delta n = 0.05$ change in the dielectric environment.

(FOM) taking into account the peak size (the full-width half-maximum, which is twice the half-width half-maximum taken from figure 4.15), the shift in the resonance $\Delta\Lambda$ and the change in dielectric constant Δn. The ratio of the shift in the spectral peak (in nm) relative to the change in dielectric constant (in refractive index units, RIU) provides the sensitivity of the device. Taking the sensitivity against the peak's full-width half-maximum (also in nm) provides a quantity on the performance of the resonance structure [164]

$$FOM = \frac{\Delta\Lambda/\Delta n\,[\mathrm{nm}\,/\,\mathrm{RIU}]}{FWHM\,[\mathrm{nm}]}. \tag{4.2}$$

The FOM for the triangular NGT comes to $3.71\,\mathrm{RUI}^{-1}$. It is interesting that the triangular NGT shows this property despite not being specifically designed for this purpose. Other NGT structures could be designed to provide sharper spectral features and a stronger sensitivity to the dielectric environment.

In addition to the plasmonic resonance, the triangular NGT has an out-of-plane scattering regime at larger pitch lengths. This feature is due to the periodic structuring in the propagation direction, leading to the ability to provide additional momentum to the underlying waveguide mode and therefore coupling to radiative modes; similar to that of the grating. The triangle array has a greater influence the TE mode of the waveguide due to the strong interaction with the dipole mode of the triangular elements which do not exist in the case of the grating. The characteristic out-of-plane scattering dip, caused by the Bragg reflection when the pitch of the structure matches that of the wavelength of the waveguide mode, coincides with the out-of-plane scattering where $\theta_s = 0°$. Using this and equation 3.3, an estimation for the effective index of the nanogap tiling can be made (see section 3.2), and is found to be $n_{\text{eff}} = 2.82$. The $\theta_s = -90°$ scattering angle for both the superstrate ($n_s = 1.0$) and substrate ($n_s = 1.44$) scattering can now be estimated at 405.8 nm and 367.8 nm respectively, as marked on figure 4.16.

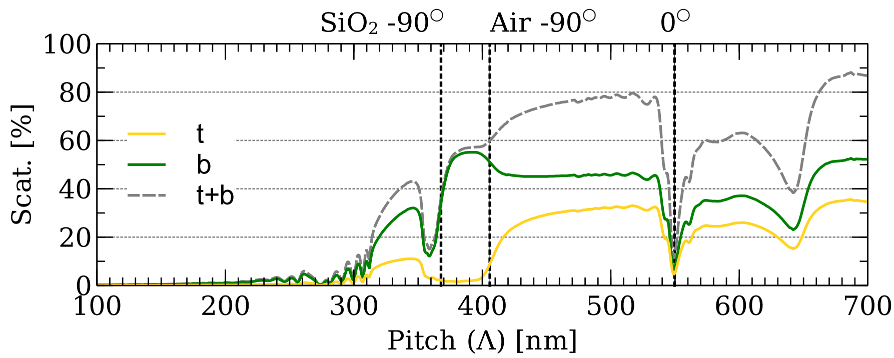

Figure 4.16: The top (t) and bottom (b) spectra for the integrated triangular NGT structure highlighting the out-of-plane coupling angles from equation 3.3 with dashed lines.

The $\theta_s = -90°$ scattering limits for both the superstrate and substrate match very well with the onset of out-of-plane scattering as seen in figure 4.16 for the NGT structure. The drop in the scattering to the substrate (green line) at the onset of the superstrate out-of-plane scattering (yellow line) can also be clearly seen, creating a shoulder in the substrate scattering spectrum.

The scattering spectra of the triangular NGT revealed photonic resonances in the form of Bragg reflections, an anti-crossing behaviour from the hybridised plasmonic resonance and out-of-plane scattering. The sharp transmission change at the edge of the plasmonic resonance is a good candidate for sensing the changes in the dielectric environment of the surface structure.

The triangular NGT has been studied in this section in the backwards orientation. This orientation was chosen due to potentially having a stronger focal spot field enhancement as the shape of the triangles results in a focusing of the evanescent field into the nanogaps, increasing the surface field enhancement. The triangular NGT in the forward orientation is explored in the following section.

4.3 Asymmetric Transmission

The triangular NGT has a geometric asymmetry along the waveguide propagation direction due to the triangular shape of the metallic elements. Exploring the integrated triangular NGT system with the triangles in the forward orientation, a difference in the scattering spectra is observed in comparison with the backwards orientated triangles around the second Bragg peak (B2), as shown in figure 4.17.

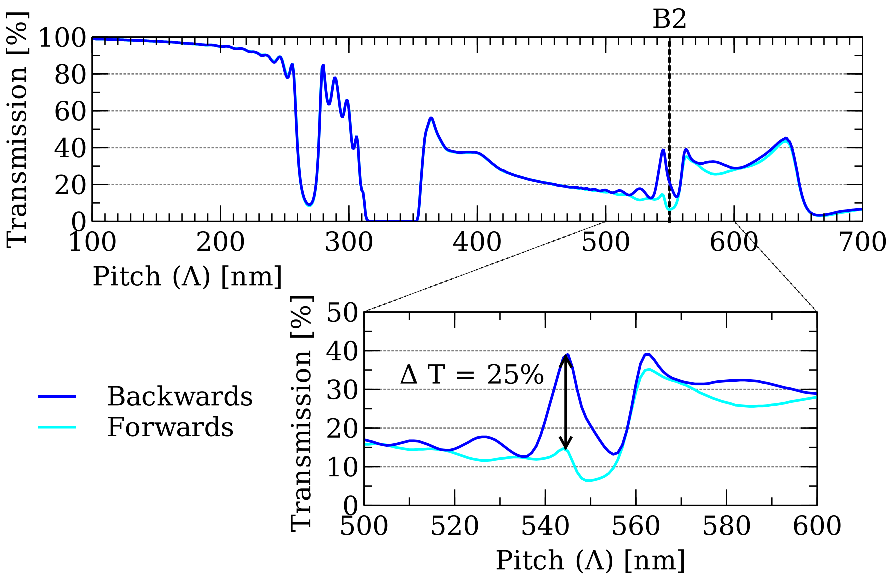

Figure 4.17: A comparison of the full (top) and expanded (bottom) transmission spectra for the integrated triangular NGT structure with $N = 25$ elements under forward and backward illumination highlighting the maximum transmission difference (ΔT).

The transmission spectra between the forward and backward triangle orientations are similar except in the region where the effective wavelength of the waveguide mode becomes resonant with the pitch of the system ($\Lambda \approx \lambda_{\text{eff}}$). A closer inspection of this region (bottom panel of figure 4.17) reveals a large transmission difference of around 25% at $\Lambda \approx 545\,\text{nm}$. Evidently, this transmission difference must come from asymmetry of the triangular elements [165].

The transmission measured is the total flux of energy across the end boundary of the system. The observed difference in transmitted energy between the two orientations should be apparent in the other scattering or loss channels (shown in figure 4.18).

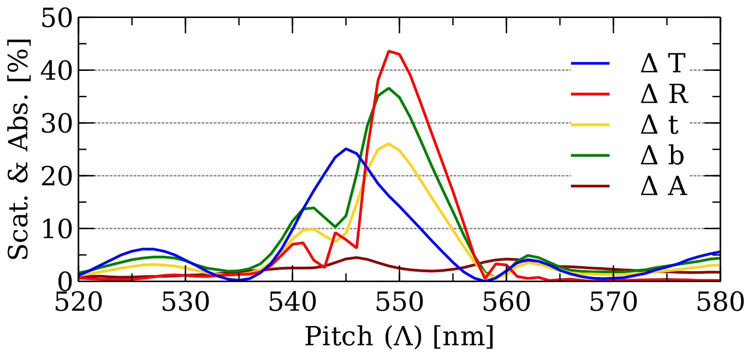

Figure 4.18: The absolute difference between the transmission (ΔT), reflection (ΔR), top (Δt) and bottom (Δb) scattering, and the absorption (ΔA) between the forward and backward orientated elements.

Looking at the difference in the scattered energy through all the domain boundaries between the forward and backward orientations (figure 4.18) shows that the largest difference in energy transfer is in the reflected and out-of-plane scattering channels. This suggests that, for the forward orientated triangles, the energy in the waveguide is scattered to a higher degree than in the backward orientation. For the backward orientated triangles the evanescent field of the waveguide mode interacts with the point of the triangle first and is gradually tapered into the nanogap, reducing the scattered energy. However, no gradual tapering occurs for the forward orientation because the evanescent field interacts with the base of the triangle first, resulting in higher scattered energy.

The energy flux through the various scattering channels does not itself provide a full description of the performance of the triangular NGT, especially for the structuring of the fields inside the device. At $\lambda_0 = 1550\,\mathrm{nm}$, the 220 nm silicon waveguide supports the fundamental TE and TM modes across its height. However, it can support higher order modes within the plane of the waveguide (i.e. the x-direction). For one unit cell width, an antisymmetric mode may exist. The x-component of the electric field of the fundamental mode and the first asymmetric mode for one unit cell width are depicted in figure 4.19.

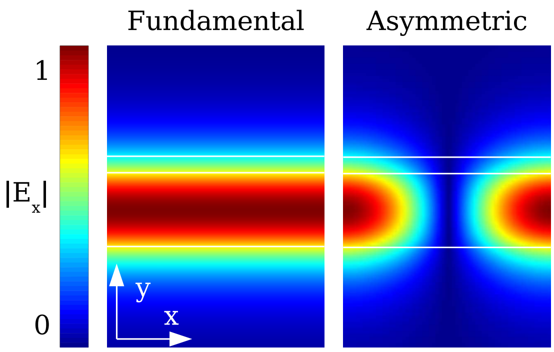

Figure 4.19: A comparison of the electric field $|E_x|$ of the fundamental and the first asymmetric TE waveguide modes for the open geometry.

As previously discussed, the triangular NGT is able to provide momentum to the waveguide mode due to its periodic structuring in the direction of wave propagation. This offers the potential to provide coupling between different waveguide modes. For example, mode conversion is known to occur in both photonic crystals [166] and waveguides [167, 168].

The E_x component of the electric fields for the triangular NGT consisting of 25 elements in length is displayed in figure 4.20 for the forward and backward orientations. The fundamental TE mode in injected into both structures. The electric fields are seen to undertake a mode transformation, in both orietnations, to the antisymmetric mode due to the structuring of the metallic surface (the width of the image is two unit-cells). There is a clear difference in the rate of the mode conversion between the two orientations as the fields are seen to have different structuring. To explore this mode conversion for both orientation in more detail, a four port scattering matrix of the device is determined.

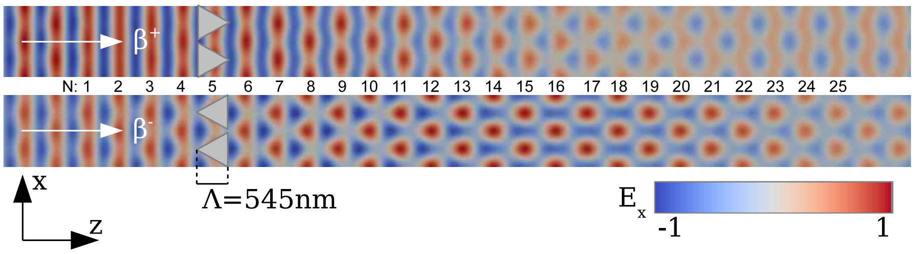

Figure 4.20: A comparison of the E_x fields for the forward (top) and backward (bottom) orientated triangles in the centre of the waveguide. The numbers indicate the approximate locations of the elements. The 5th element has been drawn to show the orientation.

The scattering matrix for a system consisting of 4 ports can be written

$$\begin{bmatrix} b_1 \\ b_2 \\ b_3 \\ b_4 \end{bmatrix} = \mathrm{S} \begin{bmatrix} a_1 \\ a_2 \\ a_3 \\ a_4 \end{bmatrix}, \ \mathrm{S} = \begin{bmatrix} \mathrm{S}_{11} & \mathrm{S}_{12} & \mathrm{S}_{13} & \mathrm{S}_{14} \\ \mathrm{S}_{21} & \mathrm{S}_{22} & \mathrm{S}_{23} & \mathrm{S}_{24} \\ \mathrm{S}_{31} & \mathrm{S}_{32} & \mathrm{S}_{33} & \mathrm{S}_{34} \\ \mathrm{S}_{41} & \mathrm{S}_{42} & \mathrm{S}_{43} & \mathrm{S}_{44} \end{bmatrix}, \tag{4.3}$$

where the scattering parameter S_{nm} is found by dividing the outgoing power flow through port n by the incident power flow on port m, $b_{\mathrm{n}}/a_{\mathrm{m}}$. Since these parameters are amplitudes, taking the modulus squared provides the energy transfer, $|\mathrm{S}_{\mathrm{nm}}|^2$.

Port boundaries, solved to the fundamental and first asymmetric modes at both ends of the structure (figure 4.21), are used to determine the mode-specific energy flux across the boundaries, and therefore provide the scattering parameters of the system.

The scattering parameters for the triangular NGT, with a pitch equal to the maximum transmission difference found in figure 4.18 ($\Lambda = 545\,\mathrm{nm}$), are shown in figure 4.22.

From the scattering parameters in the left panel of figure 4.22, it is clear

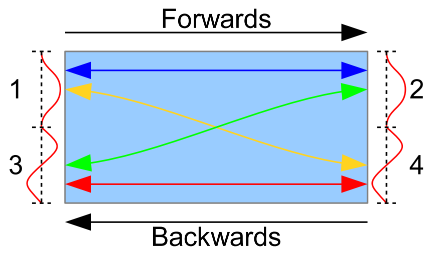

Figure 4.21: The 4-port boundary setup for the triangular NGT system. Ports 1 and 2 are solved for the fundamental mode, while ports 3 and 4 are solved for the first asymmetric mode. The coloured arrows through the device represent the transmissive scattering parameters between the ports in either direction.

that $S_{nm} = S_{mn}$. This is a signature of a symmetric scattering matrix and is expected for a linear and passive system. The triangular NGT continuously converts between the two modes. However, the rate of conversion is different for each mode and for each propagation direction, leading to a asymmetry mode conversion. With no surface elements, the injected mode is fully transmitted, as shown by the blue (S_{12} and S_{21}) and red (S_{34} and S_{43}) lines at $N = 0$. As the number of elements on the device increases, the structure starts to convert the waveguide modes. With only a few elements ($N \approx 16$) the injected mode is highly converted and back-conversion starts to dominate. The loss of the system becomes significant with many plasmonic elements, resulting in the sum of the scattering parameters being much less than unity.

The graphs on the right hand side of figure 4.22 show the proportion of each transmission mode relative to the total transmissive energy flux of the system. It is clear from these graphs that the backwards propagating fundamental mode gets nearly fully converted at around $N = 19$ elements. For comparison, the forward propagating mode at $N = 19$ only partially converts between the modes ($\sim 54\%$) before back-conversion begins to dominate.

Using this data it is possible to optimise the NGT structure depending on the required property. For example, if total conversion from the fundamental mode to the first asymmetric mode is wanted the backwards triangles with $N = 19$ elements can be used, as mentioned. If a maximum transmission difference is

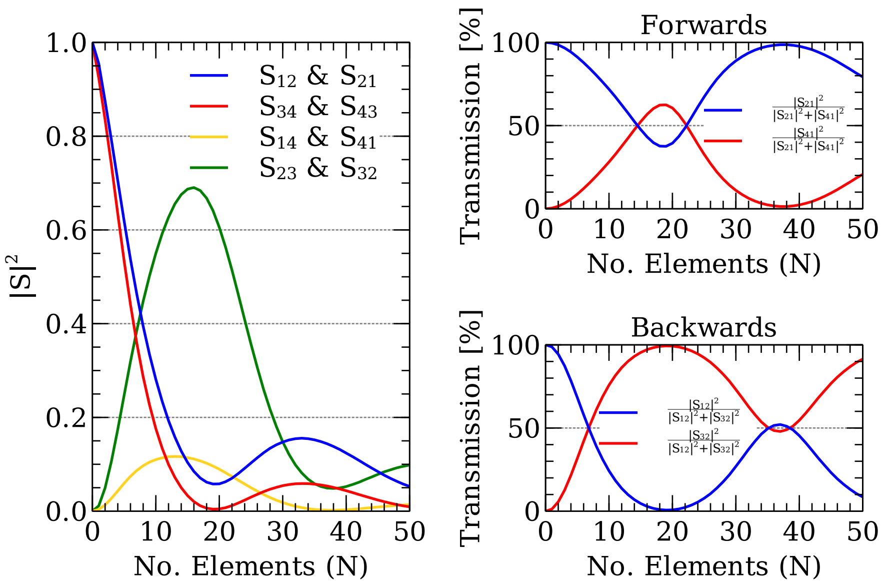

Figure 4.22: The scattering parameters (left) for the triangular NGT and the relative mode proportion of the transmission for the forward (top right) and backward (bottom right) orientated triangles.

desired, irrelevant of modal content, then the largest difference between the transmissive scattering parameters can be used. This occurs for the backwards propagating fundamental mode at $N = 16$ elements, where a large difference in transmission of $\sim 54\%$ is obtained (figure 4.23). This can be compared to the $\sim 25\%$ difference in transmission of the original $N = 25$ simulation (figure 4.17).

Considering the large difference in transmission between the forward and backward propagation directions, the device could be seen as a step towards an optical diode. With a given transmission threshold, the device would exceed the threshold in the higher transmission direction (defined as passed) but be below the threshold in the lower transmission direction (defined as blocked).

With the emergence of silicon nanophotonics, research into optical diodes and isolators is being heavily pursued with the aim of fabricating an on-chip optical isolator being highly sought after. The current leading methods involve active breaking of time-reversal [169] techniques such as magnetic [170, 171]

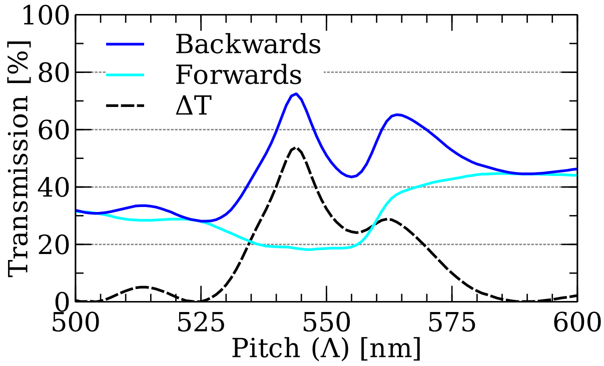

Figure 4.23: Optimised maximum difference in transmission (ΔT) for the triangular NGT with $N = 16$ elements.

or electric modulation [172, 173]. However, these techniques are often bulky or involve external devices or fields which may interferer with nearby devices. There have also been many attempts to realise passive silicon diodes and isolators based on photonic crystals [174–177], modulated refractive index waveguides [178–180] and ring resonators [168, 181]. However, it is very important to understand the definition of an optical isolator [182, 183]. Optical isolators must have asymmetry for *all* modes traversing the device, not just for a particular ensemble of modes, and therefore must have an asymmetric scattering matrix.

The integrated triangular NGT device does not include the use of active components and is completely linear, as seen by the symmetric scattering matrix (figure 4.22). The device cannot break Lorentz reciprocity in its current form and therefore cannot be used as an optical isolator, despite showing asymmetric mode conversion [184]. However, since the metallic structure is accessible from the surface, it can easily be combined with active components, such as electrical contacts, or with nonlinear materials [185, 186] in order to break Lorentz reciprocity. Silicon is known to have nonlinear properties [187], but the platform could equally be made out of other material systems (e.g. group III-V semiconductors) which have a wider availability of nonlinear materials.

The integrated triangular NGT has asymmetric transmission around the second Bragg peak due to the differing conversions of the TE modes from the triangle orientation. This effect was optimised to find a setup of complete modal conversion and another setup for a maximum difference in transmission of $\sim$ 54%, which, in conjunction with active or nonlinear components, may pave the way for an integrated on-chip optical isolator.

Some nonlinear materials are sensitive to the strength of the electric fields within them. If such a nonlinear material could be deposited between the surface elements of the NGT, the nonlinear material would benefit from the strong fields in the nanogaps. In the next section, the effective surface enhancement of the evanescent fields, caused by the surface triangular NGT, is explored in order to boost a nonlinear response.

4.4 Effective Surface Field Enhancement

Nanoplasmonic surfaces are increasingly being explored for their abilities to concentrate light into hot-spots, providing a large enhancement to the strength of the electromagnetic fields. High field strengths are useful for applications such as nonlinear optics [188] (for example, the Kerr effect in silicon [187]) and sensing [41] due to their increased interaction with stronger fields. The integrated NGTs not only offer the ability to use a wide range of nonlinear materials, due to the flexibility with the choice of material systems they can be made from, but they also provide an accessible surface in an integrated, on-chip design. As NGTs feature dense arrays of nanoparticles the high density of nanogaps can potentially provide a strong surface field enhancement (figure 4.24), for use in such applications.

To obtain the effective surface field enhancement provided by the structure, the strength of the electric field at the surface and in the waveguide are compared. The surface field strength, taken at the mid point of the metallic layer y_{s}, and the waveguide field strength, taken at the centre of the waveguide y_{wg}, are normalise by dividing by the averaged electric field strength of the open platform (i.e. without any surface structure) $\mathrm{E}^0(y)$, which is invariant in the

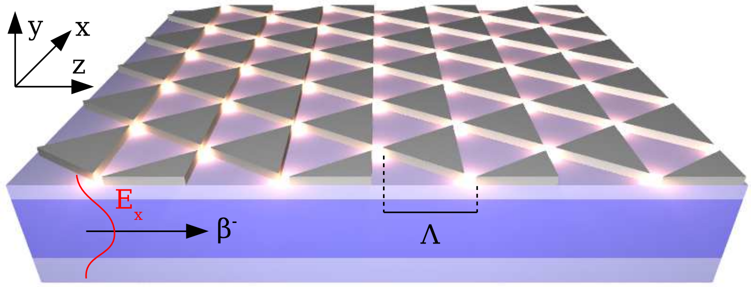

Figure 4.24: A graphical interpretation of the hot-spots for the integrated plasmonic triangular NGT, illuminated by the in-plane fundamental TE mode.

x and z directions. This yields the normalised electric field intensities at the surface ($y = y_\mathrm{s}$) and the mid-point of the waveguide ($y = y_\mathrm{wg}$)

$$\mathbf{E}_\mathrm{s}^2 = \frac{|\mathrm{E}(x, y_\mathrm{s}, z)|^2}{|\mathrm{E}^0(y_\mathrm{s})|^2} \tag{4.4a}$$

$$\mathbf{E}_\mathrm{wg}^2 = \frac{|\mathrm{E}(x, y_\mathrm{wg}, z)|^2}{|\mathrm{E}^0(y_\mathrm{wg})|^2}. \tag{4.4b}$$

These normalised electric field intensities (laterally averaged across the x-direction) are plotted in figure 4.25 to display how the field evolves as it propagates through the structure. The x-axis of the colour plots displays the structure length normalised against the pitch (i.e. the element number, as $N = z/\Lambda$). The average normalised intensities along the length of the structure in the propagation direction are displayed in the right hand panels.

The transmission stop-band of the SPP resonance can be clearly seen in figure 4.25 as a dark band in both the surface and waveguide fields (at $\Lambda \approx 325\,\mathrm{nm}$). The energy in the waveguide (bottom panel) is seen to diminish before the surface energy (top panel), suggesting the transition of energy from the photonic waveguide to the plasmonic structure. Additional transmission stop-bands can be seen at the locations of the Bragg reflections ($\Lambda_{\mathrm{B}1} \approx 275\,\mathrm{nm}$ and $\Lambda_{\mathrm{B}2} \approx 550\,\mathrm{nm}$). The apparent vertically striped nature of the surface field is due to the higher field intensities of the hot-spots formed in the nanogaps of the triangular elements.

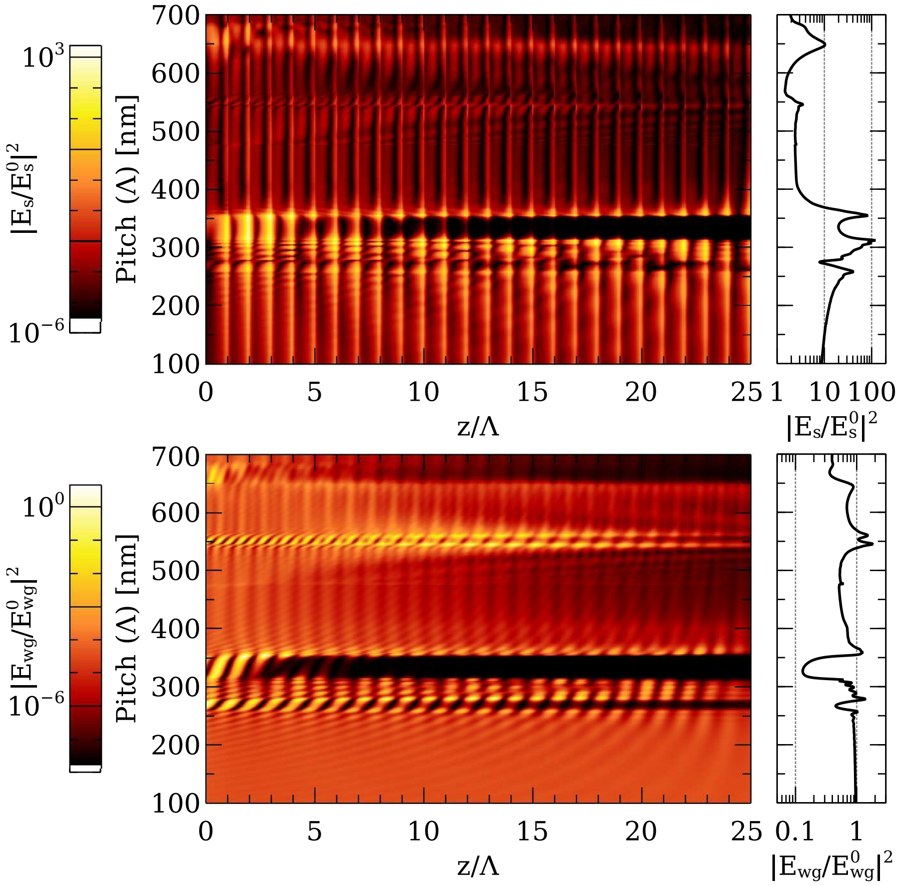

Figure 4.25: The laterally averaged normalised electric field intensities for the triangular NGT at y_s (top panels) and y_{wg} (bottom panels) along the propagation direction (left panels) and averaged along the propagation direction (right panels).

In order to quantify the potential to functionalise the triangular NGT surface, the effective enhancement of the linear and nonlinear susceptibilities of a material deposited onto the surface needs to be determined. To find the effective surface enhancement of the triangular NGT, the normalised surface field is taken relative to the normalised waveguide field. This has the added benefit of accounting for wave propagation effects, such as propagation attenuation, back reflection and standing wave formation. For example, the effective surface intensity enhancement $\eta_{\text{eff}}^{(\text{I})}$ for a χ^2 susceptibility is defined

$$\eta_{\text{eff}}^{(\text{I})} = \frac{\mathbf{E}_{\text{s}}^2}{\mathbf{E}_{\text{wg}}^2}. \tag{4.5}$$

The overall loss of the system due to scattering and absorption can be expressed in terms of the attenuation coefficient $\alpha = -\ln(\text{T})/(N\Lambda)$, where T is the transmission of the device and N is the number of elements of pitch length Λ. A more useful quantity is the propagation length of the fields within the device $\ell_{\text{P}} = 1/\alpha$.

The effective surface field enhancement and propagation length of the integrated triangular NGT are shown in figure 4.26.

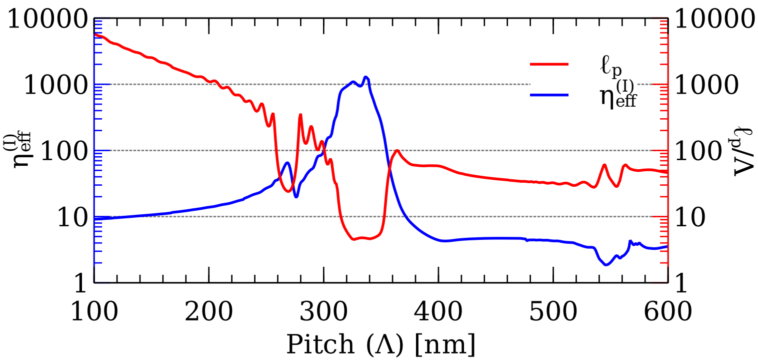

Figure 4.26: The effective surface intensity enhancement $\eta_{\text{eff}}^{(\text{I})}$ (blue) and propagation length normalised by the pitch ℓ_{p}/Λ (red) of the integrated triangular NGT structure.

From these results it is clear that the effective surface enhancement peaks at the plasmon resonance ($\Lambda \approx 325\,\text{nm}$) due to the LSPR of the surface structure in comparison to the energy of the waveguide mode. However, in this region of highly enhanced fields, the propagation length of the structure is greatly reduced, as the excited plasmonic modes are lossy. A high enhancement can also be seen at the first Bragg peak, but here the high attenuation is due to the back reflection of the energy. The propagation length of the device increases as the element sizes reduce into the subwavelength region ($\Lambda \lesssim 250\,\text{nm}$), yet the effective enhancement of the surface levels out to a value of ~ 10. This off-resonant enhancement can be attributed to the lightning rod effect [36] which concentrates the energy of the fields to the edges of the elements without inducing high plasmonic losses. The effective enhancement of the out-of-plane scattering regime ($\Lambda > 400\,\mathrm{nm}$) is much lower than that of the subwavelength regime due to the onset of out-of-plane scattering, reducing the overall energy available in the system.

This effective surface field enhancement is a good measure of how much of the electric field concentrates at the surface relative to the waveguide. Although the achieved intensity enhancement of the subwavelength regime is comparatively low, the photonic waveguide mode remains in interaction with the nanogap tiling along the length of the structure due to the low loss and low scattering. To quantify the trade off between the surface enhancement and the propagation loss, a figure of merit value is introduced which can be thought of as an effective cross section of the device

$$\sigma_{\mathrm{eff}} = \eta_{\mathrm{eff}}^{(\mathrm{I})} \ell_{\mathrm{p}} \Lambda. \tag{4.6}$$

This cross section (specifically for second order nonlinearities) combines the effective surface enhancement and propagation length to produce a description of the performance of the device. A high surface enhancement and a long propagation length are both beneficial for the performance of the structure, and will both increase the cross section value. Using this, the effective cross section for the triangular NGT is shown in figure 4.27.

The effective cross section is near constant in both the subwavelength and radiative regimes, where the ability of the NGT to concentrate the energy on the surface of the structure can be seen to be proportional to the density of hot-spots ($\sim 1/\Lambda^2$) and the normalised attenuation ($(\ell_{\mathrm{p}}/\Lambda)^{-1}$)

$$\eta_{\mathrm{eff}}^{(\mathrm{I})} = const. \times \frac{1}{\Lambda^2} \left(\frac{\ell_{\mathrm{p}}}{\Lambda} \right)^{-1}. \tag{4.7}$$

As an example application of the device, an active gain material is used in conjunction with the SOI platform [47]. To take advantage of the concentrated

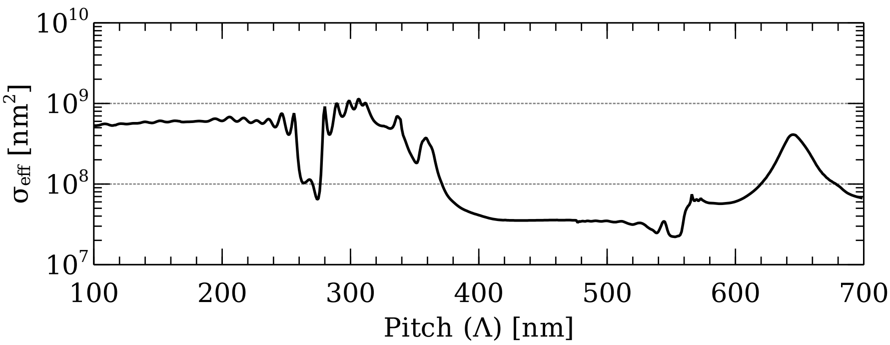

Figure 4.27: The effective cross section σ_{eff} of the triangular NGT, showing the near constant subwavelength and radiative regimes.

electric field of the NGT, the gain medium is assumed to deposited onto the surface between the metallic elements, and of the same thickness as the metal (30 nm). The confinement factor of the gain medium layer can be calculated by integrating the proportion of the evanescent field of the electric field intensity in the gain medium layer and dividing it by the total integrated field, for the open geometry, as described by the equation

$$\Gamma = \frac{\int_{-\infty}^{+\infty} \Theta(y) \left|\mathbf{E}^0(y)\right|^2 \mathrm{d}y}{\int_{-\infty}^{+\infty} \left|\mathbf{E}^0(y)\right|^2 \mathrm{d}y}, \tag{4.8}$$

where $\Theta(y)$ is unity for the gain-filled layer, and zero elsewhere (see figure 4.28). For the given device, the confinement factor is found to be $\Gamma \approx 0.0143$.

To fully compensate the dissipative and radiative losses within the system, an equivalent gain g_{equiv} from the material would be required. The equivalent gain required to fully compensate the total losses of the system can be written as

$$g_{\mathrm{equiv}} = \frac{1}{\eta_{\mathrm{eff}}^{(\mathrm{I})} \ell_{\mathrm{p}} \Gamma}. \tag{4.9}$$

The equivalent gain for the integrated triangular NGT device is shown in figure 4.29.

The subwavelength regime of the device shows a realistically low equivalent gain needed to fully compensate the losses. This is due to the high surface

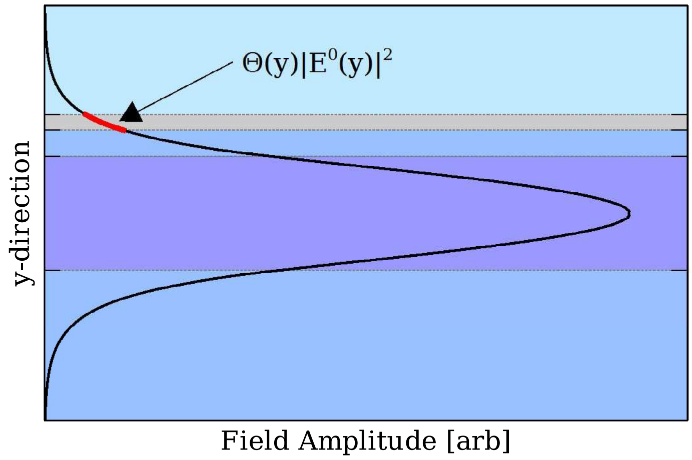

Figure 4.28: An illustration of the proportion (red) of the evanescent tail of the TE waveguide mode in the gain-filled medium.

field enhancement of the triangular NGT and low losses within this region. At the first Bragg peak ($\Lambda \sim 260\,\mathrm{nm}$), the equivalent gain required to compensate the loss is higher due to the onset of resonant back reflection, reducing the available energy which can interact with the gain. At the plasmonic resonance ($\Lambda \sim 340\,\mathrm{nm}$), the equivalent gain required is surprisingly low despite the high losses induced. However, this is also where the surface field concentration is at its strongest between the plasmonic elements, increasing the effectiveness of the gain medium. Beyond the plasmonic resonance out-of-plane scattering dominates, resulting in a high equivalent gain value of $\sim 10^4\,\mathrm{cm}^{-1}$ necessary to compensate for the increased losses.

The triangular NGT structure is found to deliver a high surface field enhancement in conjunction with relatively low losses for the subwavelength regime. A surface-deposited gain material with realistically achievable effective gain could be used to compensate for the losses of the device. The strong surface field enhancement of the NGT could also be used to enhance the nonlinear response of a nonlinear material when deposited on the surface.

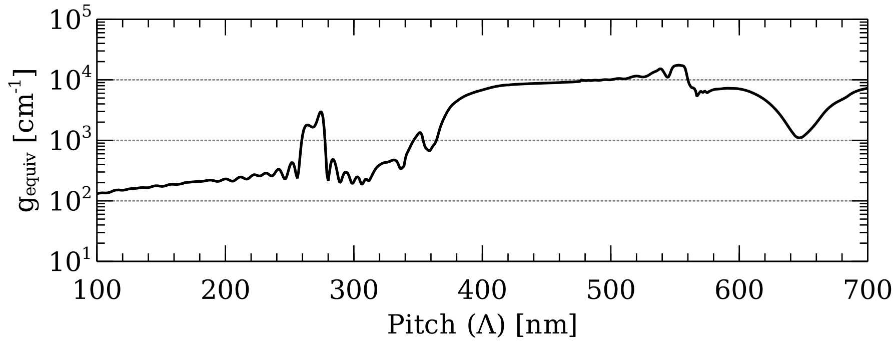

Figure 4.29: The equivalent gain required to compensate the losses of the integrated triangular NGT as calculated from equation 4.9.

Chapter 5

Summary and Outlook

The aim of the project, guided by the increasing interest in plasmonic surfaces, was to integrate plasmonic surface structures to a photonic waveguide platform to address the issue of high losses associated with plasmonic structures. A silicon-on-insulator waveguide platform based on existing CMOS technology was modelled, employing a transverse electric (TE) mode which was observed to have lower losses in comparison to the transverse magnetic mode when in the proximity of a metallic cover. The TE mode provided a better impedance match between the open (uncovered) and closed (metal covered) waveguide systems. The evanescent field of the waveguide mode is in interaction with the plasmonic structure along the entirety of its length. A buffer layer of tunable thickness is introduced between the waveguide and plasmonic surface to provide a way to tune the coupling strength between the waveguide mode and the plasmonic surface structure, and therefore the associated losses.

A coupling mechanism between radiation modes and the waveguide was introduced in the form of a metallic surface grating. The geometry of the grating was optimised to provide high coupling efficiencies between the waveguide and radiation modes, allowing for an experimentally convenient way to couple external fields to the waveguide. This allows for the excitation of waveguide modes within the platform which may then be used to interact with surface structures.

A particular class of surface structures, nanogap tilings (NGTs) was introduced. NGTs, as the name suggests, are regular tiling patterns of metallic patches consisting of nanogaps between the elements where light can be focused into hot-spots and the fields enhanced. One particular tiling pattern, the fixed triangular patches arranged on a triangular lattice, was explored in detail. Due to the triangular shape of the elements, the light propagating towards the point of the triangles is efficiently tapered into the nanogaps, increasing the field strength. The triangular NGT is an effective surface field enhancer because all nanogaps are in the direction of the electric field, allowing for complete hot-spot illumination. In comparison, for example, diamond patches in a square lattice only has half the nanogaps orientated along the electric field, resulting in the illumination of only half the nanogaps and therefore reducing the density of hot-spots. The triangular NGT provided insight to a variety of different effects simply by scaling the surface structure in relation to the effective wavelength of the waveguide mode. From this, multiple regions of operation were identified, each with interesting potential prospects.

Due to the strong periodic nature of the NGT in the direction of wave propagation, the lattice provides phase matching of the propagating mode to radiative modes, including resonant backscattering into the waveguide (Bragg reflections) and out-of-plane scattering to the substrate and superstrate. These features are described by the k-matching equation. Bragg reflection occurs when the pitch matches every half-wavelength of the effective waveguide mode, while the out-of-plane resonance is a broad region around the second Bragg peak, where the effective wavelength of the waveguide mode is in near resonance with the pitch of the surface structure.

When the wavevector of the photonic mode matches the plasmonic resonance of the surface structure (which is relative to the size of its elements), a hybrid mode is formed. This waveguide plasmon polariton takes the form of two strong absorption resonances which mark the edges of a transmission stop band, where transmission of the waveguide mode is completely inhibited. The NGT surface was additionally explored with an out-of-plane wave at angle of incidence that matched the evanescent field of the totally internally reflected mode with the propagation constant of the waveguide. This revealed the unhybridised plasmonic resonance, whose location was between the two absorption resonances found via in-plane illumination. The sharp change in transmission at the edge of the transmission stop-band offers the opportunity to use the NGT for sensing purposes. A change in the dielectric environment around the accessible surface structure could cause the spectrum resonance to shift, allowing the NGT to detectably change from a non-transmitting state to a transmitting state.

The triangular NGT has C_{3v} symmetry meaning it has two major axes of excitation: the forward (with the point of the triangular element) and backward (against the point of the element) propagation directions. The scattering spectrum between the two propagation directions significantly differ when the element size is near-resonant to the effective wavelength of the guided mode. Around this location, the surface structure allows the excitation of a higher order waveguide mode. As the geometry of the surface structure is asymmetric between the two propagation direction, the rate of conversion between the waveguide modes differ. Since the two modes have different attenuations and scattering, the overall transmission through the device varies between the two propagation direction. With optimised structures, a large difference in transmission of 54% and a 100% mode conversion is achieved. The asymmetric transmission and mode conversion may provide a step towards an on-chip optical isolator when the symmetry of the scattering matrix is broken via the inclusion of active or nonlinear materials.

The NGT structure has the ability to concentrate light at the surface of the device in a dense array of hot-spots in the nanogaps between the metallic elements. Despite being only evanescently driven by the underlying waveguide, the concentration of the surface field exceeds the strength of the field in the waveguide. To quantify the ability of the surface structure to enhance the surface fields, a novel field enhancement extraction technique was defined. The normalised fields of the surface structure is taken relative to the normalised field of the waveguide centre to provide an effective surface enhancement. The effective surface enhancement was found to be high for the subwavelength regime, peaking at the plasmonic resonance, and then lower for the out-of-plane scattering regime.

To provide an improved description of the ability of the surface structure to concentrate the fields at the surface, an effective cross section was introduced, taking into account the trade off with the attenuation of the system. This cross section was found to be near constant in the subwavelength and scattering regimes which suggests that the energy on the surface device is proportional to the density of hot-spots and the attenuation of the system. The subwavelength regime appears high in performance due to the high off-resonant field concentration between the elements in addition to low attenuation, marking it as an ideal candidate for surface functionalisation with nonlinear and gain materials.

With the trade-off between light concentration and losses characterised, an application of the surface structure with a theoretical gain material is explored. The effective gain required to fully compensate the losses of the system, with a gain material deposited on the surface between the metallic elements, was found to be realistically possible for the subwavelength regime and even at the plasmonic resonance, although higher gain values are required to compensate the onset of the out-of-plane scattering at longer pitch lengths.

The dielectric platform designed in this work is not limited to the SOI material system and telecommunication wavelengths. Any material system with a high refractive index contrast, such as group III-V semiconductors (e.g. InGaAsP) for 510 nm wavelengths, may be used to form the photonic waveguide platform. The use of III-V semiconductors would offer a wider possibility of using nonlinear or active materials, as well as the use of quantum-wells and dots, opening up the surface structures and this integrated platform to a wide range of useful applications.

The flexibility of nanolithography allows for the deposition of virtually any

2D structure onto the surface of the photonic platform, potentially even graphene [189]. More complex structures, such as plasmonic guides [45, 47] and circuitry [190] may also be applicable. The triangular NGT tiling explored in this work is only one of many possibilities of covering the surface with regular 2D tilings. For example, a graphene-like plasmonic crystal array [191, 192] could provide interesting effects [193, 194] due to the Dirac Point known to exist for such structures [195, 196]. The potential for other NGT structures, or indeed any other planar surface structure or antenna, opens up the possibility of a wealth of designer surfaces on the integrated platform dedicated to specific tasks. This allows for multiple hybrid or on-chip devices such as sensors, plasmonic couplers, active surface emitters, switches and all-optical modulators.

With the growing field of metamaterials, the inclusion of a metasurface on to the platform is desirable. For example, subwavelength split ring resonators (SRRs) would suit the TE polarised mode of the integrated platform due to both the electric field being across the gap of the SRR and the out-of-plane magnetic field through the loop of the ring [197].

With the surface structure being exposed, the surface mounted metallic elements are accessible to electrical connections, allowing for the use of the surface structure for optoelectronic devices [198] or even plasmonic circuits [190], providing an alternate means to control the propagation of the light in the waveguide via the use of electronic signals and components, or the inverse situation of controlling the electrical output of a device with the guided light.

Bibliography

[1] P. M. Z. Davies, J. M. Hamm, Y. Sonnefraud, S. A. Maier, and O. Hess, “Plasmonic nanogap tilings: light-concentrating surfaces for low-loss photonic integration.” ACS nano **7**, 7093 (2013).

[2] D. K. Gramotnev and S. I. Bozhevolnyi, “Plasmonics beyond the diffraction limit,” Nature Photonics **4**, 83 (2010).

[3] R. W. Wood, “On a Remarkable Case of Uneven Distribution of Light in a Diffraction Grating Spectrum,” Proceedings of the Physical Society of London **18**, 269 (1902).

[4] L. Rayleigh, “On the Dynamical Theory of Gratings,” Proceedings of the Royal Society A: Mathematical, Physical and Engineering Sciences **79**, 399 (1907).

[5] R. Ritchie, “Plasma Losses by Fast Electrons in Thin Films,” Physical Review **106**, 874 (1957).

[6] H. Duan, A. I. Fernández-Domínguez, M. Bosman, S. A. Maier, and J. K. W. Yang, “Nanoplasmonics: classical down to the nanometer scale.” Nano letters **12**, 1683 (2012).

[7] W. L. Barnes, A. Dereux, and T. W. Ebbesen, “Surface plasmon subwavelength optics.” Nature **424**, 824 (2003).

[8] A. V. Zayats, I. I. Smolyaninov, and A. A. Maradudin, “Nano-optics of surface plasmon polaritons,” Physics Reports **408**, 131 (2005).

[9] L. Novotny and N. van Hulst, "Antennas for light," Nature Photonics **5**, 83 (2011).

[10] V. Giannini, A. I. Fernández-Domínguez, S. C. Heck, and S. A. Maier, "Plasmonic nanoantennas: fundamentals and their use in controlling the radiative properties of nanoemitters." Chemical reviews **111**, 3888 (2011).

[11] K. L. Kelly, E. Coronado, L. L. Zhao, and G. C. Schatz, "The Optical Properties of Metal Nanoparticles: The Influence of Size, Shape, and Dielectric Environment," The Journal of Physical Chemistry B **107**, 668 (2003).

[12] D. Dregely, R. Taubert, J. Dorfmüller, R. Vogelgesang, K. Kern, and H. Giessen, "3D optical Yagi-Uda nanoantenna array." Nature communications **2**, 267 (2011).

[13] J. Homola, "Present and future of surface plasmon resonance biosensors." Analytical and bioanalytical chemistry **377**, 528 (2003).

[14] J. Anker, W. Hall, O. Lyandres, N. Shah, J. Zhao, and R. P. Van Duyne, "Biosensing with plasmonic nanosensors," Nature Materials **7**, 442 (2008).

[15] S. A. Maier, M. L. Brongersma, P. G. Kik, S. Meltzer, A. A. G. Requicha, and H. A. Atwater, "Plasmonics-A Route to Nanoscale Optical Devices," Advanced Materials **13**, 1501 (2001).

[16] J. Henzie, J. Lee, M. H. Lee, W. Hasan, and T. W. Odom, "Nanofabrication of plasmonic structures." Annual review of physical chemistry **60**, 147 (2009).

[17] N. A. Issa and R. Guckenberger, "Optical Nanofocusing on Tapered Metallic Waveguides," Plasmonics **2**, 31 (2006).

[18] E. Moreno, S. Rodrigo, S. Bozhevolnyi, L. Martín-Moreno, and F. García-Vidal, "Guiding and Focusing of Electromagnetic Fields with Wedge Plasmon Polaritons," Physical Review Letters **100**, 023901 (2008).

[19] M. Stockman, "Nanofocusing of Optical Energy in Tapered Plasmonic Waveguides," Physical Review Letters **93**, 137404 (2004).

[20] B. Hecht, H. Bielefeldt, L. Novotny, Y. Inouye, and D. Pohl, "Local Excitation, Scattering, and Interference of Surface Plasmons," Physical Review Letters **77**, 1889 (1996).

[21] S. I. Bozhevolnyi, V. S. Volkov, A. Boltasseva, and K. Leosson, "Local excitation of surface plasmon polaritons in random surface nanostructures," Optics Communications **223**, 25 (2003).

[22] J. Joannopoulos, S. Johnson, J. Winn, and R. Meade, *Photonic crystals: molding the flow of light*, 2nd ed. (Princeton Univ Pr, 2011).

[23] J. B. Pendry, A. Aubry, D. R. Smith, and S. A. Maier, "Transformation optics and subwavelength control of light." Science (New York, N.Y.) **337**, 549 (2012).

[24] V. M. Shalaev, "Optical negative-index metamaterials," Nature Photonics **1**, 41 (2007).

[25] R. Liu, T. Cui, D. Huang, B. Zhao, and D. Smith, "Description and explanation of electromagnetic behaviors in artificial metamaterials based on effective medium theory," Physical Review E **76**, 026606 (2007).

[26] J. B. Pendry, "Negative Refraction Makes a Perfect Lens," Physical Review Letters **85**, 3966 (2000).

[27] P. A. Huidobro, M. L. Nesterov, L. Martín-Moreno, and F. J. García-Vidal, "Transformation optics for plasmonics." Nano letters **10**, 1985 (2010).

[28] Y. Liu, T. Zentgraf, G. Bartal, and X. Zhang, "Transformational plasmon optics." Nano letters **10**, 1991 (2010).

[29] K. L. Tsakmakidis, A. D. Boardman, and O. Hess, "'Trapped rainbow' storage of light in metamaterials." Nature **450**, 397 (2007).

[30] C. L. Holloway, E. F. Kuester, J. A. Gordon, J. O'Hara, J. Booth, and D. R. Smith, "An Overview of the Theory and Applications of Metasurfaces: The Two-Dimensional Equivalents of Metamaterials," IEEE Antennas and Propagation Magazine **54**, 10 (2012).

[31] A. V. Kildishev, A. Boltasseva, and V. M. Shalaev, "Planar photonics with metasurfaces." Science (New York, N.Y.) **339**, 1232009 (2013).

[32] T. Ebbesen, H. Lezec, H. Ghaemi, T. Thio, and P. Wolff, "Extraordinary optical transmission through sub-wavelength hole arrays," Nature **391**, 667 (1998).

[33] E. C. Kinzel and X. Xu, "Extraordinary infrared transmission through a periodic bowtie aperture array." Optics letters **35**, 992 (2010).

[34] Q. Chen and D. R. S. Cumming, "High transmission and low color cross-talk plasmonic color filters using triangular-lattice hole arrays in aluminum films." Optics express **18**, 14056 (2010).

[35] K. Kumar, H. Duan, R. S. Hegde, S. C. W. Koh, J. N. Wei, and J. K. W. Yang, "Printing colour at the optical diffraction limit." Nature nanotechnology **7**, 557 (2012).

[36] J. Gersten and A. Nitzan, "Electromagnetic theory of enhanced Raman scattering by molecules adsorbed on rough surfaces," The Journal of Chemical Physics **73**, 3023 (1980).

[37] E. Fort and S. Grésillon, "Surface enhanced fluorescence," Journal of Physics D: Applied Physics **41**, 013001 (2008).

[38] A. Kinkhabwala, Z. Yu, S. Fan, Y. Avlasevich, K. Müllen, and W. E. Moerner, "Large single-molecule fluorescence enhancements produced by a bowtie nanoantenna," Nature Photonics **3**, 654 (2009).

[39] N. Liu, M. L. Tang, M. Hentschel, H. Giessen, and A. P. Alivisatos, "Nanoantenna-enhanced gas sensing in a single tailored nanofocus." Nature materials **10**, 631 (2011).

[40] S. Zou and G. C. Schatz, "Silver nanoparticle array structures that produce giant enhancements in electromagnetic fields," Chemical Physics Letters **403**, 62 (2005).

[41] V. G. Kravets, F. Schedin, a. V. Kabashin, and A. N. Grigorenko, "Sensitivity of collective plasmon modes of gold nanoresonators to local environment." Optics letters **35**, 956 (2010).

[42] O. Hess, J. B. Pendry, S. A. Maier, R. F. Oulton, J. M. Hamm, and K. L. Tsakmakidis, "Active nanoplasmonic metamaterials." Nature materials **11**, 573 (2012).

[43] O. Hess and K. L. Tsakmakidis, "Metamaterials with quantum gain." Science (New York, N.Y.) **339**, 654 (2013).

[44] R. F. Oulton, V. J. Sorger, D. A. Genov, D. F. P. Pile, and X. Zhang, "A hybrid plasmonic waveguide for subwavelength confinement and long-range propagation," Nature Photonics **2**, 496 (2008).

[45] P. D. Flammer, J. M. Banks, T. E. Furtak, C. G. Durfee, R. E. Hollingsworth, and R. T. Collins, "Hybrid plasmon/dielectric waveguide for integrated silicon-on-insulator optical elements." Optics Express **18**, 21013 (2010).

[46] M. C. Gather, K. Meerholz, N. Danz, and K. Leosson, "Net optical gain in a plasmonic waveguide embedded in a fluorescent polymer," Nature Photonics **4**, 457 (2010).

[47] L. Gao, L. Tang, F. Hu, R. Guo, X. Wang, and Z. Zhou, "Active metal strip hybrid plasmonic waveguide with low critical material gain." Optics Express **20**, 11487 (2012).

[48] Anon, "A bold unifying leap." Nature **471**, 265 (2011).

[49] S. A. Maier, *Plasmonics: Fundamentals and Applications* (Springer US, Boston, MA, 2007).

[50] H. Y. Li, S. M. Zhou, J. Li, Y. L. Chen, S. Y. Wang, Z. C. Shen, L. Y. Chen, H. Liu, and X. X. Zhang, "Analysis of the Drude Model in Metallic Films," Applied Optics **40**, 6307 (2001).

[51] P. B. Johnson and R. W. Christy, "Optical Constants of the Noble Metals," Physical Review B **6**, 4370 (1972).

[52] D. F. P. Pile and D. K. Gramotnev, "Channel plasmon-polariton in a triangular groove on a metal surface," Optics Letters **29**, 1069 (2004).

[53] S. Bozhevolnyi, V. Volkov, E. Devaux, and T. Ebbesen, "Channel Plasmon-Polariton Guiding by Subwavelength Metal Grooves," Physical Review Letters **95**, 046802 (2005).

[54] S. I. Bozhevolnyi, V. S. Volkov, E. Devaux, J.-Y. Laluet, and T. W. Ebbesen, "Channel plasmon subwavelength waveguide components including interferometers and ring resonators." Nature **440**, 508 (2006).

[55] N. Calander and M. Willander, "Theory of surface-plasmon resonance optical-field enhancement at prolate spheroids," Journal of Applied Physics **92**, 4878 (2002).

[56] P. Mühlschlegel, H.-J. Eisler, O. J. F. Martin, B. Hecht, and D. W. Pohl, "Resonant optical antennas." Science (New York, N.Y.) **308**, 1607 (2005).

[57] L. Novotny, "Effective Wavelength Scaling for Optical Antennas," Physical Review Letters **98**, 266802 (2007).

[58] K. B. Crozier, A. Sundaramurthy, G. S. Kino, and C. F. Quate, "Optical antennas: Resonators for local field enhancement," Journal of Applied Physics **94**, 4632 (2003).

[59] G. Vecchi, V. Giannini, and J. Gómez Rivas, "Shaping the Fluorescent Emission by Lattice Resonances in Plasmonic Crystals of Nanoantennas," Physical Review Letters **102**, 146807 (2009).

[60] E. Cubukcu and F. Capasso, "Optical nanorod antennas as dispersive one-dimensional Fabry-Perot resonators for surface plasmons," Applied Physics Letters **95**, 201101 (2009).

[61] E. J. Smythe, E. Cubukcu, and F. Capasso, "Optical properties of surface plasmon resonances of coupled metallic nanorods," Optics Express **15**, 7439 (2007).

[62] W. Rechberger, A. Hohenau, A. Leitner, J. Krenn, B. Lamprecht, and F. Aussenegg, "Optical properties of two interacting gold nanoparticles," Optics Communications **220**, 137 (2003).

[63] K. B. Crozier, E. Togan, E. Simsek, and T. Yang, "Experimental measurement of the dispersion relations of the surface plasmon modes of metal nanoparticle chains," Optics Express **15**, 17482 (2007).

[64] Y. Alaverdyan, E.-M. Hempe, A. N. Vamivakas, H. E, S. A. Maier, and M. Atatuure, "Spectral and angular distribution of Rayleigh scattering from plasmon-coupled nanohole chains," Applied Physics Letters **94**, 021112 (2009).

[65] J. A. Fan, C. Wu, K. Bao, J. Bao, R. Bardhan, N. J. Halas, V. N. Manoharan, P. Nordlander, G. Shvets, and F. Capasso, "Self-assembled plasmonic nanoparticle clusters." Science (New York, N.Y.) **328**, 1135 (2010).

[66] J. a. Fan, K. Bao, L. Sun, J. Bao, V. N. Manoharan, P. Nordlander, and F. Capasso, "Plasmonic mode engineering with templated self-assembled nanoclusters." Nano letters **12**, 5318 (2012).

[67] W. Zhou, Y. Hua, M. D. Huntington, and T. W. Odom, "Delocalized Lat-

tice Plasmon Resonances Show Dispersive Quality Factors," The Journal of Physical Chemistry Letters **3**, 1381 (2012).

[68] W. Zhou and T. W. Odom, "Tunable subradiant lattice plasmons by out-of-plane dipolar interactions." Nature nanotechnology **6**, 423 (2011).

[69] C. L. Haynes, A. D. McFarland, L. Zhao, R. P. Van Duyne, G. C. Schatz, L. Gunnarsson, J. Prikulis, B. Kasemo, and M. Käll, "Nanoparticle Optics: The Importance of Radiative Dipole Coupling in Two-Dimensional Nanoparticle Arrays," The Journal of Physical Chemistry B **107**, 7337 (2003).

[70] V. Kravets, F. Schedin, and A. Grigorenko, "Extremely Narrow Plasmon Resonances Based on Diffraction Coupling of Localized Plasmons in Arrays of Metallic Nanoparticles," Physical Review Letters **101**, 087403 (2008).

[71] V. Giannini, A. I. Fernández-Domínguez, Y. Sonnefraud, T. Roschuk, R. Fernández-García, and S. A. Maier, "Controlling light localization and light-matter interactions with nanoplasmonics." Small (Weinheim an der Bergstrasse, Germany) **6**, 2498 (2010).

[72] S. Linden, J. Kuhl, and H. Giessen, "Controlling the Interaction between Light and Gold Nanoparticles: Selective Suppression of Extinction," Physical Review Letters **86**, 4688 (2001).

[73] W. A. Murray and W. L. Barnes, "Plasmonic Materials," Advanced Materials **19**, 3771 (2007).

[74] I. Radko, V. Volkov, J. Beermann, A. Evlyukhin, T. Sø ndergaard, A. Boltasseva, and S. Bozhevolnyi, "Plasmonic metasurfaces for waveguiding and field enhancement," Laser & Photonics Review **3**, 575 (2009).

[75] J. A. Schuller, E. S. Barnard, W. Cai, Y. C. Jun, J. S. White, and M. L.

Brongersma, "Plasmonics for extreme light concentration and manipulation." Nature materials **9**, 193 (2010).

[76] N. Yu, E. Cubukcu, L. Diehl, D. Bour, S. Corzine, J. Zhu, G. Höfler, K. B. Crozier, and F. Capasso, "Bowtie plasmonic quantum cascade laser antenna," Optics Express **15**, 13272 (2007).

[77] J. Zuloaga, E. Prodan, and P. Nordlander, "Quantum description of the plasmon resonances of a nanoparticle dimer." Nano letters **9**, 887 (2009).

[78] M. Schnell, A. Garcia-Etxarri, J. Alkorta, J. Aizpurua, and R. Hillenbrand, "Phase-resolved mapping of the near-field vector and polarization state in nanoscale antenna gaps." Nano letters **10**, 3524 (2010).

[79] G. Subramania, S. Foteinopoulou, and I. Brener, "Nonresonant Broadband Funneling of Light via Ultrasubwavelength Channels," Physical Review Letters **107**, 163902 (2011).

[80] N. Yu, P. Genevet, M. A. M. Kats, F. Aieta, J.-P. Tetienne, F. Capasso, and Z. Gaburro, "Light propagation with phase discontinuities: generalized laws of reflection and refraction," Science **334**, 333 (2011).

[81] J. Lin, J. P. B. Mueller, Q. Wang, G. Yuan, N. Antoniou, X.-C. Yuan, and F. Capasso, "Polarization-controlled tunable directional coupling of surface plasmon polaritons." Science (New York, N.Y.) **340**, 331 (2013).

[82] X. Ni, N. K. Emani, A. V. Kildishev, A. Boltasseva, and V. M. Shalaev, "Broadband light bending with plasmonic nanoantennas." Science (New York, N.Y.) **335**, 427 (2012).

[83] S. Sun, K.-Y. Yang, C.-M. Wang, T.-K. Juan, W. T. Chen, C. Y. Liao, Q. He, S. Xiao, W.-T. Kung, G.-Y. Guo, L. Zhou, and D. P. Tsai, "High-efficiency broadband anomalous reflection by gradient meta-surfaces." Nano letters **12**, 6223 (2012).

[84] S. Zhang, D. A. Genov, Y. Wang, M. Liu, and X. Zhang, "Plasmon-Induced Transparency in Metamaterials," Physical Review Letters **101**, 47401 (2008).

[85] L. Zhang, T. Koschny, and C. M. Soukoulis, "Creating double negative index materials using the Babinet principle with one metasurface," Physical Review B **87**, 045101 (2013).

[86] R. F. Oulton, G. Bartal, D. F. P. Pile, and X. Zhang, "Confinement and propagation characteristics of subwavelength plasmonic modes," New Journal of Physics **10**, 105018 (2008).

[87] X. Sun, M. Z. Alam, J. S. Aitchison, and M. Mojahedi, in *IEEE Photonics Conference 2012*, Vol. 5 (IEEE, 2012) pp. 618–619.

[88] S. Wuestner, A. Pusch, K. L. Tsakmakidis, J. M. Hamm, and O. Hess, "Overcoming Losses with Gain in a Negative Refractive Index Metamaterial," Physical Review Letters **105**, 127401 (2010).

[89] D. Dai and S. He, "Low-loss hybrid plasmonic waveguide with double low-index nano-slots," Optics Express **18**, 17958 (2010).

[90] A. Karalis, E. Lidorikis, M. Ibanescu, J. Joannopoulos, and M. Soljačić, "Surface-Plasmon-Assisted Guiding of Broadband Slow and Subwavelength Light in Air," Physical Review Letters **95**, 063901 (2005).

[91] H. Ditlbacher, N. Galler, D. M. Koller, A. Hohenau, A. Leitner, F. R. Aussenegg, and J. R. Krenn, "Coupling dielectric waveguide modes to surface plasmon polaritons," Optics Express **16**, 10455 (2008).

[92] I. Avrutsky, R. Soref, and W. Buchwald, "Sub-wavelength plasmonic modes in a conductor-gap-dielectric system with a nanoscale gap." Optics express **18**, 348 (2010).

[93] T. Holmgaard and S. Bozhevolnyi, "Theoretical analysis of dielectric-loaded surface plasmon-polariton waveguides," Physical Review B **75**, 245405 (2007).

[94] S. H. Nam, A. J. Taylor, and A. Efimov, "Subwavelength hybrid terahertz waveguides." Optics express **17**, 22890 (2009).

[95] R. F. Oulton, V. J. Sorger, T. Zentgraf, R.-M. Ma, C. Gladden, L. Dai, G. Bartal, and X. Zhang, "Plasmon lasers at deep subwavelength scale." Nature **461**, 629 (2009).

[96] D. Dai and S. He, "A silicon-based hybrid plasmonic waveguide with a metal cap for a nano-scale light confinement." Optics express **17**, 16646 (2009).

[97] M. Z. Alam, J. Meier, J. S. Aitchison, and M. Mojahedi, "Propagation characteristics of hybrid modes supported by metal-low-high index waveguides and bends." Optics express **18**, 12971 (2010).

[98] X.-Y. Zhang, A. Hu, J. Z. Wen, T. Zhang, X.-J. Xue, Y. Zhou, and W. W. Duley, "Numerical analysis of deep sub-wavelength integrated plasmonic devices based on Semiconductor-Insulator-Metal strip waveguides." Optics express **18**, 18945 (2010).

[99] A. Karalis, J. Joannopoulos, and M. Soljačić, "Plasmonic-Dielectric Systems for High-Order Dispersionless Slow or Stopped Subwavelength Light," Physical Review Letters **103**, 043906 (2009).

[100] T. Zentgraf, S. Zhang, R. F. Oulton, and X. Zhang, "Ultranarrow coupling-induced transparency bands in hybrid plasmonic systems," Physical Review B **80**, 195415 (2009).

[101] M. Brun, A. Drezet, H. Mariette, N. Chevalier, J. C. Woehl, and S. Huant, "Remote optical addressing of single nano-objects," Europhysics Letters (EPL) **64**, 634 (2003).

[102] N. Anderson, A. Bouhelier, and L. Novotny, "Near-field photonics: tip-enhanced microscopy and spectroscopy on the nanoscale," Journal of Optics A: Pure and Applied Optics **8**, S227 (2006).

[103] F. Bernal Arango, A. Kwadrin, and A. F. Koenderink, "Plasmonic antennas hybridized with dielectric waveguides." ACS nano **6**, 10156 (2012).

[104] M. Février, P. Gogol, A. Aassime, R. Mégy, C. Delacour, A. Chelnokov, A. Apuzzo, S. Blaize, J.-M. Lourtioz, and B. Dagens, "Giant coupling effect between metal nanoparticle chain and optical waveguide." Nano letters **12**, 1032 (2012).

[105] D. Lee, H. Yim, S. Lee, and Others, "Tiny surface plasmon resonance sensor integrated on silicon waveguide based on vertical coupling into finite metal-insulator-metal plasmonic waveguide," Optics Express **19**, 19895 (2011).

[106] S. Tuccio, M. Centini, A. Benedetti, and C. Sibilia, "Subwavelength coherent control and coupling of light in plasmonic nanoresonators on dielectric waveguides," Journal of the Optical Society of America B **30**, 450 (2013).

[107] H. Booker, "Slot aerials and their relation to complementary wire aerials (Babinet's principle)," ... Engineers-Part IIIA: Radiolocation, Journal of the ... **93**, 620 (1946).

[108] T. Grosjean, M. Mivelle, F. I. Baida, G. W. Burr, and U. C. Fischer, "Diabolo nanoantenna for enhancing and confining the magnetic optical field." Nano letters **11**, 1009 (2011).

[109] F. Falcone, T. Lopetegi, M. Laso, J. Baena, J. Bonache, M. Beruete, R. Marqués, F. Martín, and M. Sorolla, "Babinet Principle Applied to the Design of Metasurfaces and Metamaterials," Physical Review Letters **93**, 197401 (2004).

[110] T. Zentgraf, T. Meyrath, A. Seidel, S. Kaiser, H. Giessen, C. Rockstuhl, and F. Lederer, "Babinet's principle for optical frequency metamaterials and nanoantennas," Physical Review B **76**, 033407 (2007).

[111] C. Maleville, B. Aspar, T. Poumeyrol, H. Moriceau, M. Bruel, A. Auberton-Hervè, and T. Barge, "Wafer bonding and H-implantation mechanisms involved in the Smart-cutÂ® technology," Materials Science and Engineering: B **46**, 14 (1997).

[112] M. L. Nesterov, A. V. Kats, and S. K. Turitsyn, "Extremely short-length surface plasmon resonance devices," Optics Express **16**, 20227 (2008).

[113] W.-P. Huang, "Coupled-mode theory for optical waveguides: an overview," Journal of the Optical Society of America A **11**, 963 (1994).

[114] S. Aksu, A. a. Yanik, R. Adato, A. Artar, M. Huang, and H. Altug, "High-throughput nanofabrication of infrared plasmonic nanoantenna arrays for vibrational nanospectroscopy." Nano letters **10**, 2511 (2010).

[115] S. Cataldo, J. Zhao, F. Neubrech, B. Frank, C. Zhang, P. V. Braun, and H. Giessen, "Hole-mask colloidal nanolithography for large-area low-cost metamaterials and antenna-assisted surface-enhanced infrared absorption substrates." ACS nano **6**, 979 (2012).

[116] A. Weber-Bargioni, A. Schwartzberg, M. Schmidt, B. Harteneck, D. F. Ogletree, P. J. Schuck, and S. Cabrini, "Functional plasmonic antenna scanning probes fabricated by induced-deposition mask lithography." Nanotechnology **21**, 065306 (2010).

[117] H. Duan, H. Hu, K. Kumar, Z. Shen, and J. K. W. Yang, "Direct and reliable patterning of plasmonic nanostructures with sub-10-nm gaps." ACS nano **5**, 7593 (2011).

[118] V. Malyarchuk, F. Hua, N. H. Mack, V. T. Velasquez, J. O. White, R. G.

Nuzzo, and J. A. Rogers, "High performance plasmonic crystal sensor formed by soft nanoimprint lithography," Optics Express **13**, 5669 (2005).

[119] A. Boltasseva, "Plasmonic components fabrication via nanoimprint," Journal of Optics A: Pure and Applied Optics **11**, 114001 (2009).

[120] M. H. Lee, M. D. Huntington, W. Zhou, J.-C. Yang, and T. W. Odom, "Programmable soft lithography: solvent-assisted nanoscale embossing." Nano letters **11**, 311 (2011).

[121] K. J. Stebe, E. Lewandowski, and M. Ghosh, "Materials science. Oriented assembly of metamaterials." Science (New York, N.Y.) **325**, 159 (2009).

[122] F. J. Ruess, L. Oberbeck, M. Y. Simmons, K. E. J. Goh, A. R. Hamilton, T. Hallam, S. R. Schofield, N. J. Curson, and R. G. Clark, "Toward Atomic-Scale Device Fabrication in Silicon Using Scanning Probe Microscopy," Nano Letters **4**, 1969 (2004).

[123] Q. Tan, A. Cosentino, M. Roussey, and H. P. Herzig, "Theoretical and experimental study of a 30 nm metallic slot array," Journal of the Optical Society of America B **28**, 1711 (2011).

[124] J. B. Pendry, L. Martín-Moreno, and F. J. García-Vidal, "Mimicking surface plasmons with structured surfaces." Science **305**, 847 (2004).

[125] J. Tian, S. Yu, W. Yan, and M. Qiu, "Broadband high-efficiency surface-plasmon-polariton coupler with silicon-metal interface," Applied Physics Letters **95**, 013504 (2009).

[126] Z. Han, A. Y. Elezzabi, and V. Van, "Experimental realization of sub-wavelength plasmonic slot waveguides on a silicon platform." Optics letters **35**, 502 (2010).

[127] R. Wood, "Anomalous Diffraction Gratings," Physical Review **48**, 928 (1935).

[128] A. Hessel and A. A. Oliner, "A New Theory of Wood's Anomalies on Optical Gratings," Applied Optics **4**, 1275 (1965).

[129] W. Barnes, T. Preist, S. Kitson, and J. Sambles, "Physical origin of photonic energy gaps in the propagation of surface plasmons on gratings," Physical Review B **54**, 6227 (1996).

[130] D. de Ceglia, M. A. Vincenti, M. Scalora, N. Akozbek, and M. J. Bloemer, "Plasmonic band edge effects on the transmission properties of metal gratings," AIP Advances **1**, 032151 (2011).

[131] Q. Gan, Z. Fu, Y. Ding, and F. Bartoli, "Ultrawide-Bandwidth Slow-Light System Based on THz Plasmonic Graded Metallic Grating Structures," Physical Review Letters **100**, 256803 (2008).

[132] J. Porto, F. García-Vidal, and J. Pendry, "Transmission Resonances on Metallic Gratings with Very Narrow Slits," Physical Review Letters **83**, 2845 (1999).

[133] J. Yang, Z. Zhou, H. Jia, X. Zhang, and S. Qin, "High-performance and compact binary blazed grating coupler based on an asymmetric subgrating structure and vertical coupling." Optics letters **36**, 2614 (2011).

[134] D. Taillaert, W. Bogaerts, P. Bienstman, T. Krauss, P. Van Daele, I. Moerman, S. Verstuyft, K. De Mesel, and R. Baets, "An out-of-plane grating coupler for efficient butt-coupling between compact planar waveguides and single-mode fibers," IEEE Journal of Quantum Electronics **38**, 949 (2002).

[135] L. Vivien, D. Pascal, and S. Lardenois, "Light injection in SOI microwaveguides using high-efficiency grating couplers," Journal of Lightwave Technology **24**, 3810 (2006).

[136] H.-Y. Chen and K.-C. Yang, "Design of a high-efficiency grating coupler based on a silicon nitride overlay for silicon-on-insulator waveguides." Applied optics **49**, 6455 (2010).

[137] S. Scheerlinck, J. Schrauwen, F. Van Laere, D. Taillaert, D. Van Thourhout, and R. Baets, "Efficient, broadband and compact metal grating couplers for silicon-on-insulator waveguides," Optics Express **15**, 9625 (2007).

[138] S. Scheerlinck, D. Taillaert, D. Van Thourhout, and R. Baets, "Flexible metal grating based optical fiber probe for photonic integrated circuits," Applied Physics Letters **92**, 031104 (2008).

[139] T. P. H. Sidiropoulos, S. A. Maier, and R. F. Oulton, "Efficient low dispersion compact plasmonic-photonic coupler." Optics express **20**, 12359 (2012).

[140] M. A. Vincenti, D. de Ceglia, M. Scalora, R. Marani, V. Marrocco, M. Grande, G. Morea, and A. D'Orazio, in *Library*, Vol. 7946, edited by A. Adibi, S.-Y. Lin, and A. Scherer (2011) pp. 794625–794625–7.

[141] B. Jafarian, N. Nozhat, and N. Granpayeh, "Analysis of a Triangular-shaped Plasmonic Metal-Insulator-Metal Bragg Grating Waveguide," Journal of the Optical Society of Korea **15**, 118 (2011).

[142] H. Gersen, T. Karle, R. Engelen, W. Bogaerts, J. Korterik, N. van Hulst, T. Krauss, and L. Kuipers, "Real-Space Observation of Ultraslow Light in Photonic Crystal Waveguides," Physical Review Letters **94**, 073903 (2005).

[143] V. Mikhailov, G. Wurtz, J. Elliott, P. Bayvel, and A. Zayats, "Dispersing Light with Surface Plasmon Polaritonic Crystals," Physical Review Letters **99**, 083901 (2007).

[144] M. Soljacić and J. D. Joannopoulos, "Enhancement of nonlinear effects using photonic crystals." Nature materials **3**, 211 (2004).

[145] J. J. Baumberg, T. A. Kelf, Y. Sugawara, S. Cintra, M. E. Abdelsalam, P. N. Bartlett, and A. E. Russell, "Angle-resolved surface-enhanced Ra-

man scattering on metallic nanostructured plasmonic crystals." Nano letters **5**, 2262 (2005).

[146] M. Kretschmann and A. Maradudin, "Band structures of two-dimensional surface-plasmon polaritonic crystals," Physical Review B **66**, 245408 (2002).

[147] J. D. Caldwell, O. J. Glembocki, F. J. Bezares, M. I. Kariniemi, J. T. Niinistö, T. T. Hatanpää, R. W. Rendell, M. Ukaegbu, M. K. Ritala, S. M. Prokes, C. M. Hosten, M. a. Leskelä, and R. Kasica, "Large-area plasmonic hot-spot arrays: sub-2 nm interparticle separations with plasma-enhanced atomic layer deposition of Ag on periodic arrays of Si nanopillars." Optics express **19**, 26056 (2011).

[148] P. Ghenuche, S. Cherukulappurath, T. H. Taminiau, N. F. van Hulst, and R. Quidant, "Spectroscopic Mode Mapping of Resonant Plasmon Nanoantennas," Physical Review Letters **101**, 116805 (2008).

[149] H. Fischer and O. J. F. Martin, "Engineering the optical response of plasmonic nanoantennas," Optics Express **16**, 9144 (2008).

[150] E. Hao and G. C. Schatz, "Electromagnetic fields around silver nanoparticles and dimers." The Journal of chemical physics **120**, 357 (2004).

[151] H. Choi, D. F. Pile, S. Nam, G. Bartal, and X. Zhang, "Compressing surface plasmons for nano-scale optical focusing," Optics Express **17**, 7519 (2009).

[152] L. J. Sherry, R. Jin, C. A. Mirkin, G. C. Schatz, and R. P. Van Duyne, "Localized surface plasmon resonance spectroscopy of single silver triangular nanoprisms." Nano letters **6**, 2060 (2006).

[153] A. L. Koh, A. I. Fernández-Domínguez, D. W. McComb, S. A. Maier, and J. K. W. Yang, "High-resolution mapping of electron-beam-excited plas-

mon modes in lithographically defined gold nanostructures." Nano letters **11**, 1323 (2011).

[154] Y. El Hassouani, C. Li, Y. Pennec, E. H. El Boudouti, H. Larabi, A. Akjouj, O. Bou Matar, V. Laude, N. Papanikolaou, A. Martinez, and B. Djafari Rouhani, "Dual phononic and photonic band gaps in a periodic array of pillars deposited on a thin plate," Physical Review B **82**, 155405 (2010).

[155] R. Marani, M. Grande, V. Marrocco, A. D'Orazio, V. Petruzzelli, M. A. Vincenti, and D. de Ceglia, "Plasmonic bandgap formation in two-dimensional periodic arrangements of gold patches with subwavelength gaps." Optics letters **36**, 903 (2011).

[156] M. Liu, Y. Song, Y. Zhang, X. Wang, and C. Jin, "Mode Evolution and Transmission Suppression in a Perforated Ultrathin Metallic Film with a Triangular Array of Holes," Plasmonics **7**, 397 (2012).

[157] A. Christ, S. Tikhodeev, N. Gippius, J. Kuhl, and H. Giessen, "Waveguide-Plasmon Polaritons: Strong Coupling of Photonic and Electronic Resonances in a Metallic Photonic Crystal Slab," Physical Review Letters **91**, 183901 (2003).

[158] A. Christ, T. Zentgraf, J. Kuhl, S. Tikhodeev, N. Gippius, and H. Giessen, "Optical properties of planar metallic photonic crystal structures: Experiment and theory," Physical Review B **70**, 125113 (2004).

[159] N. A. Gippius, "Waveguide Plasmon Polaritons in Metal-Dielectric Photonic Crystal Slabs," Physics of the Solid State **47**, 145 (2005).

[160] C. Tan, J. Simonen, and T. Niemi, "Hybrid waveguide-surface plasmon polariton modes in a guided-mode resonance grating," Optics Communications **285**, 4381 (2012).

[161] W. Zhou, J. Y. Suh, Y. Hua, and T. W. Odom, "Hybridization of Local-

ized and Guided Modes in 2D Metal-Insulator-Metal Nanocavity Arrays," The Journal of Physical Chemistry C **117**, 2541 (2013).

[162] V. Giannini, G. Vecchi, and J. Gómez Rivas, "Lighting Up Multipolar Surface Plasmon Polaritons by Collective Resonances in Arrays of Nanoantennas," Physical Review Letters **105**, 266801 (2010).

[163] S. Maier, P. Kik, and H. Atwater, "Optical pulse propagation in metal nanoparticle chain waveguides," Physical Review B **67**, 1 (2003).

[164] M. Grande, M. A. Vincenti, T. Stomeo, G. Morea, R. Marani, V. Marrocco, V. Petruzzelli, A. D'Orazio, R. Cingolani, M. De Vittorio, D. de Ceglia, and M. Scalora, "Experimental demonstration of a novel bio-sensing platform via plasmonic band gap formation in gold nano-patch arrays." Optics express **19**, 21385 (2011).

[165] J. DiMaria, E. Dimakis, T. D. Moustakas, and R. Paiella, "Plasmonic off-axis unidirectional beaming of quantum-well luminescence," Applied Physics Letters **103**, 251108 (2013).

[166] J. Winn, S. Fan, J. Joannopoulos, and E. Ippen, "Interband transitions in photonic crystals," Physical Review B **59**, 1551 (1999).

[167] Z. Yu and S. Fan, "Optical isolation based on nonreciprocal phase shift induced by interband photonic transitions," Applied Physics Letters **94**, 171116 (2009).

[168] Z. Yu and S. Fan, "Complete optical isolation created by indirect interband photonic transitions," Nature Photonics **3**, 91 (2009).

[169] G. Leuchs and M. Sondermann, "Time-reversal symmetry in optics*," Physica Scripta **85**, 058101 (2012).

[170] R. L. Espinola, T. Izuhara, M.-C. Tsai, R. M. Osgood, Jr., and H. Dï¿œtsch, "Magneto-optical nonreciprocal phase shift in garnet/silicon-on-insulator waveguides," Optics Letters **29**, 941 (2004).

[171] S. Ghosh, S. Keyvaninia, Y. Shoji, W. Van Roy, T. Mizumoto, G. Roelkens, and R. G. Baets, "Compact Mach-Zehnder Interferometer Ce:YIG/SOI Optical Isolators," IEEE Photonics Technology Letters **24**, 1653 (2012).

[172] Z. Yu, S. Fan, and S. Member, "Integrated Nonmagnetic Optical Isolators Based on Photonic Transitions," IEEE Journal of Selected Topics in Quantum Electronics **16**, 459 (2010).

[173] H. Lira, Z. Yu, S. Fan, and M. Lipson, "Electrically Driven Nonreciprocity Induced by Interband Photonic Transition on a Silicon Chip," Physical Review Letters **109**, 033901 (2012).

[174] M. Soljačić, C. Luo, J. D. Joannopoulos, and S. Fan, "Nonlinear photonic crystal microdevices for optical integration," Optics Letters **28**, 637 (2003).

[175] Z. Wang, Y. Chong, J. D. Joannopoulos, and M. Soljacić, "Observation of unidirectional backscattering-immune topological electromagnetic states." Nature **461**, 772 (2009).

[176] C. Wang, X.-L. Zhong, and Z.-Y. Li, "Linear and passive silicon optical isolator." Scientific reports **2**, 674 (2012).

[177] V. Liu, D. a. B. Miller, and S. Fan, "Ultra-compact photonic crystal waveguide spatial mode converter and its connection to the optical diode effect." Optics express **20**, 28388 (2012).

[178] M. Greenberg and M. Orenstein, "Irreversible coupling by use of dissipative optics," Optics Letters **29**, 451 (2004).

[179] L. Feng, M. Ayache, J. Huang, Y.-L. Xu, M.-H. Lu, Y.-F. Chen, Y. Fainman, and A. Scherer, "Nonreciprocal light propagation in a silicon photonic circuit." Science (New York, N.Y.) **333**, 729 (2011).

[180] Y.-L. Xu, L. Feng, M.-H. Lu, and Y.-F. Chen, "Asymmetric optical mode conversion and transmission by breaking PT-symmetry on silicon photonic circuits," Physics Letters A **376**, 886 (2012).

[181] L. Fan, J. Wang, L. T. Varghese, H. Shen, B. Niu, Y. Xuan, A. M. Weiner, and M. Qi, "An all-silicon passive optical diode." Science (New York, N.Y.) **335**, 447 (2012).

[182] S. Fan, R. Baets, A. Petrov, Z. Yu, J. D. Joannopoulos, W. Freude, A. Melloni, M. Popović, M. Vanwolleghem, D. Jalas, M. Eich, M. Krause, H. Renner, E. Brinkmeyer, and C. R. Doerr, "Comment on "Nonreciprocal light propagation in a silicon photonic circuit"." Science (New York, N.Y.) **335**, 38; author reply 38 (2012).

[183] D. Jalas, A. Petrov, M. Eich, W. Freude, S. Fan, Z. Yu, R. Baets, M. Popović, A. Melloni, J. D. Joannopoulos, M. Vanwolleghem, C. R. Doerr, and H. Renner, "What is - and what is not - an optical isolator," Nature Photonics **7**, 579 (2013).

[184] D. a. B. Miller, "All linear optical devices are mode converters." Optics Express **20**, 23985 (2012).

[185] C. G. Treviño Palacios, G. I. Stegeman, and P. Baldi, "Spatial nonreciprocity in waveguide second-order processes," Optics Letters **21**, 1442 (1996).

[186] K. Gallo, G. Assanto, K. R. Parameswaran, and M. M. Fejer, "All-optical diode in a periodically poled lithium niobate waveguide," Applied Physics Letters **79**, 314 (2001).

[187] Q. Lin, J. Zhang, G. Piredda, R. W. Boyd, P. M. Fauchet, and G. P. Agrawal, "Dispersion of silicon nonlinearities in the near infrared region," Applied Physics Letters **91**, 021111 (2007).

[188] S. Kim, J. Jin, Y.-J. Kim, I.-y. Park, Y. Kim, and S.-W. Kim, "High-harmonic generation by resonant plasmon field enhancement." Nature **453**, 757 (2008).

[189] V. G. Kravets, F. Schedin, R. Jalil, L. Britnell, R. V. Gorbachev, D. Ansell, B. Thackray, K. S. Novoselov, A. K. Geim, A. V. Kabashin, and A. N. Grigorenko, "Singular phase nano-optics in plasmonic metamaterials for label-free single-molecule detection." Nature materials **12**, 304 (2013).

[190] T. W. Ebbesen, C. Genet, and S. I. Bozhevolnyi, "Surface-plasmon circuitry," Physics Today **61**, 44 (2008).

[191] B. C. Galarreta, E. Harté, N. Marquestaut, P. R. Norton, and F. Lagugné-Labarthet, "Plasmonic properties of Fischer's patterns: polarization effects." Physical chemistry chemical physics : PCCP **12**, 6810 (2010).

[192] T. Geldhauser, S. Ikegaya, A. Kolloch, N. Murazawa, K. Ueno, J. Boneberg, P. Leiderer, E. Scheer, and H. Misawa, "Visualization of Near-Field Enhancements of Gold Triangles by Nonlinear Photopolymerization," Plasmonics **6**, 207 (2011).

[193] C. Ouyang, Z. Xiong, F. Zhao, B. Dong, X. Hu, X. Liu, and J. Zi, "Slow light with low group-velocity dispersion at the edge of photonic graphene," Physical Review A **84**, 015801 (2011).

[194] D. K. Polyushkin, E. Hendry, E. K. Stone, and W. L. Barnes, "THz generation from plasmonic nanoparticle arrays." Nano letters **11**, 4718 (2011).

[195] D. Han, Y. Lai, J. Zi, Z.-Q. Zhang, and C. Chan, "Dirac Spectra and Edge States in Honeycomb Plasmonic Lattices," Physical Review Letters **102**, 123904 (2009).

[196] T. Ochiai and M. Onoda, "Photonic analog of graphene model and its

extension: Dirac cone, symmetry, and edge states," Physical Review B **80**, 1 (2009).

[197] C. E. Kriegler, M. S. Rill, S. Linden, and M. Wegener, "Bianisotropic Photonic Metamaterials," IEEE Journal of Selected Topics in Quantum Electronics **16**, 367 (2010).

[198] E. Ozbay, "Plasmonics: merging photonics and electronics at nanoscale dimensions." Science (New York, N.Y.) **311**, 189 (2006).

[199] V. Giannini, A. I. Fernández-Domínguez, S. C. Heck, and S. a. Maier, "Plasmonic nanoantennas: fundamentals and their use in controlling the radiative properties of nanoemitters." Chemical reviews **111**, 3888 (2011).

Appendix A

Methods

A.1 Scattering Calculations

The majority of the numerical studies of this work use a scattering calculation as outlined by [199]. The total fields at a boundary are a superposition of the incident and scattered fields, or $\mathbf{E}_{\text{tot}} = \mathbf{E}_{\text{inc}} + \mathbf{E}_{\text{scat}}$ and $\mathbf{H}_{\text{tot}} = \mathbf{H}_{\text{inc}} + \mathbf{H}_{\text{scat}}$. The FEM software solves the total field solution from the incident field, and therefore the scattered field can be obtained from these equations. The incident field is the illuminating energy (e.g. from an external source) while the scattered energy is the light scattered off the scatterer after interacting with the incident light. The power flow across the boundary can therefore be given by the Poynting vectors

$$\mathbf{S}_{\text{tot}} = \mathbf{S}_{\text{inc}} + \mathbf{S}_{\text{scat}} + \mathbf{S}_{\text{ext}} = \frac{1}{2}\text{Re}[\mathbf{E}_{\text{tot}} \times \mathbf{H}^*_{\text{tot}}]$$

$$\mathbf{S}_{\text{inc}} = \frac{1}{2}\text{Re}[\mathbf{E}_{\text{inc}} \times \mathbf{H}^*_{\text{inc}}]$$

$$\mathbf{S}_{\text{scat}} = \frac{1}{2}\text{Re}[\mathbf{E}_{\text{scat}} \times \mathbf{H}^*_{\text{scat}}]$$

$$\mathbf{S}_{\text{ext}} = \frac{1}{2}\text{Re}[\mathbf{E}_{\text{scat}} \times \mathbf{H}^*_{\text{inc}}] + \frac{1}{2}\text{Re}[\mathbf{E}_{\text{inc}} \times \mathbf{H}^*_{\text{scat}}],$$

where $\mathbf{S}_{\text{ext}}$ is the extinction power flow which arises from the interference of the scattered field and incident field.

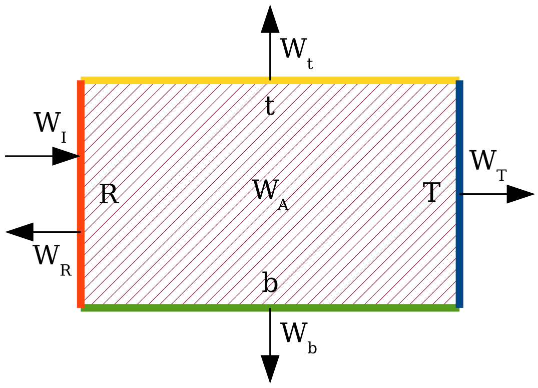

Figure A.1: The boundaries T, R, t and b, and absorption A within the system (hashed area), with the injected energy W_I upon boundary R.

By integrating the power flow through a given surface (i.e. the T, R, t or b surfaces, see figure A.1), the energy flux (W) through that surface can be obtained. The total power flow ($\mathbf{S}_{tot}$) across the surface is integrated to gain the total energy flux across the boundary except in the case of the reflected energy, as this surface includes the incident light which needs to be omitted to obtain only the reflected (scattered) proportion of the light. The total energy absorbed in the system (W_A) is given by the integral of the total flux in and out of the system for all the given boundaries (i.e. a closed surface). The absorbed energy within the system is given by the negative integral of the total energy through all the boundaries. Assuming loss within the system, the integral result will be negative due to the inward orientation of the net energy flux. The total incident energy to the system (W_I) must therefore be a sum of the energy fluxes across the boundaries and the absorbed energy within the system. Dividing the energy fluxes of each boundary by the total incident energy provides the normalised data as plotted in the results of this work.

$$\mathrm{T} = \frac{\mathrm{W_T}}{\mathrm{W_I}} = \frac{\int^{\mathrm{T}} \mathbf{S}_{\mathrm{tot}} \mathrm{ds}}{\mathrm{W_I}}$$

$$\mathrm{R} = \frac{\mathrm{W_R}}{\mathrm{W_I}} = \frac{\int^{\mathrm{R}} \mathbf{S}_{\mathrm{scat}} \mathrm{ds}}{\mathrm{W_I}}$$

$$t = \frac{W_t}{W_I} = \frac{\int^t \mathbf{S}_{tot} d\mathbf{s}}{W_I}$$

$$b = \frac{W_b}{W_I} = \frac{\int^b \mathbf{S}_{tot} d\mathbf{s}}{W_I}$$

$$A = \frac{W_A}{W_I} = \frac{-\oint \mathbf{S}_{tot} d\mathbf{s}}{W_I}$$

$$W_I = W_T + W_R + W_t + W_b + W_A$$

A.2 Two-Step Scattering Process

In order to calculate the scattered field from the isolated trimer molecule in chapter 4.1, whilst keeping the in-plane excitation from the waveguide, a sophisticated computational procedure is required. To isolate the timer scatterer, all the domain boundaries are required to be PML boundaries which extend the domain as an infinite isotropic and inhomogeneous medium. This allows for the scattered fields to be obtained at the boundaries as no fields are reflected back into the computational domain. However, the underlying waveguide mode cannot be solved with PML boundaries on the side. The fundamental TE mode would effectively be confined by the PML boundaries on the sides, resulting in a two dimensional mode instead of the required one dimensional waveguide mode..

Using COMSOL Multiphysics (www.comsol.com), two successive simulations are performed to solve the problem outlined above (figure A.2). The first simulation is much the same as the majority of simulations performed in this work. The waveguide and scatterer are meshed with PML boundaries on the y and z boundaries, and PEC boundaries on the x (side) boundaries. This allows for the one dimensional waveguide mode to be simulated correctly. However, for this simulation, the permittivity of the trimer molecule is set to the permittivity of air (i.e. the same as the surrounding superstrate). This effectively removes the scatterer (the metallic molecule) from the system, but keeps the meshing of the molecule shape to prevent interpolation errors arising from a change in the mesh. With the scattering medium effectively removed, the unaltered TE waveguide mode is solved throughout the structure.

The second process restores the scatterer permittivity to that of the metal. It replaces the PEC boundaries on the sides with PML boundaries, allowing the calculation of the scattered energy flux. The previously solved fields for the TE waveguide mode across the whole structure is used as the initialising background field for this simulation, allowing for the calculation the total and scattered fields with the scatterer now present.

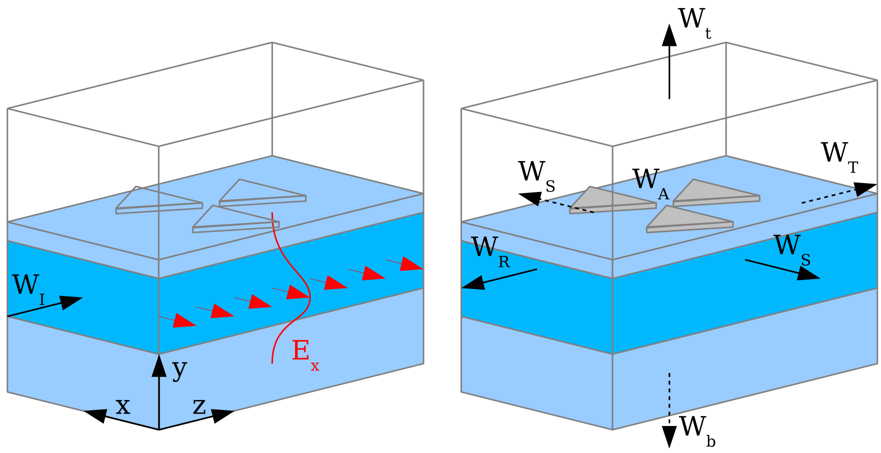

Figure A.2: The two-step simulation process. The first simulation injects the fundamental TE waveguide mode in a PEC-sided geometry, with the scatterer effectively removed. The second simulation (right) restores the scatterer and uses the solved waveguide field from the first simulation as the background field for the scattering calculations in a PML-sided geometry.